Appendix Table of Contents

Appendix.....A-1

A.1. Supplementary data for Chapter Two A-1

A.1.1. Definition of geometric parameters.....A-1

A.1.2. NMR and IR spectra of synthesised compounds A-2

A.1.3. Computer Gibbs energy for 1, 2, 11, and 12 .....A-42

A.2. Summary of unsuccessful chemistries A-43

A.2.1. NMR spectra A-46

A.2.2. Crystallographic parameters.....A-53

A.3. Supplementary data for Chapter Four A-59

A.3.1. NMR and IR spectra of synthesised compounds A-59

A.3.2. Additional crystallographic information A-65

A.3.3. Polymerisation Characterisation for Chapter 4 .....A-67

A.3.4. Copolymerisation ϵ-CL and L-La using 7 and $OPPH_3$.....A-86

A.4. Additional files.....A-88

A.4.1. Crystallographic information file A-88

Appendix

A.1. Supplementary data for Chapter Two

A.1.1. Definition of geometric parameters

Throughout this thesis, I^*_{cent} refers to the centroid of the C_5 fragment of the permethylindenyl ring. The ring slip parameter, Δ_{M-C}, corresponds to the difference between the metal–I^*_{cent} distance and that of the projection of the metal onto the least squares plane defined by I^*_{C5}, such that , and is a measure of how far the complex is distorted towards η^3 coordination compared to η^5. The torsion angle, TA′, is a measure of the twist between the apical I* and basal aryloxy motifs. It is based upon the parameter first used by Calhorda *et al.*,[10] which for homoleptic metallocenes was defined as C(2)–Cp_{cent}–Cp_{cent}′–Cp(2′). It was adapted for PHENI* complexes, and defined as TA = C(10)–C(2)–O(1)–C(18).[11] For this work, a further refined TA (M) = C(10)–C(2)–M(1)–A(1) is defined as the dihedral angle between the least squares plane defined by I^*_{C5} and that defined by the metal and the bridging heteroatom (A) tethered to the I*ring by a bridge of 'n' length. (**Figure A.1**)

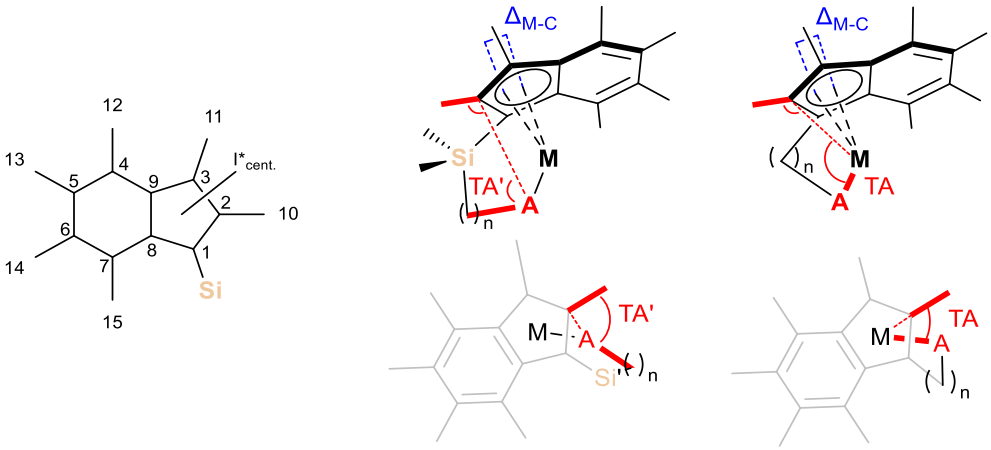


Figure A.1 Permethylindenyl numbering scheme, and definitions of the ring slip parameter, Δ_{M-I^*Cent} (blue) the characteristic torsion angle, TA′ (middle) and TA (right).

A.1.2. NMR and IR spectra of synthesised compounds

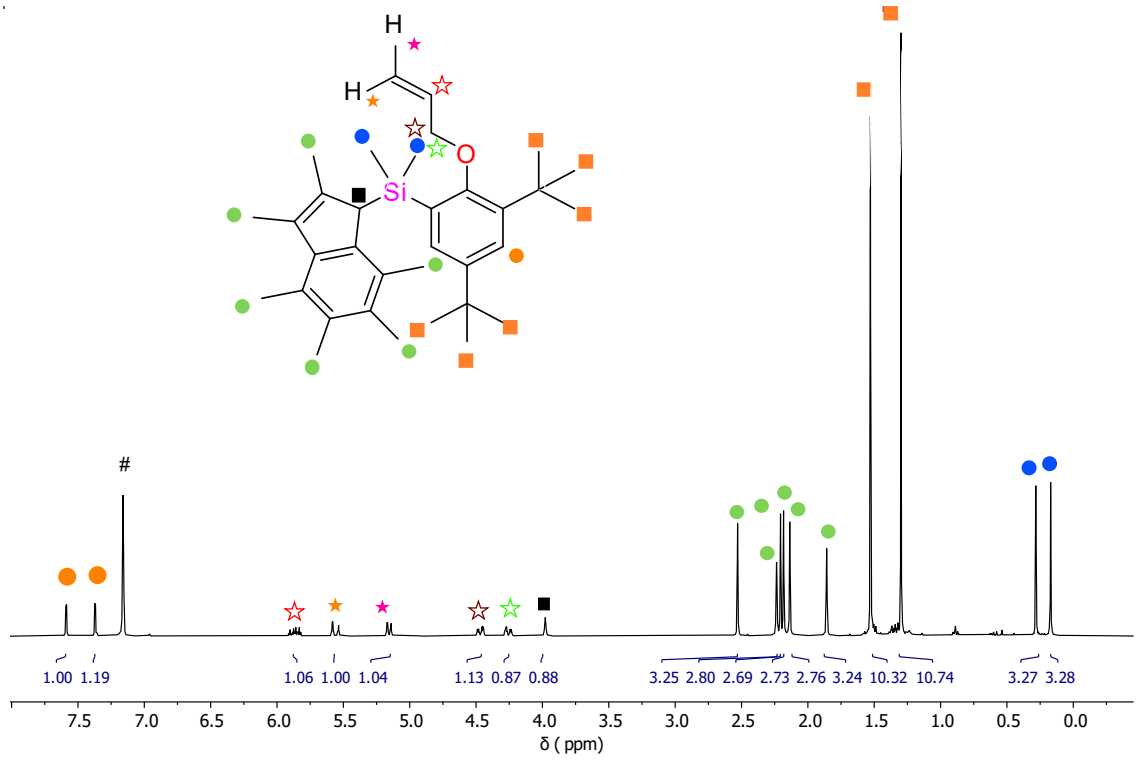


Figure A.2 ^{1}H NMR spectrum (benzene-d_6, 600 MHz, 298 K) of ^{Me_2}SB($^{t Bu_2}$ArOAllyl,I*)H (#) denotes residual protio solvent

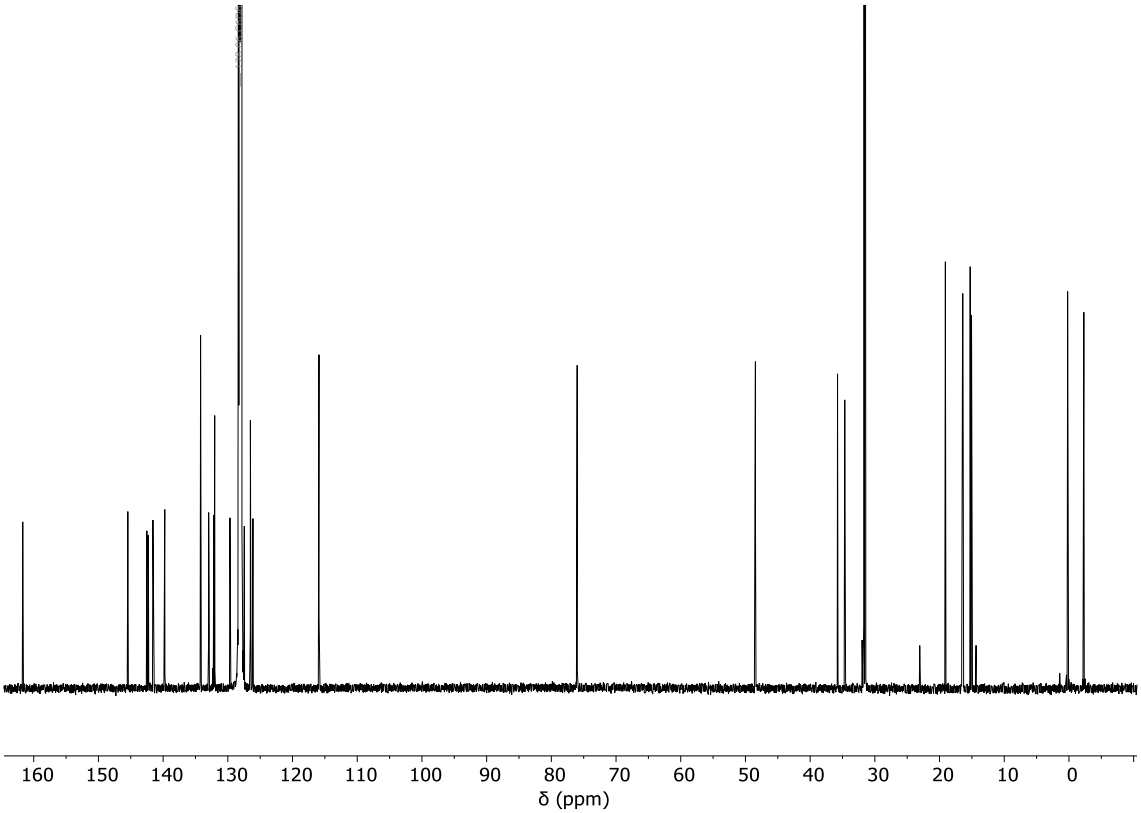


Figure A.3 ^{13}C{^{1}H} NMR spectrum (benzene-d_6, 151 MHz, 298 K) of ^{Me_2}SB($^{t Bu_2}$ArOAllyl,I*)H .

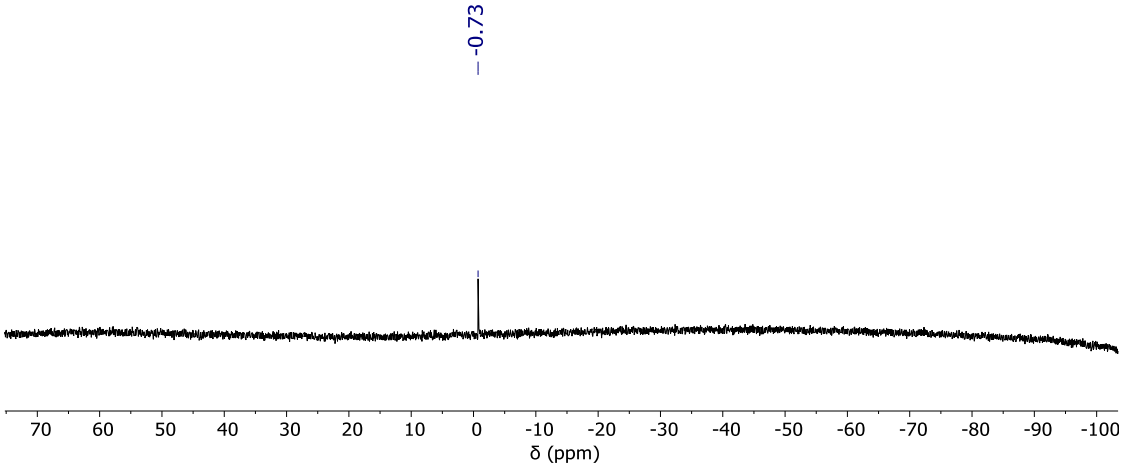


Figure A.4 ^{29}Si{^{1}H} NMR spectrum (benzene-d_6, 119 MHz, 298 K) of ^{Me_2}SB(^{tBu_2}ArOAllyl,I*)H .

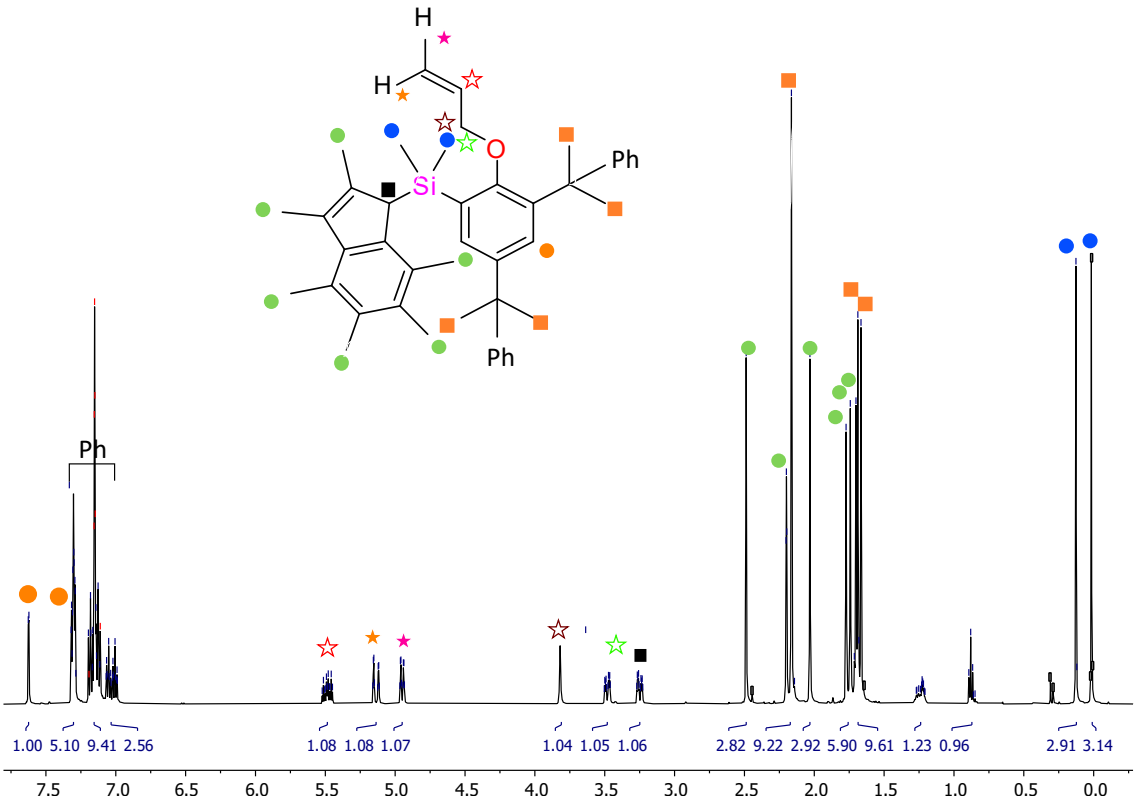


Figure A.5 ^{1}H NMR spectrum (benzene-d_6, 500 MHz, 298 K).of ^{Me_2}SB(^{Cumyl_2}ArOAllyl,I*)H

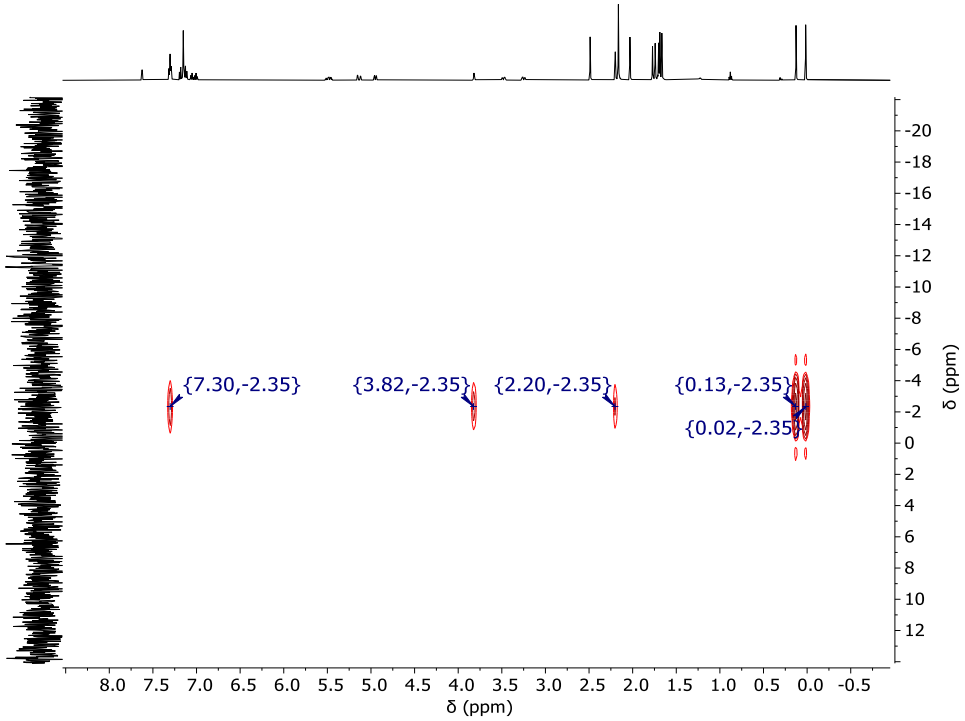


Figure A.6 $^{29}Si\{^{1}H\}$ HMBC 2D NMR spectrum (benzene-d_6, 500 MHz, 298 K) of $^{Me_2}SB(^{Cumyl_2}ArOAllyl,I^*)H$: δ -2.35 ppm

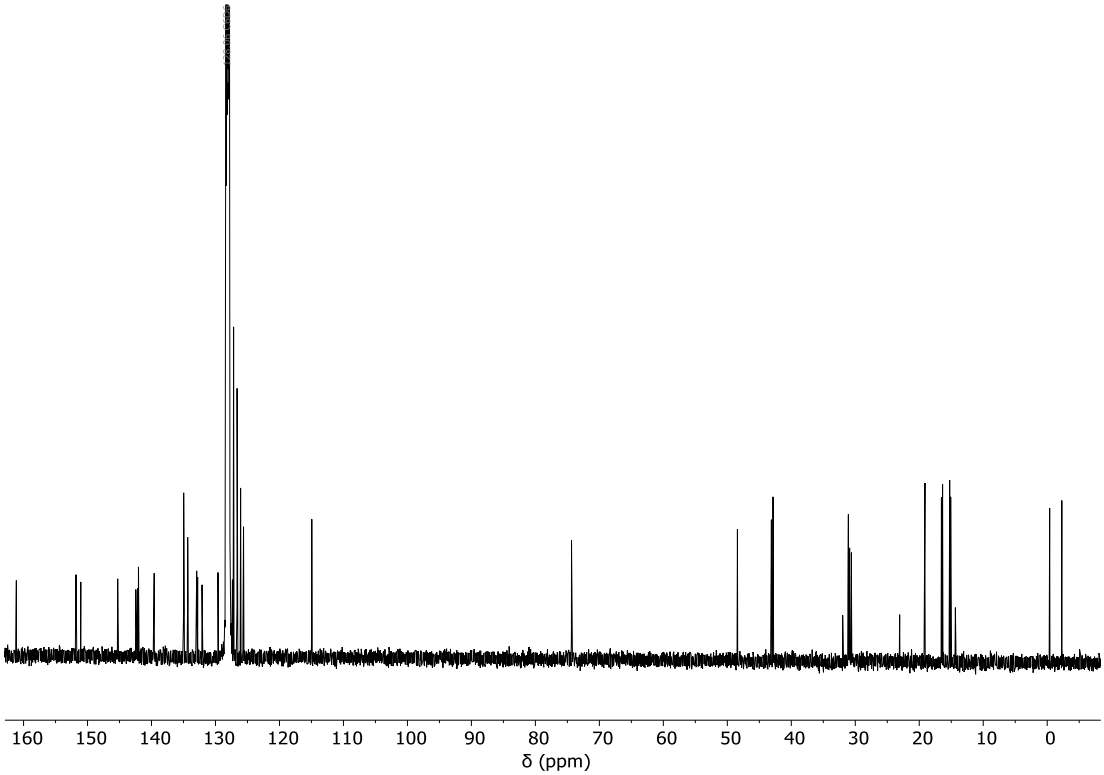


Figure A.7 $^{13}C\{^{1}H\}$ NMR spectrum (benzene-d_6, 126 MHz, 298 K) of $^{Me_2}SB(^{Cumyl_2}ArOAllyl,I^*)H$.

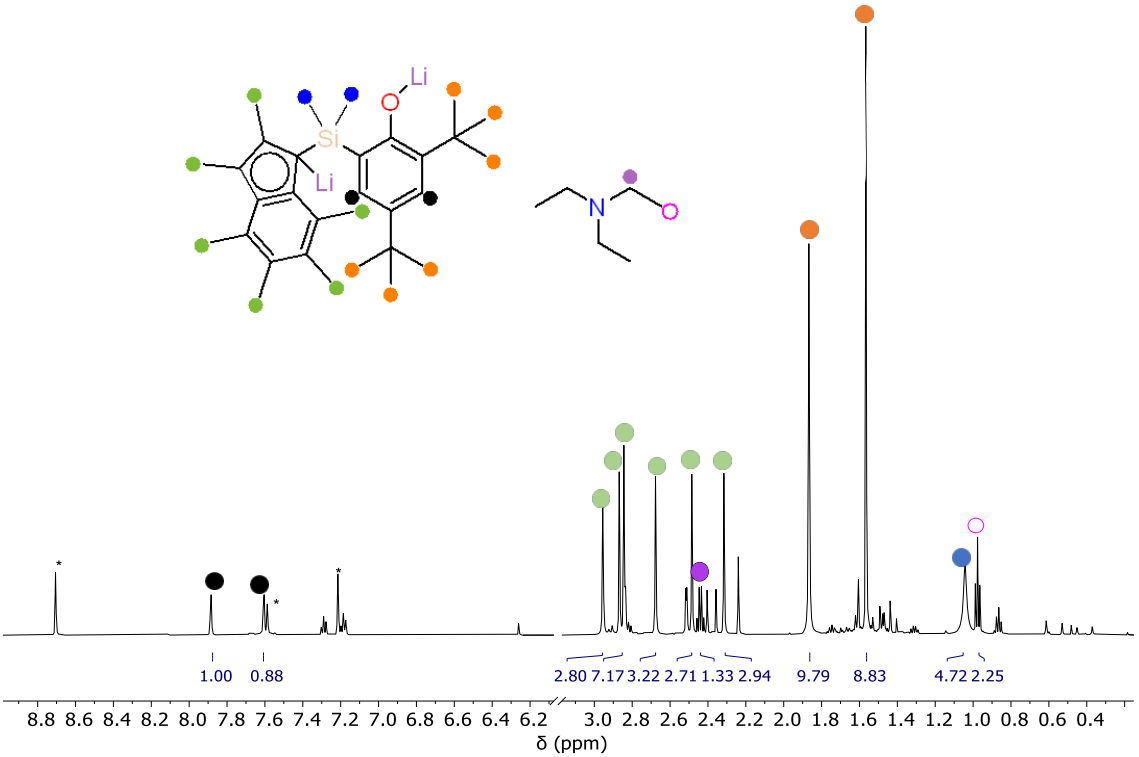


Figure A.8 ^{1}H NMR spectrum (pyridine-d_5, 600 MHz, 298 K) of ^{Me_2}SB($^{t\text{Bu}_2}$ArOAllyl,I*)Li$_2$.(NEt$_3$)$_{0.3}$

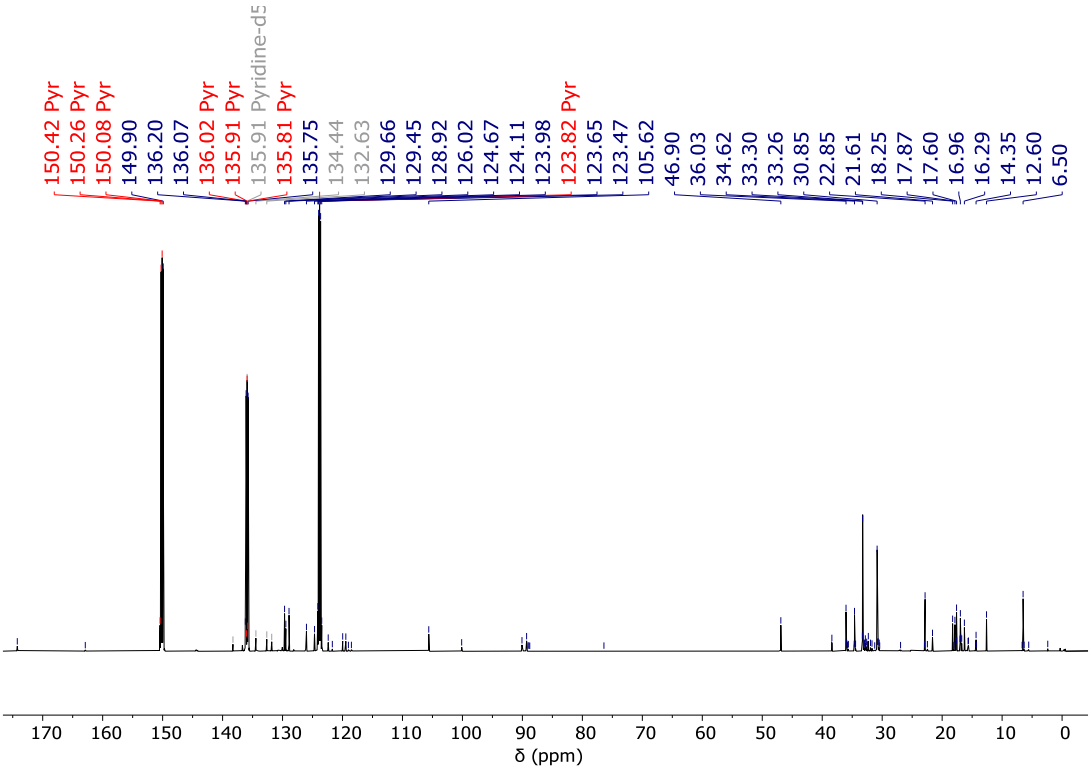


Figure A.9 ^{13}C{^{1}H} NMR spectrum (pyridine-d_5, 151 MHz, 298 K) of ^{Me_2}SB($^{t\text{Bu}_2}$ArOAllyl,I*)Li$_2$.(NEt$_3$)$_{0.3}$

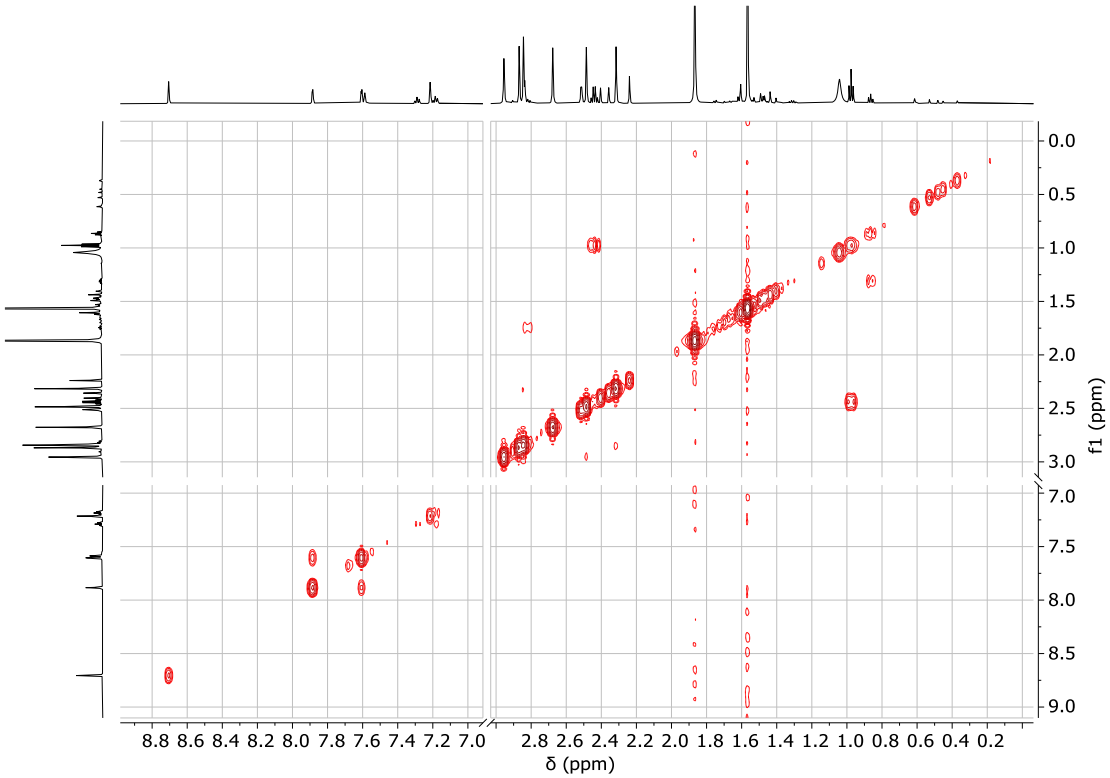


Figure A.10 ^{1}H-^{1}H COSY NMR spectrum (pyridine-d_5, 600 MHz, 298 K) of $^{Me_2}SB(^{t\text{Bu}_2}ArOAllyl,I^*)Li_2.(NEt_3)_{0.3}$

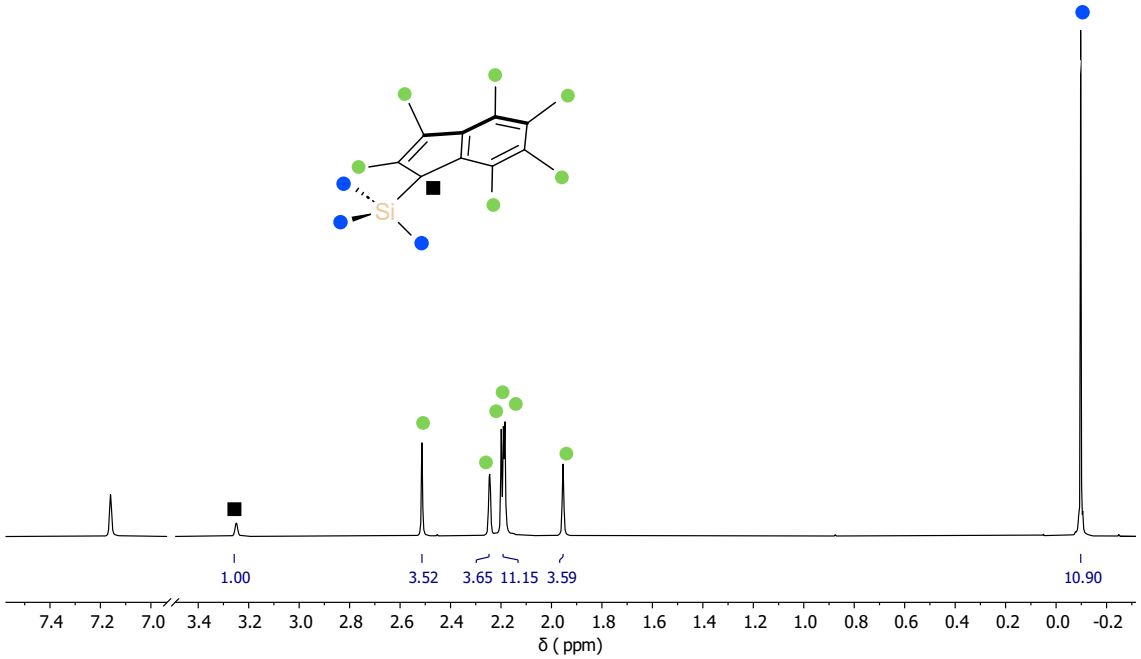


Figure A.11 ^{1}H NMR spectrum (benzene-d_6, 400 MHz, 298 K) of I*SiMe$_3$H.

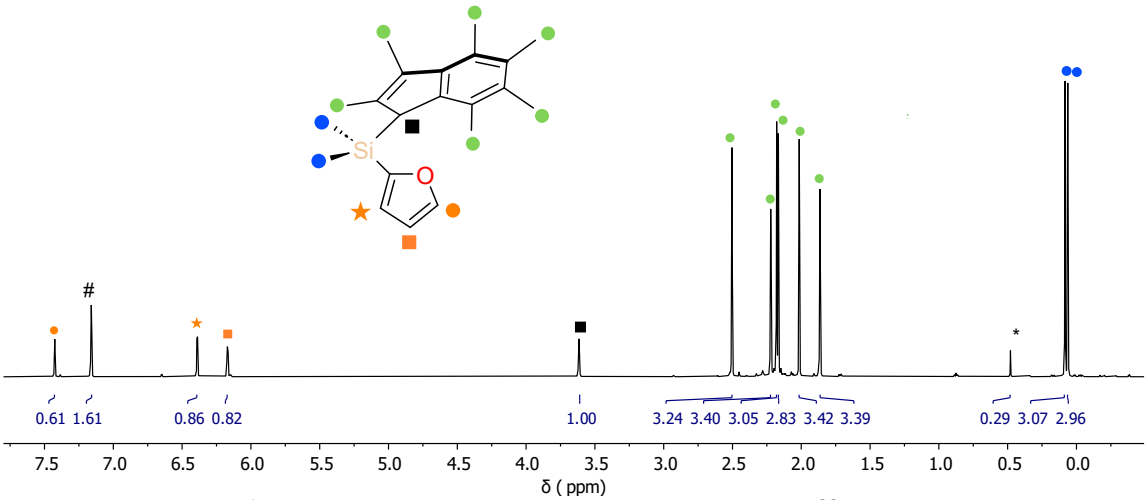


Figure A.12 ^{1}H NMR spectrum (benzene-d_6, 400 MHz, 298 K) of ^{Me_2}SB(I*,OC_4H_3)H.

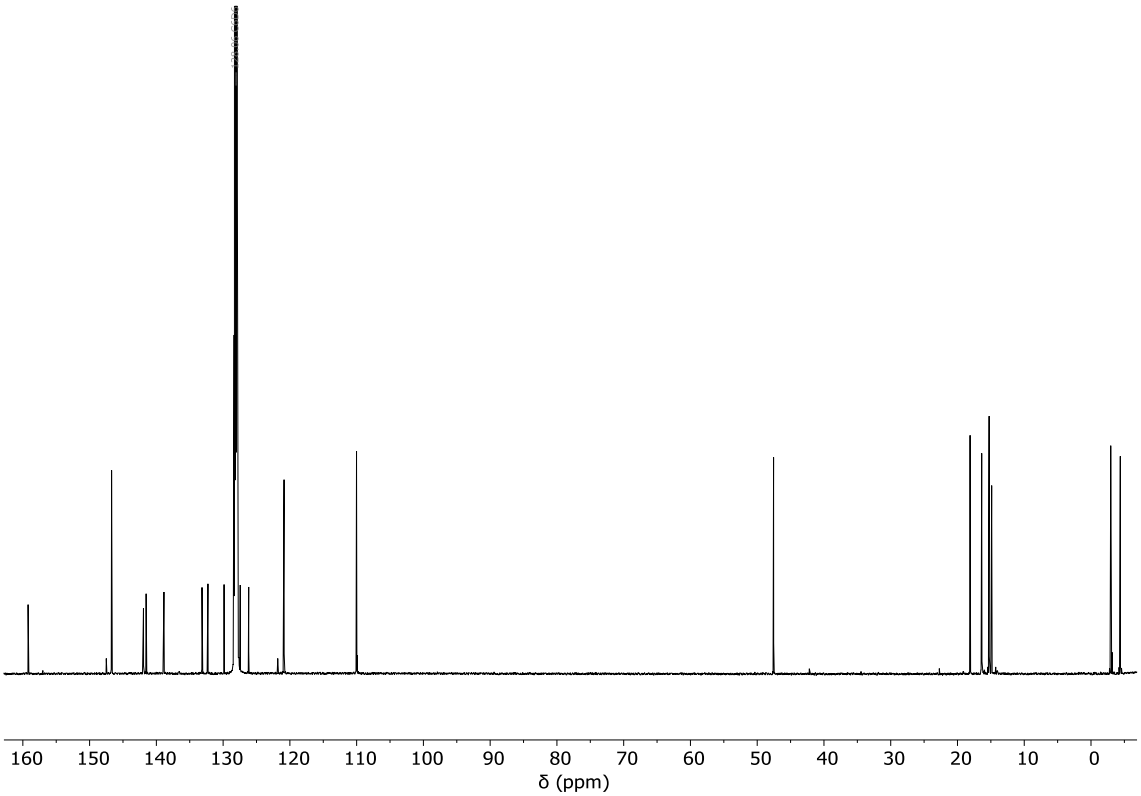


Figure A.13 ^{13}C{^{1}H} NMR spectrum (benzene-d_6, 400 MHz, 298 K) of ^{Me_2}SB(I*,OC_4H_3)H.

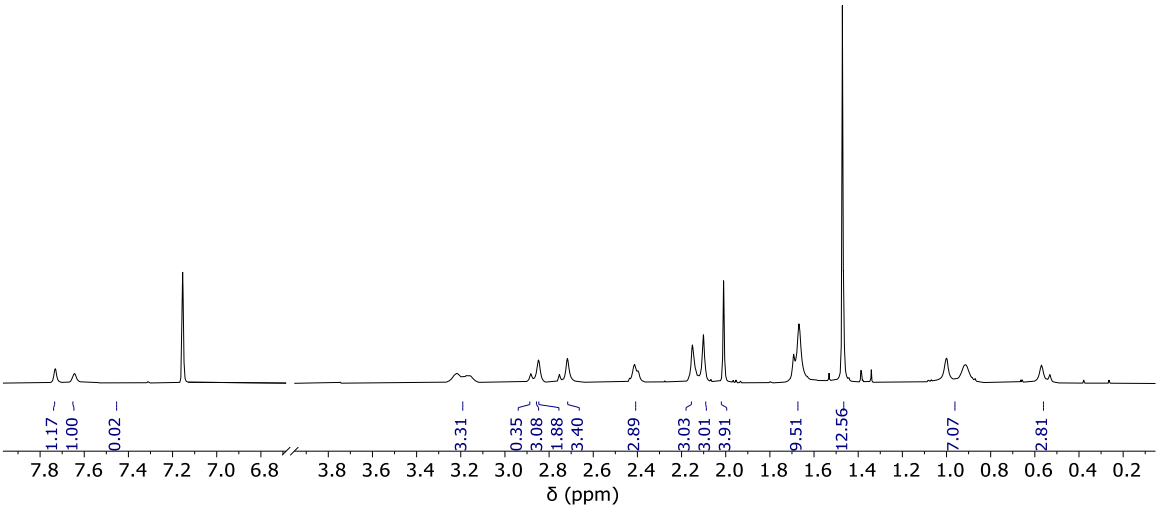


Figure A.14 ^{1}H NMR spectrum (benzene-d_6, 500 MHz, 298 K) of ^{Me_2}SB($^{t Bu_2}$ArO,I*)Sc(Cl).THF (**1**).

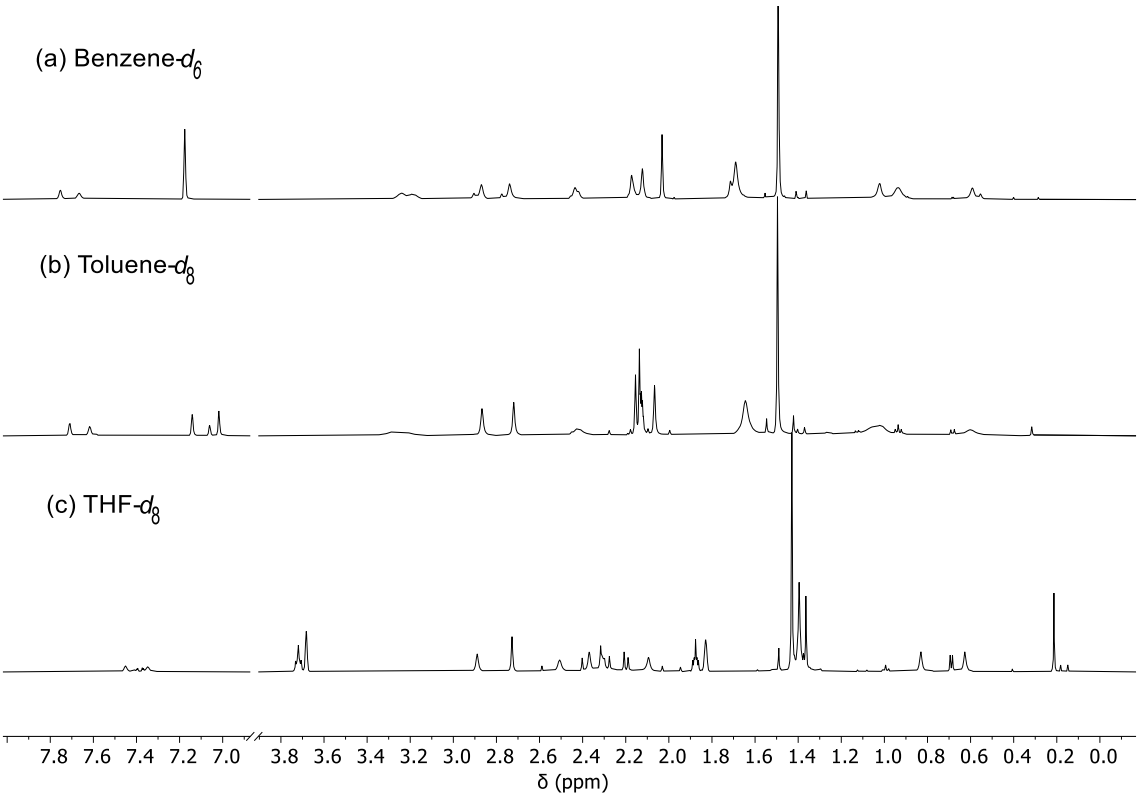


Figure A.15 ^{1}H NMR spectrum ((a) benzene-d_6, (b) toluene-d_8, (c) THF-d_8, 500 MHz, 298 K) of ^{Me_2}SB($^{t Bu_2}$ArO,I*)Sc(Cl).THF (**1**).

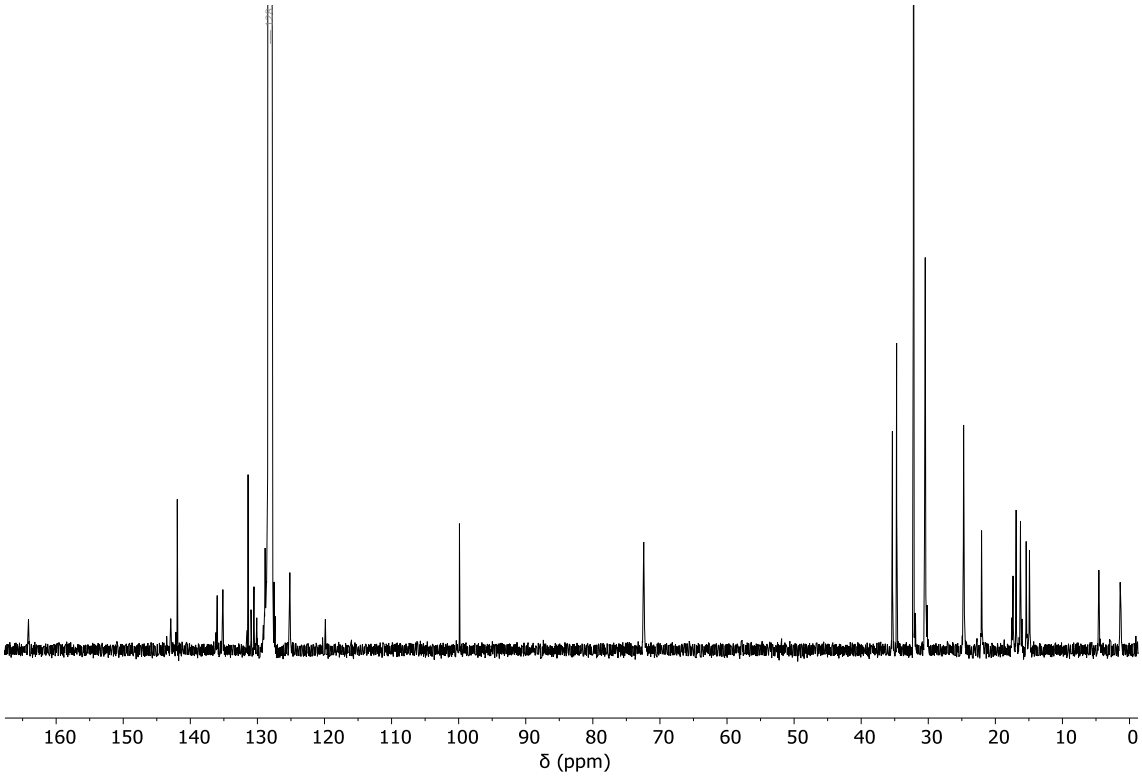


Figure A.16 $^{13}C\{^{1}H\}$ NMR spectrum (benzene-d_6, 126 MHz, 298 K) of ^{Me_2}SB($^{t Bu_2}$ArO,I*)Sc(Cl)THF (**1**).

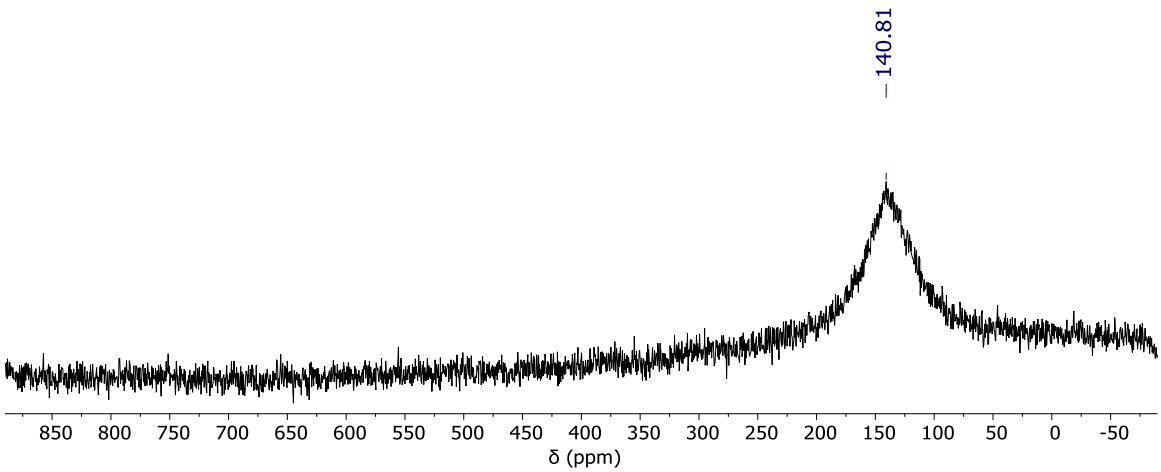


Figure A.17 $^{45}Sc\{^{1}H\}$ NMR spectrum (benzene-d_6, 121.5 MHz, 298 K) of ^{Me_2}SB($^{t Bu_2}$ArO,I*)Sc(Cl)THF (**1**).

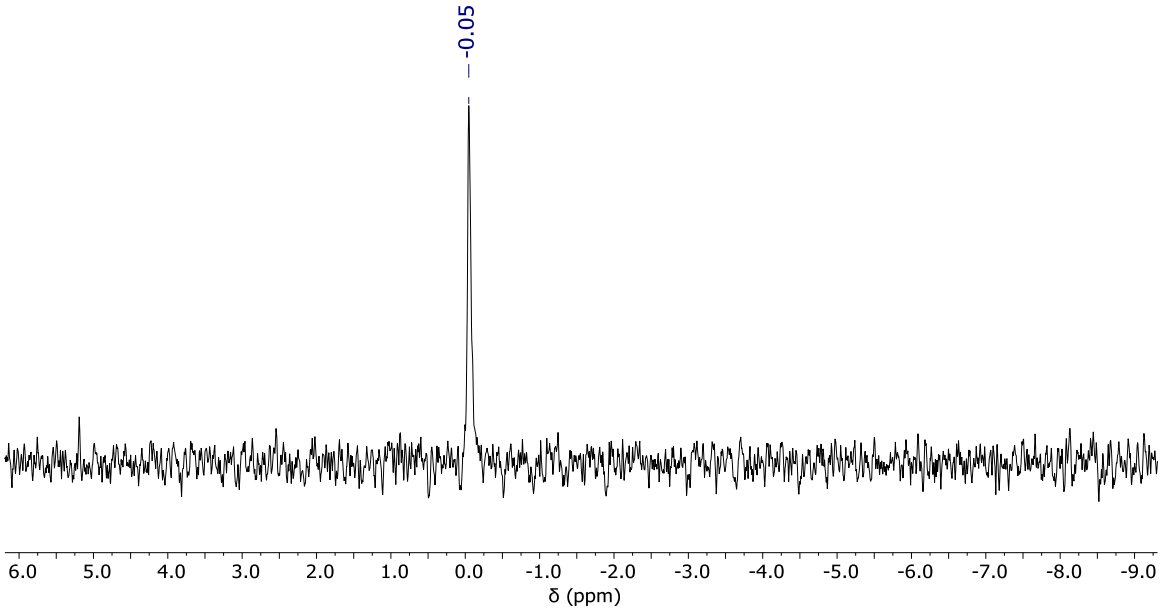


Figure A.18 $^{7}Li\{^{1}H\}$ NMR spectrum (toluene-d_8, 155.5 MHz, 298 K) of $^{Me_2}SB(^{t Bu_2}ArO,I^*)Sc(Cl)THF$ (**1**).

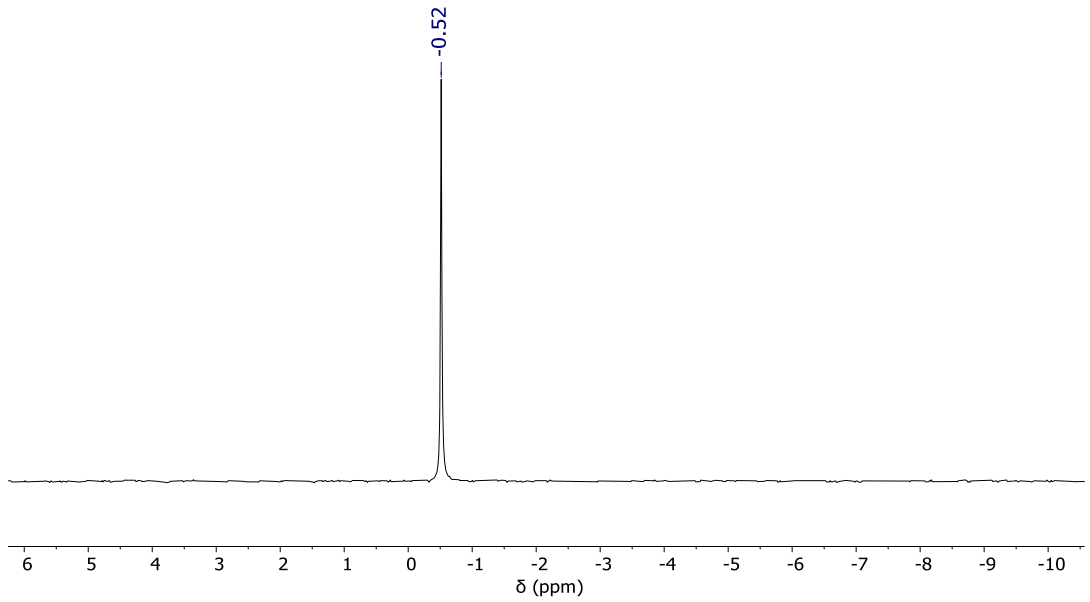


Figure A.19 $^{7}Li\{^{1}H\}$ NMR spectrum (THF-d_8, 155.5 MHz, 298 K) of $^{Me_2}SB(^{t Bu_2}ArO,I^*)Sc(Cl)THF$ (**1**).

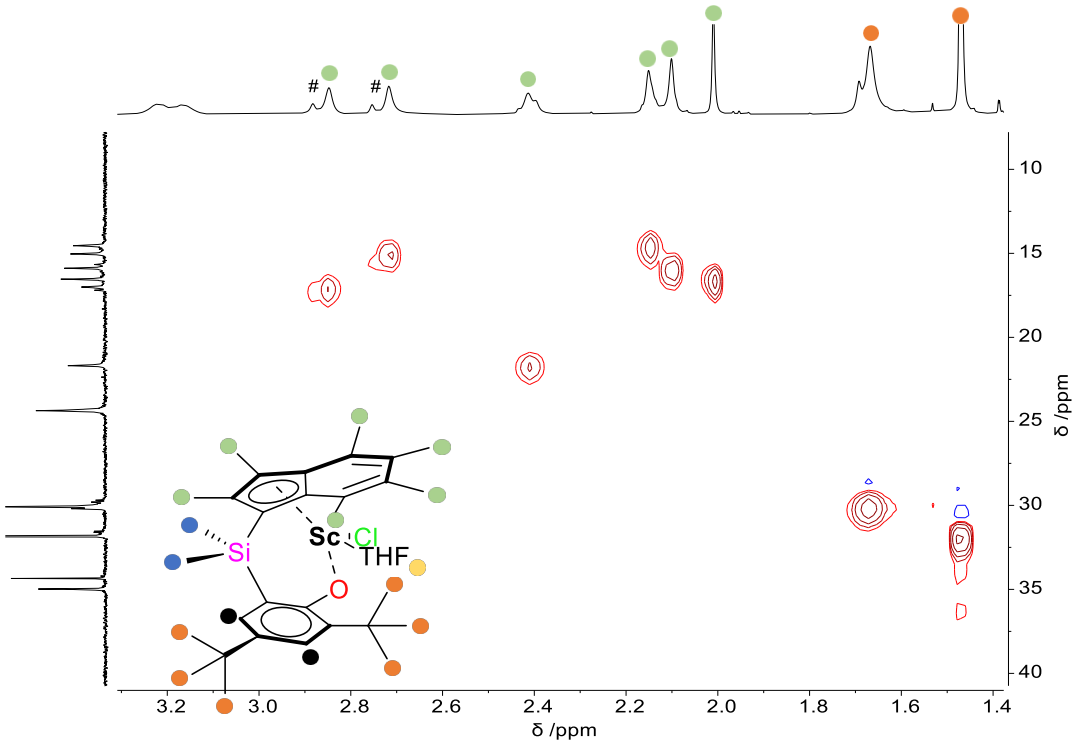


Figure A.20 ^{1}H-^{13}C HSQC NMR spectrum (benzene-d_6, 500 MHz, 298 K) of ^{Me_2}SB($^{t Bu_2}$ArO,I*)Sc(Cl)THF (**1**) plotted to show the I*Me region and corresponding minor resonances. The hash (#) denotes minor resonances

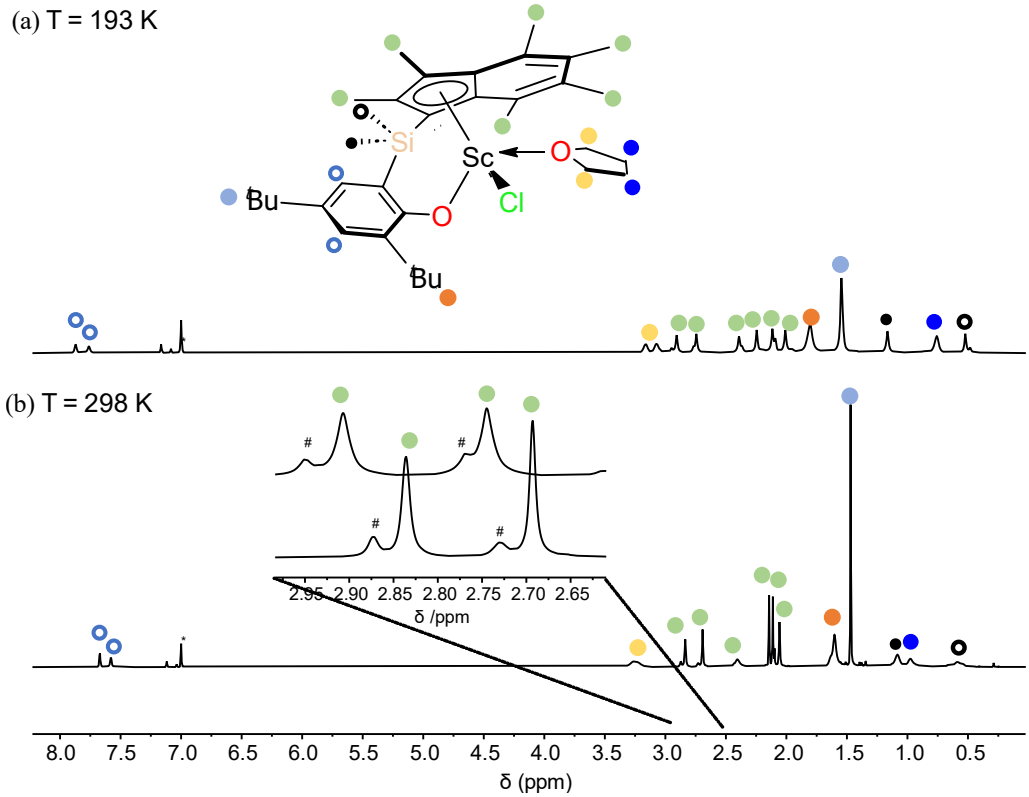


Figure A.21 Variable temperature ^{1}H NMR spectrum (toluene-d_8, 500 MHz) of ^{Me_2}SB($^{t Bu_2}$ArO,I*)Sc(Cl)THF (1) (a) T = 193 K & (b) T = 298 K. # denotes the minor I*Me rotamer.

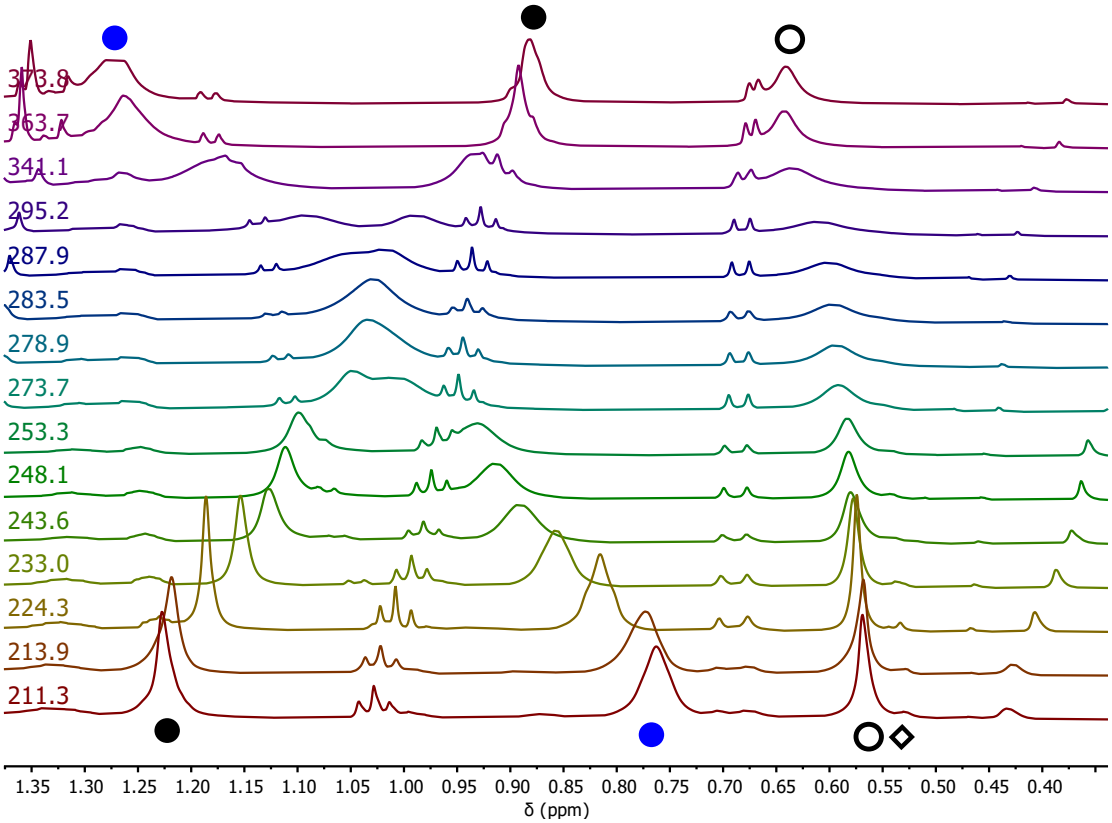


Figure A.22 ^{1}H NMR spectrum (toluene-d_8, 500 MHz) of ^{Me_2}SB($^{t Bu_2}$ArO,I*)Sc(Cl)THF (**1**) in Si*Me* region δ 1.40–0.35 ppm

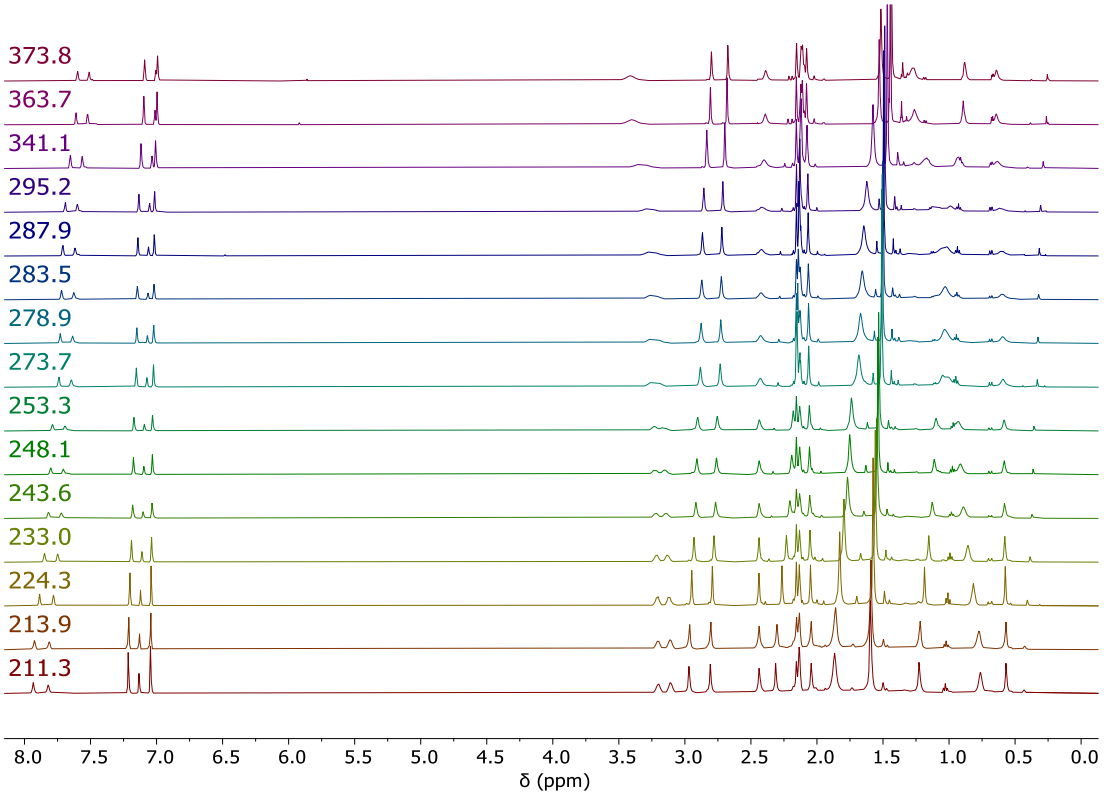


Figure A.23 Variable temperature ^{1}H NMR spectrum (toluene-d_8, 500 MHz) of ^{Me_2}SB($^{t Bu_2}$ArO,I*)Sc(Cl)THF (**1**) between 210–374 K

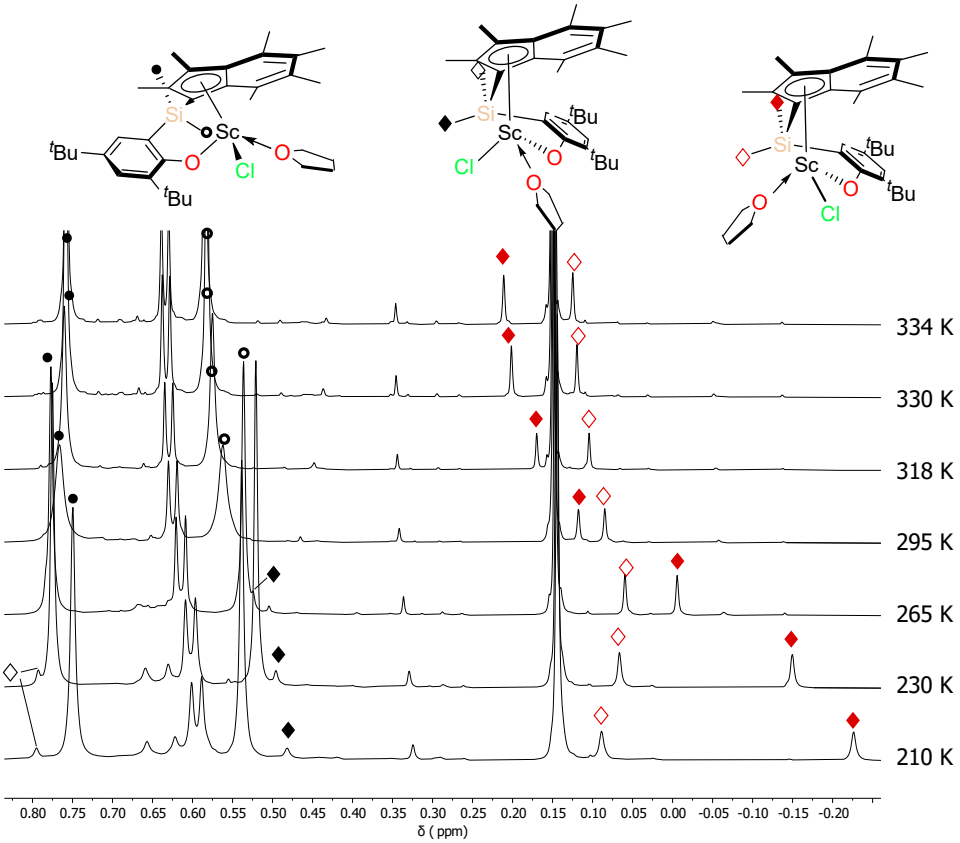


Figure A.24 Variable temperautre ^{1}H NMR spectrum (THF-d_8, 500 MHz) of ^{Me_2}SB(^{tBu_2}ArO,I*)Sc(Cl)THF (**1**) in Si*Me* region (δ 0.80– −0.30 ppm) between 210.0–334.9 K

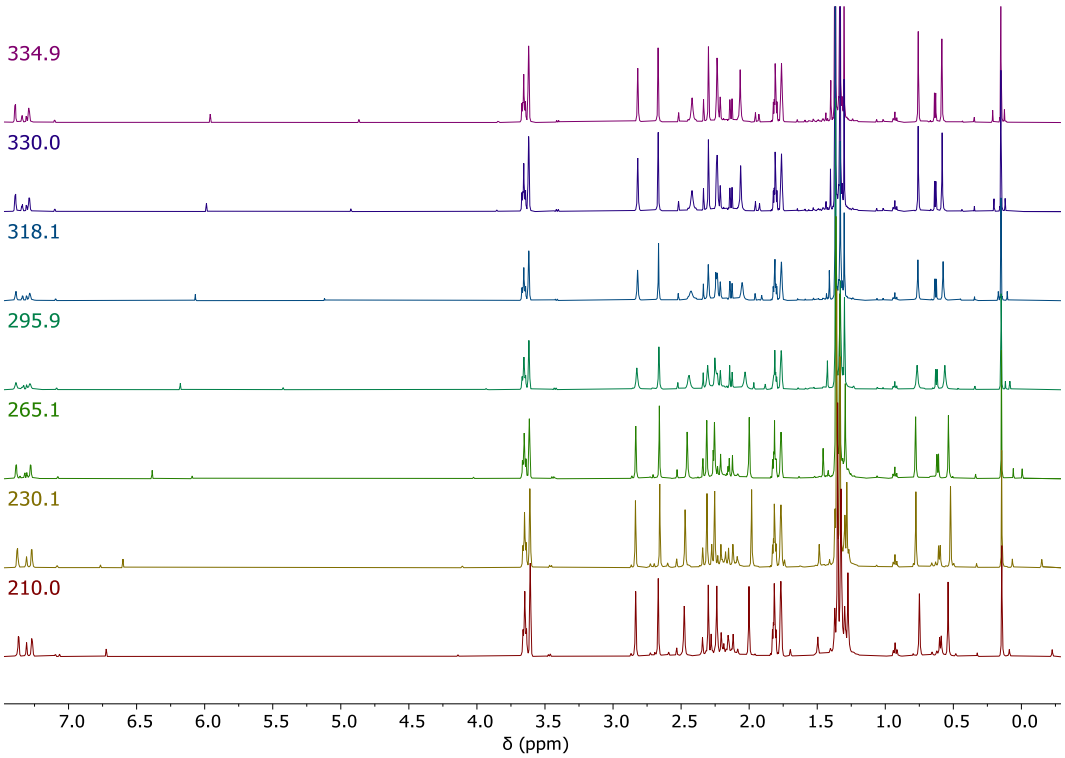


Figure A.25 ^{1}H NMR spectrum (THF-d_8, 500 MHz) of ^{Me_2}SB(^{tBu_2}ArO,I*)Sc(Cl)THF (**1**) between 210.0–334.9 K

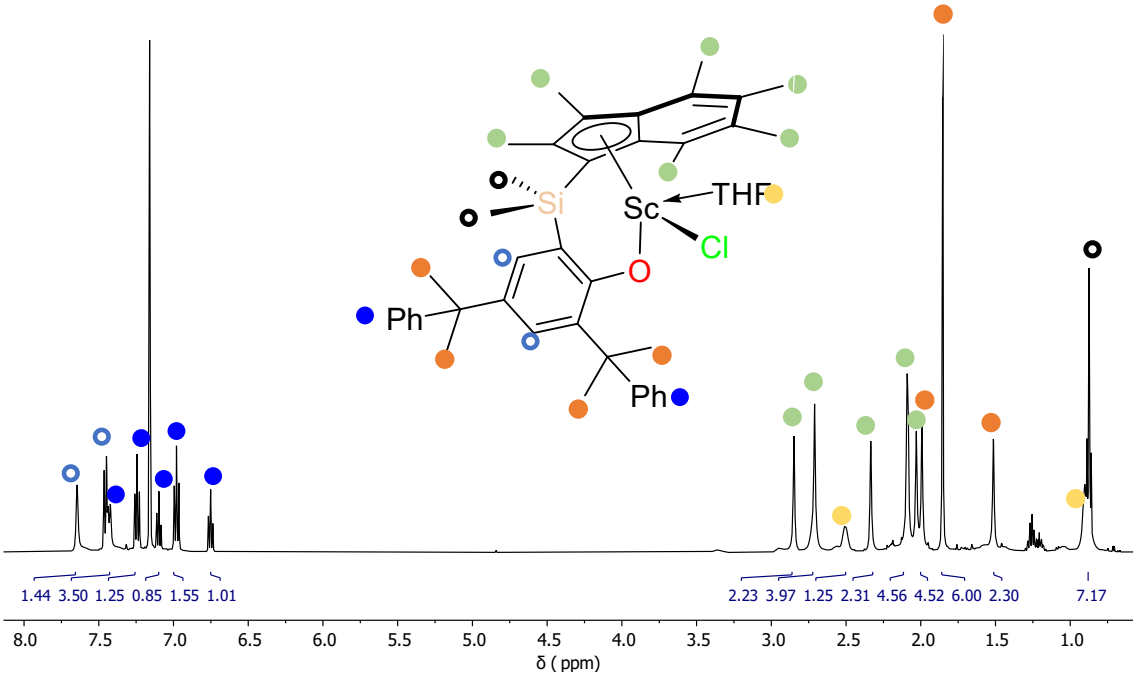


Figure A.26 ^{1}H NMR spectrum (benzene-d_6, 500 MHz, 298 K) of ^{Me_2}SB(^{Cumyl_2}ArO,I*)Sc(Cl)THF (**2**).

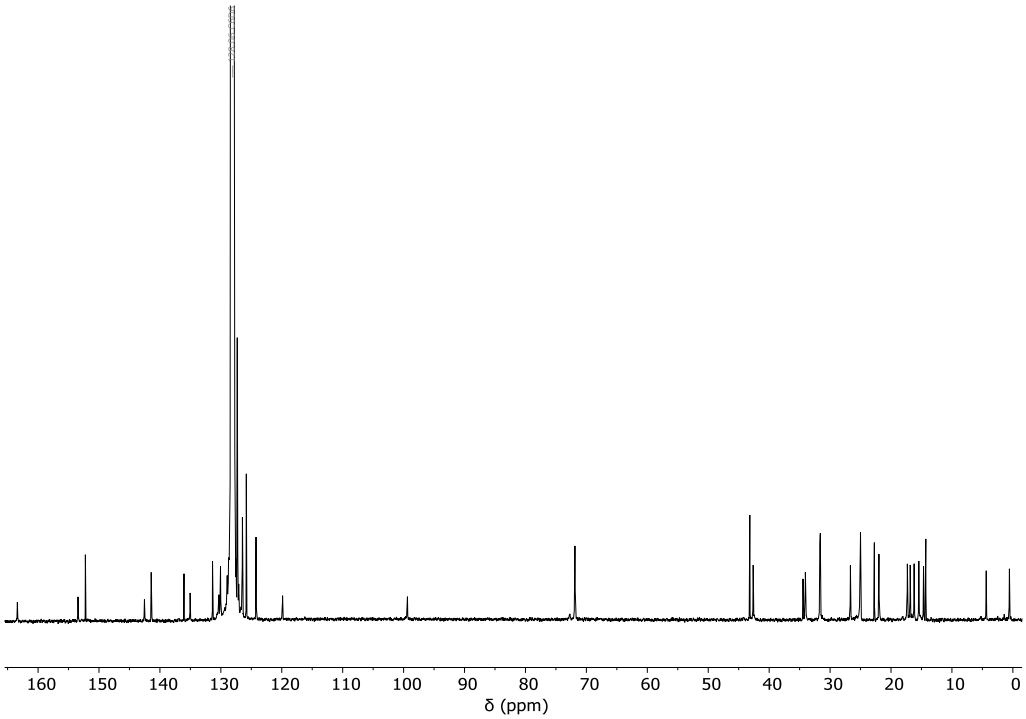


Figure A.27 ^{13}C{^{1}H} NMR spectrum (benzene-d_6, 126 MHz, 298 K) of ^{Me_2}SB(^{Cumyl_2}ArO,I*)Sc(Cl)THF (**2**).

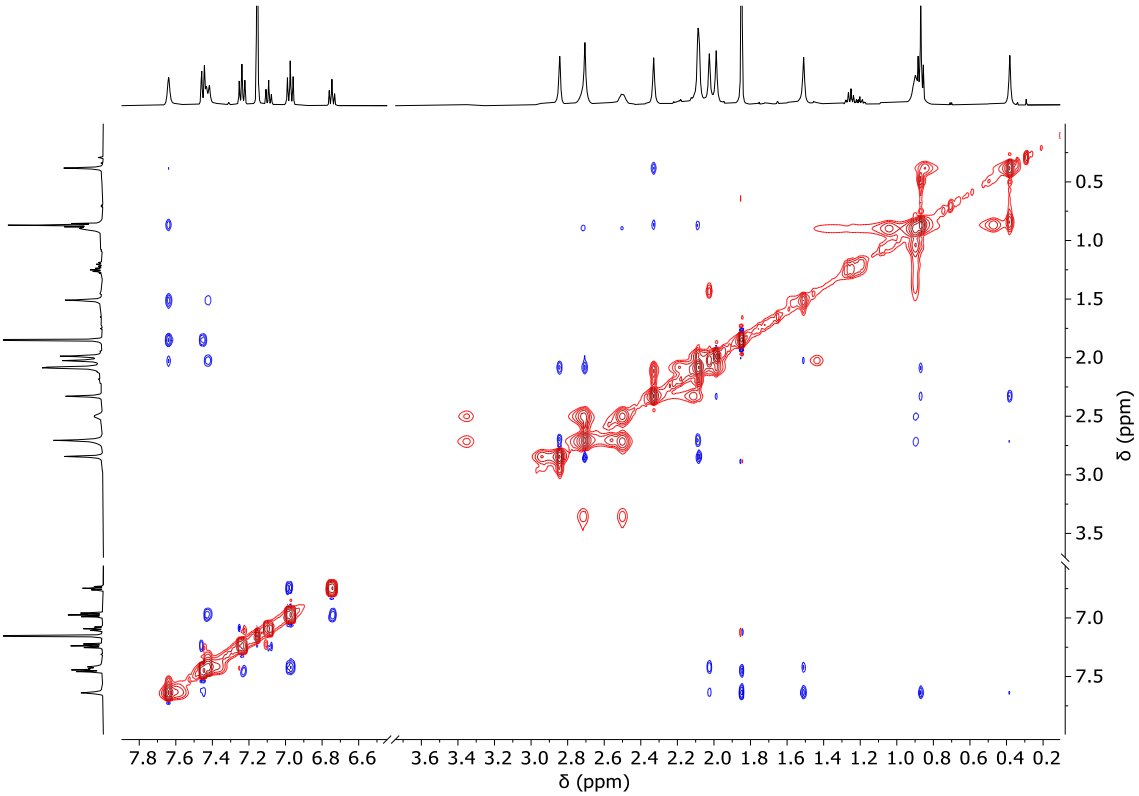


Figure A.28 ^{1}H-^{1}H NOESY spectrum (benzene-d_6, 500 MHz, 298 K) of ^{Me_2}SB(^{Cumyl_2}ArO,I*)Sc(Cl)THF (**2**) Negative (blue) spatial coupling; positive correlation (red) chemical exchange.

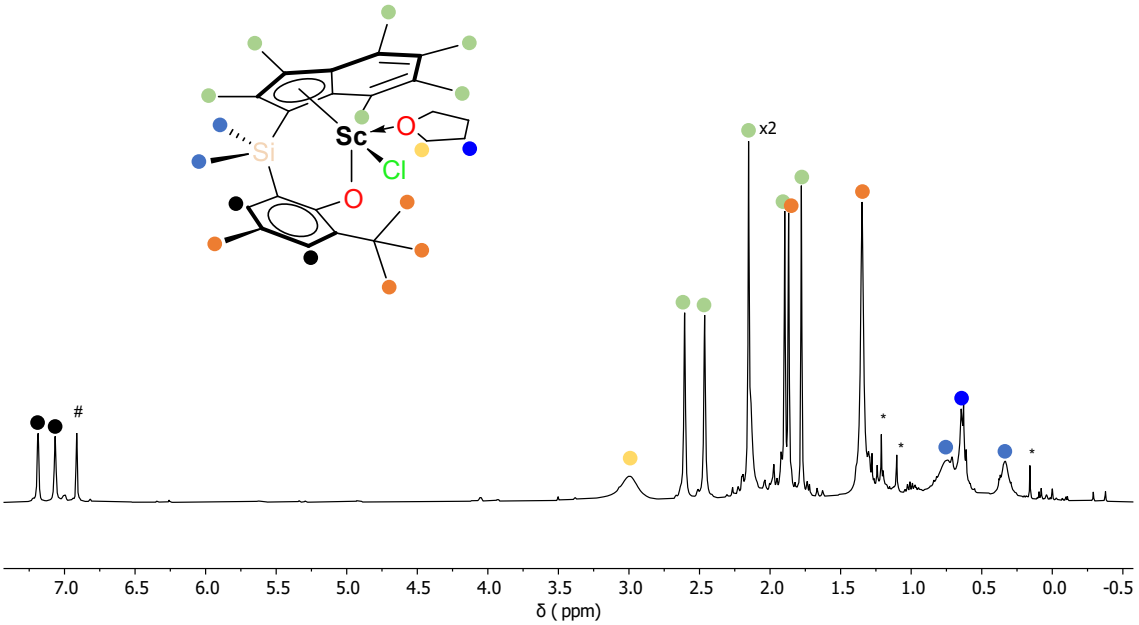


Figure A.29 ^{1}H NMR spectrum (benzene-d_6, 400 MHz, 298 K) of ^{Me_2}SB(^{tBu,Me}ArO,I*)Sc(Cl)THF (**3**).

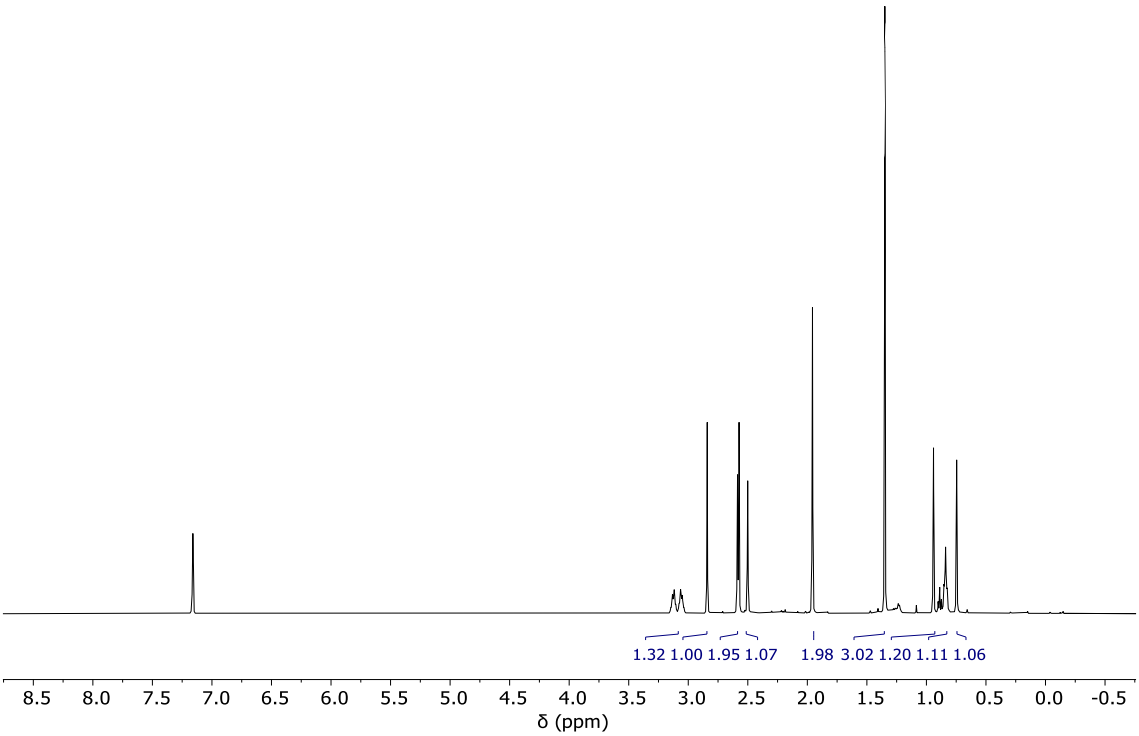


Figure A.30 ^{1}H NMR spectrum (benzene-d_6, 400 MHz, 298 K) ^{Me_2}SB($^{t Bu,}$N,I*)Sc(Cl)THF (**4**).

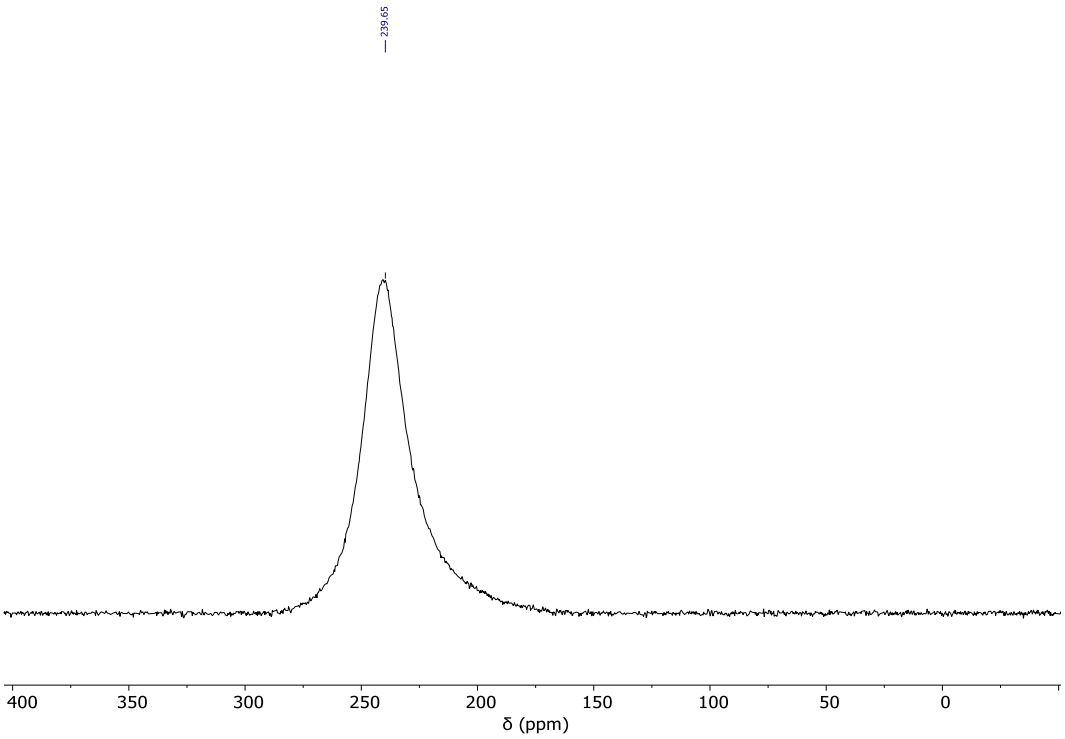


Figure A.31 ^{45}Sc{^{1}H} NMR spectrum (benzene-d_6, 121 MHz, 298 K) of ^{Me_2}SB($^{t Bu,}$N,I*)Sc(Cl)THF (**4**)

δ 239.65 ppm.

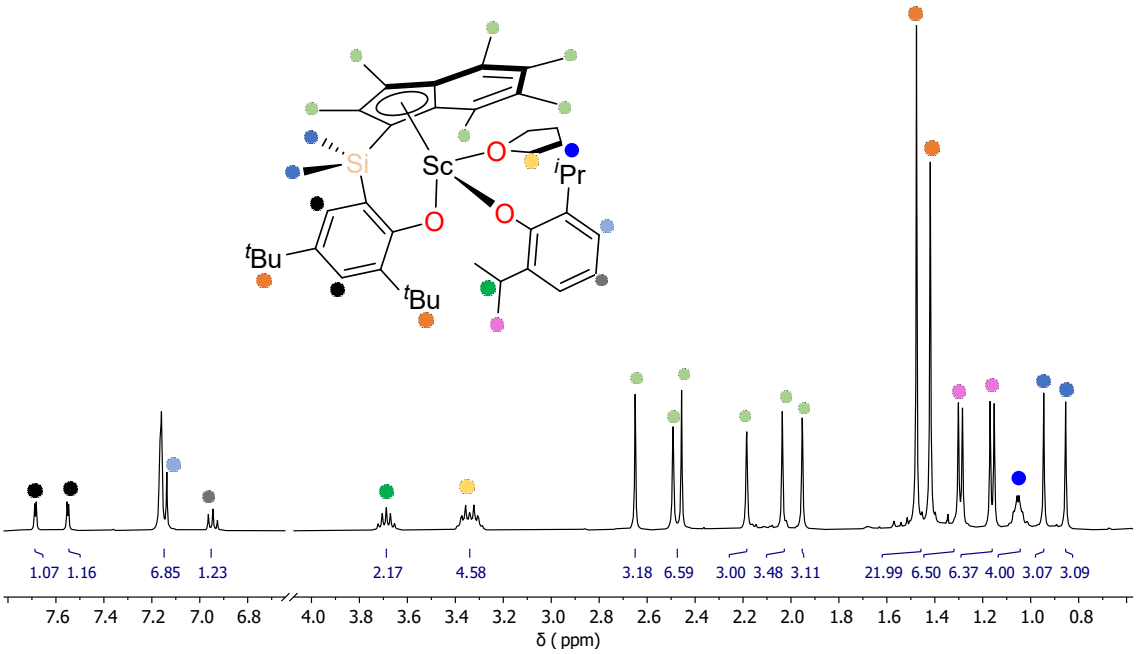


Figure A.32 ^{1}H NMR spectrum (benzene-d_6, 400 MHz, 298 K) of ^{Me_2}SB($^{t Bu_2}$ArO,I*)Sc(ODipp)THF (**5**).

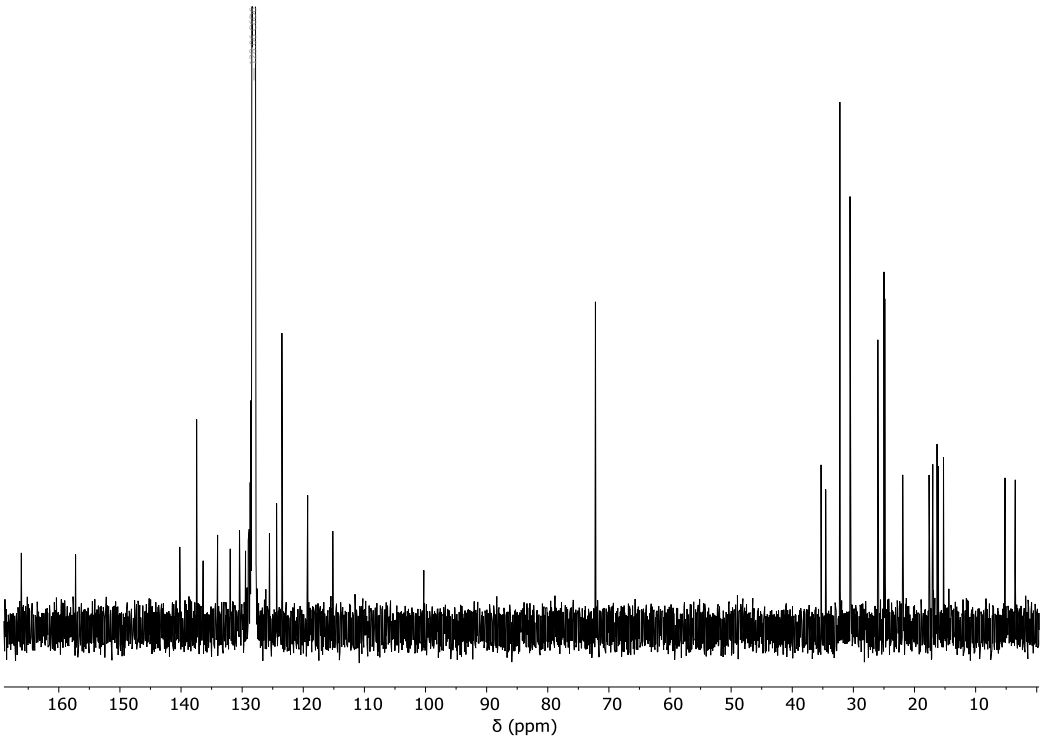


Figure A.33 ^{13}C{^{1}H} NMR spectrum (benzene-d_6, 126 MHz, 298 K) of ^{Me_2}SB($^{t Bu_2}$ArO,I*)Sc(ODipp)THF (**5**).

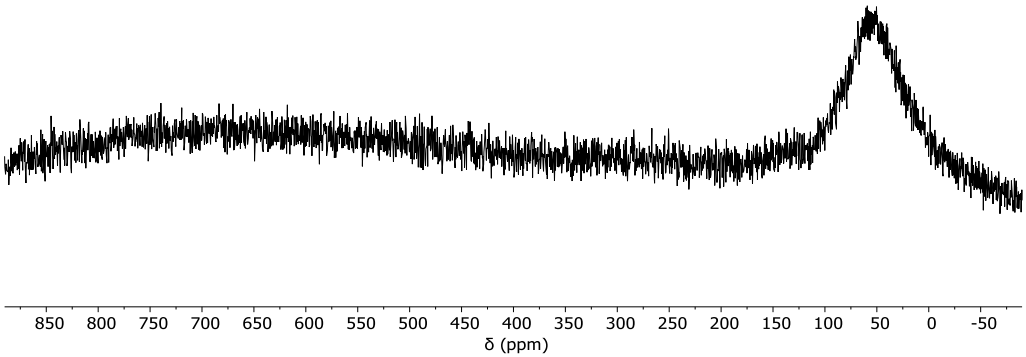


Figure A.34 ^{45}Sc{^{1}H} NMR spectrum (benzene-d_6, 121.5 MHz, 298 K) of ^{Me_2}SB($^{t Bu_2}$ArO,I*)Sc(ODipp)THF (**5**).

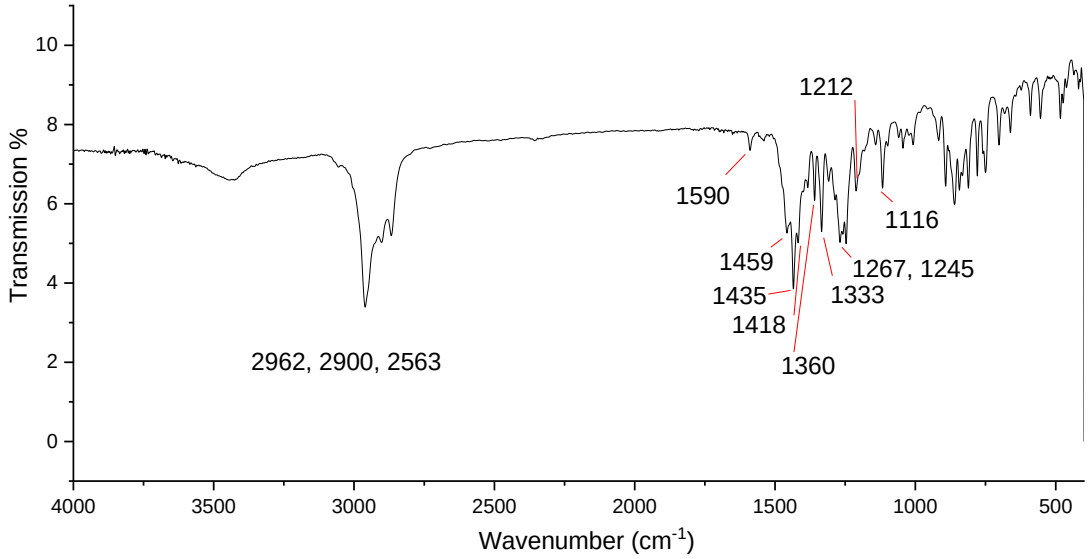


Figure A.35 IR spectrum (KBr disk) of ^{Me_2}SB($^{t Bu_2}$ArO,I*)Sc(ODipp)THF (**5**).4000–450 cm^{-1}

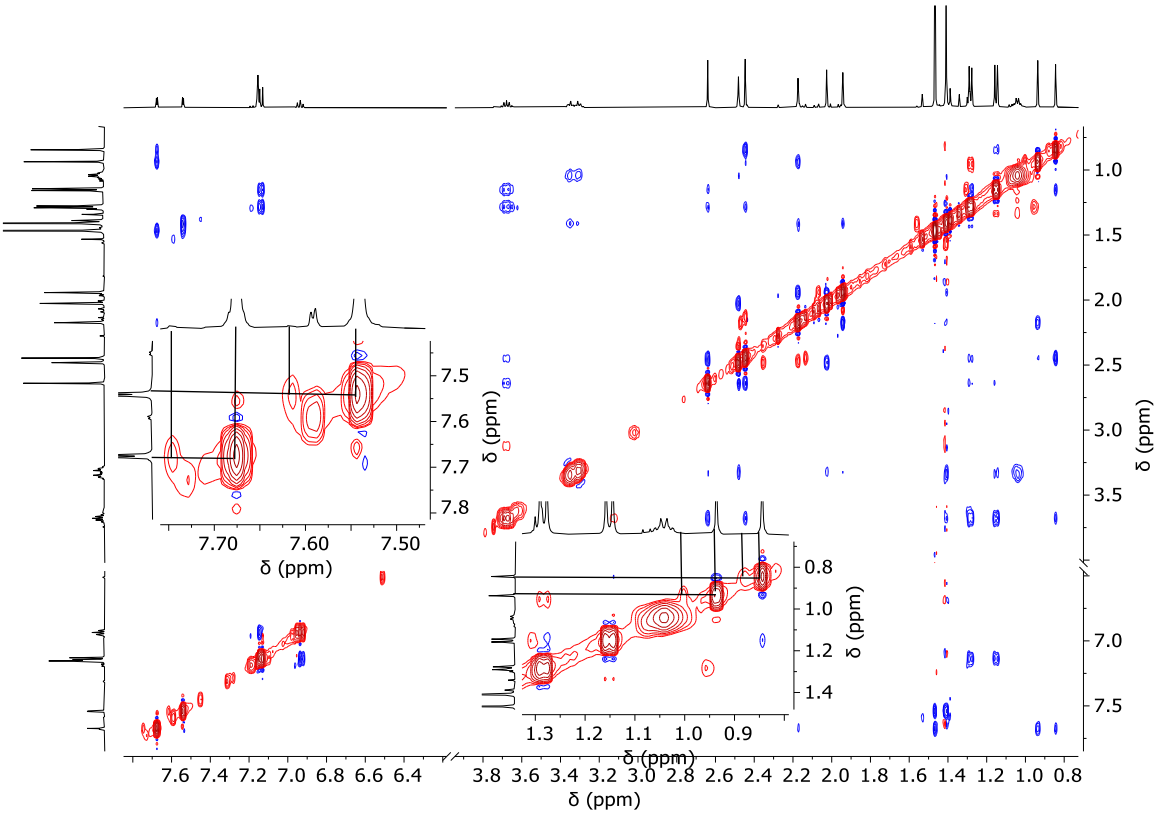


Figure A.36 ^{1}H-^{1}H NOESY spectrum (benzene-d_6, 500 MHz, 298 K) of ^{Me_2}SB(^{t}Bu$_2$ArO,I*)Sc(ODipp)THF (**5**)

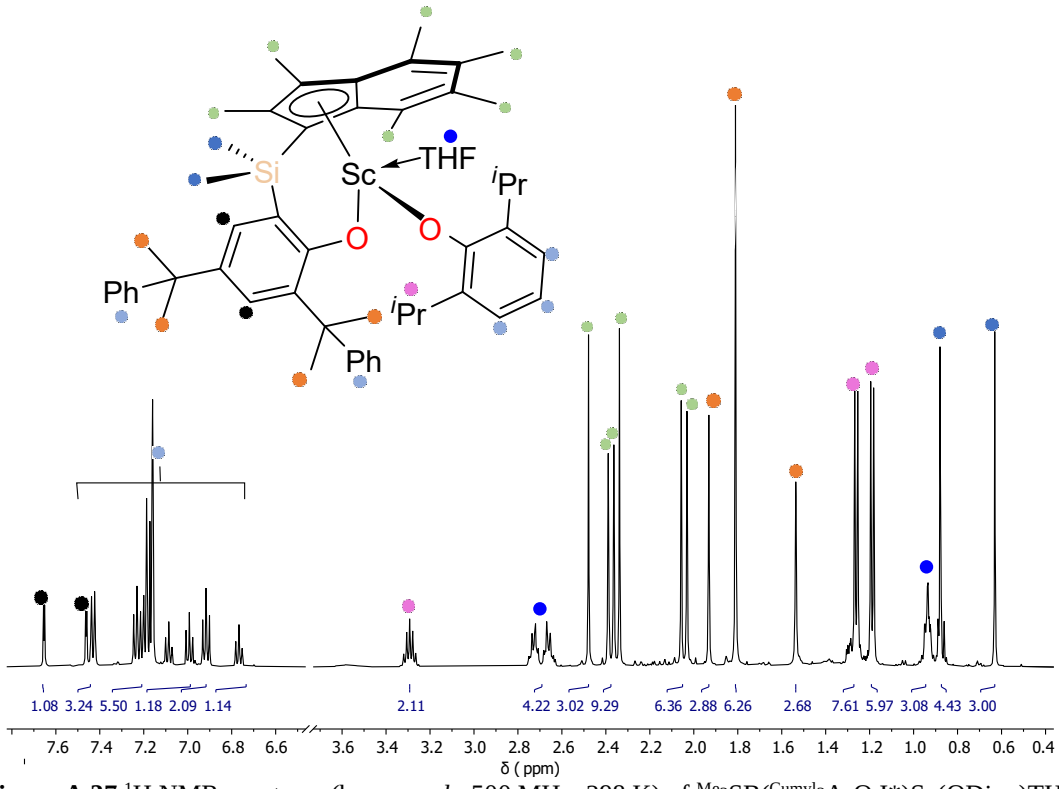


Figure A.37 ^{1}H NMR spectrum (benzene-d_6, 500 MHz, 298 K) of ^{Me_2}SB(^{Cumyl_2}ArO,I*)Sc(ODipp)THF (**6**).

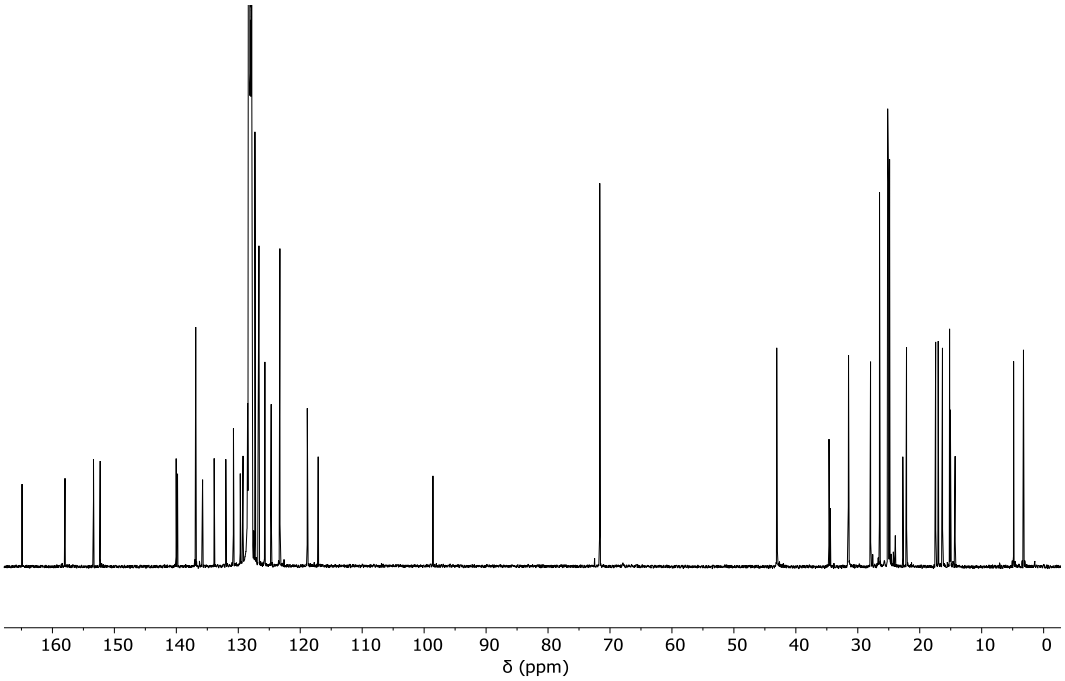


Figure A.38 $^{13}C\{^{1}H\}$ NMR spectrum (benzene-d_6, 126 MHz, 298 K) of $^{Me_2}SB(^{Cumyl_2}ArO,I^*)Sc(ODipp)THF$ (**6**).

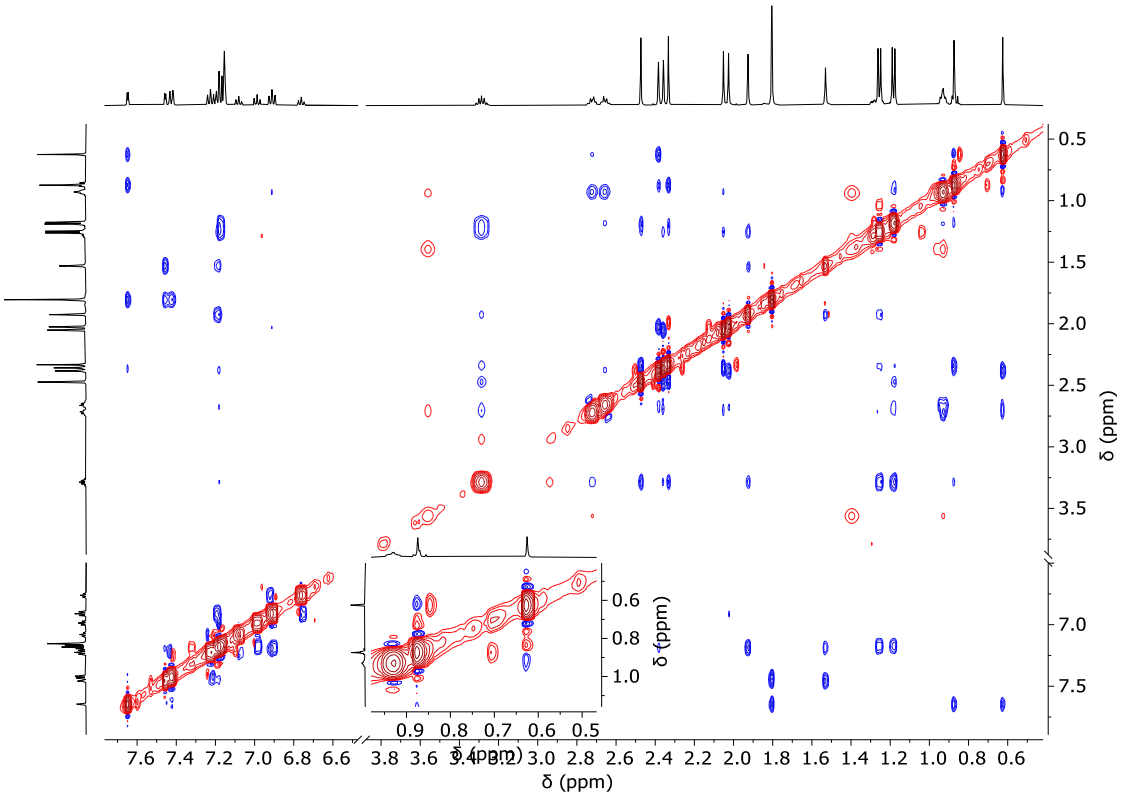


Figure A.39 ^{1}H-^{1}H NOESY spectrum (benzene-d_6, 500 MHz, 298 K) of $^{Me_2}SB(^{Cumyl_2}ArO,I^*)Sc(ODipp)THF$ (**6**) Negative (blue) spatial coupling; positive correlation (red) chemical exchange

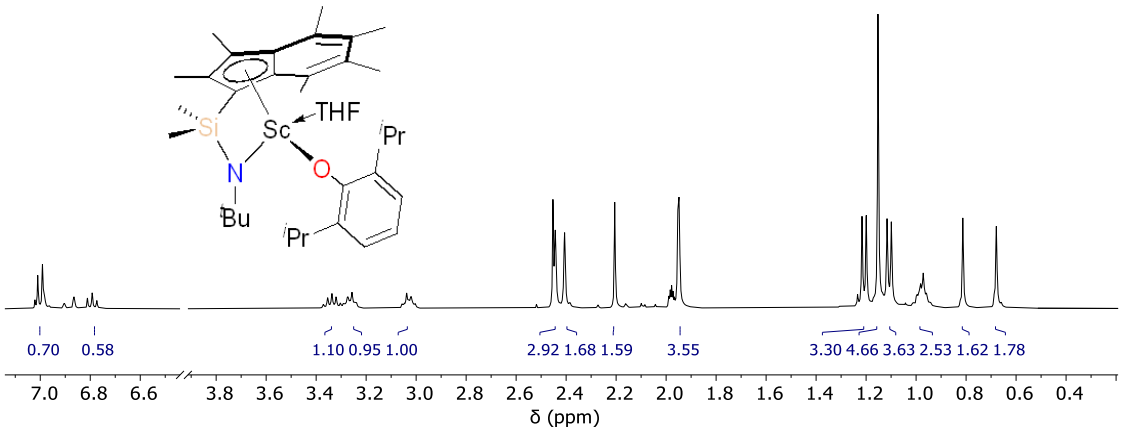


Figure A.40 ^{1}H NMR spectrum (toluene-d_8, 400 MHz, 298 K) ^{Me_2}SB($^{t\text{Bu,}}$N,I*)Sc(ODipp)THF (**7**).

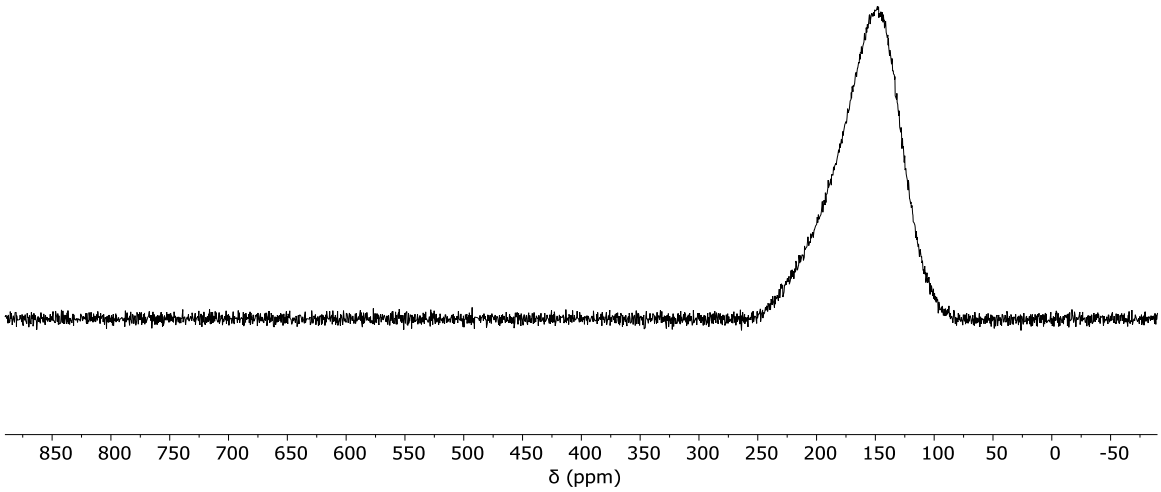


Figure A.41 ^{45}Sc{^{1}H} NMR spectrum (benzene-d_6, 121 MHz, 298 K) of ^{Me_2}SB($^{t\text{Bu}_N}$,I*)Sc(ODipp)THF (**7**) δ 148.23 ppm.

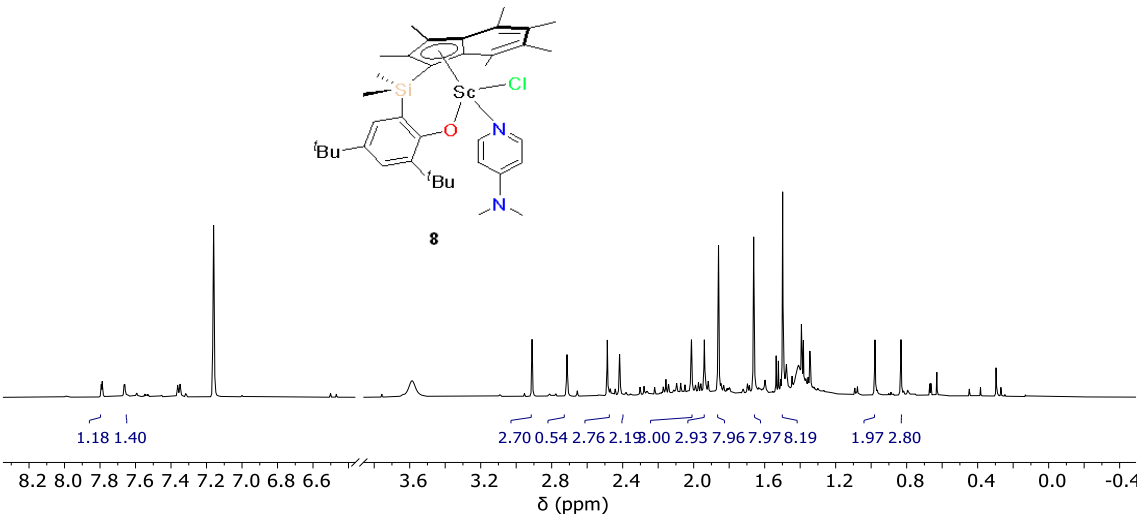


Figure A.42 ^{1}H NMR spectrum (benzene-d_6, 600 MHz, 298 K) of ^{Me_2}SB(^{tBu_2}ArO,I*)Sc(Cl)DMAP (**8**)

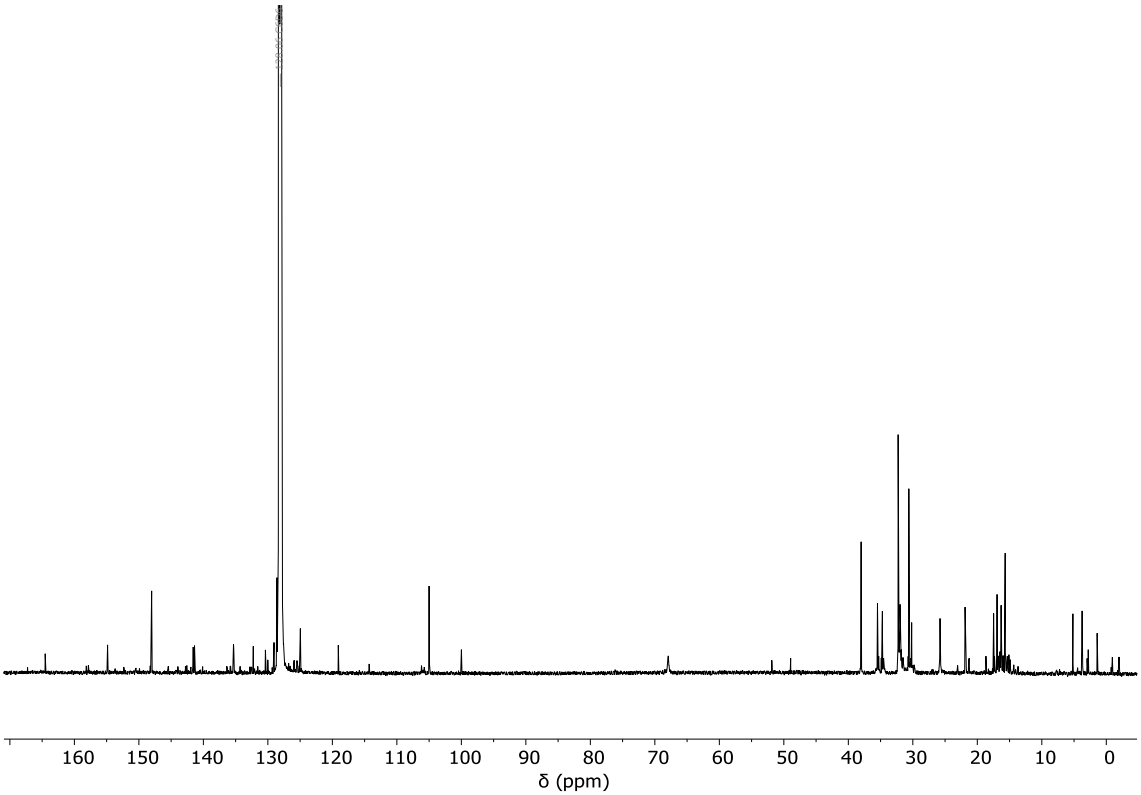


Figure A.43 ^{13}C{^{1}H} NMR spectrum (benzene-d_6, 151 MHz, 298 K) of ^{Me_2}SB(^{tBu_2}ArO,I*)Sc(Cl)DMAP (**8**).

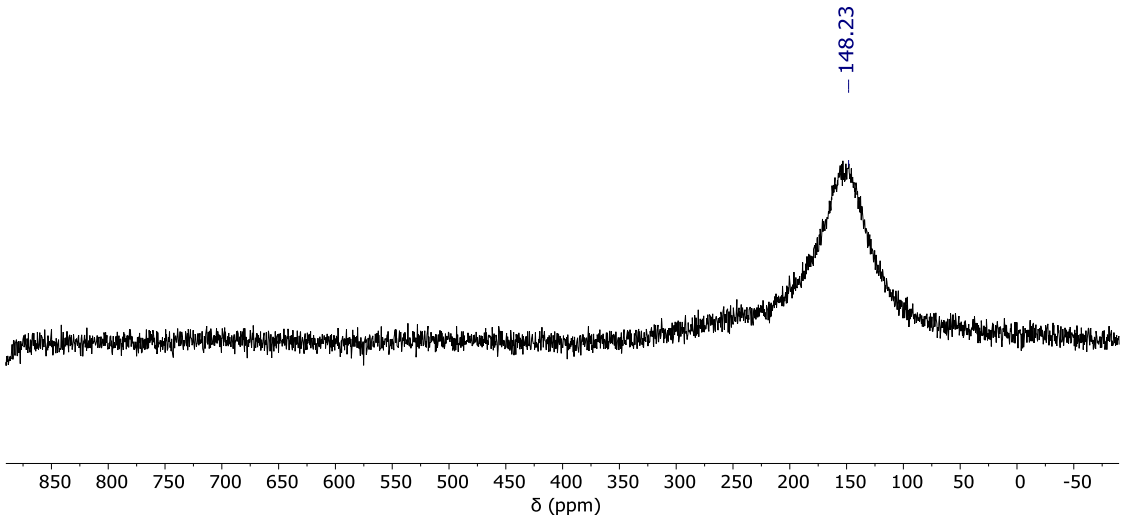


Figure A.44 ^{45}Sc{^{1}H} NMR spectrum (benzene-d_6, 121.5 MHz, 298 K) of ^{Me_2}SB(^{tBu_2}ArO,I*)Sc(Cl)DMAP (**8**).

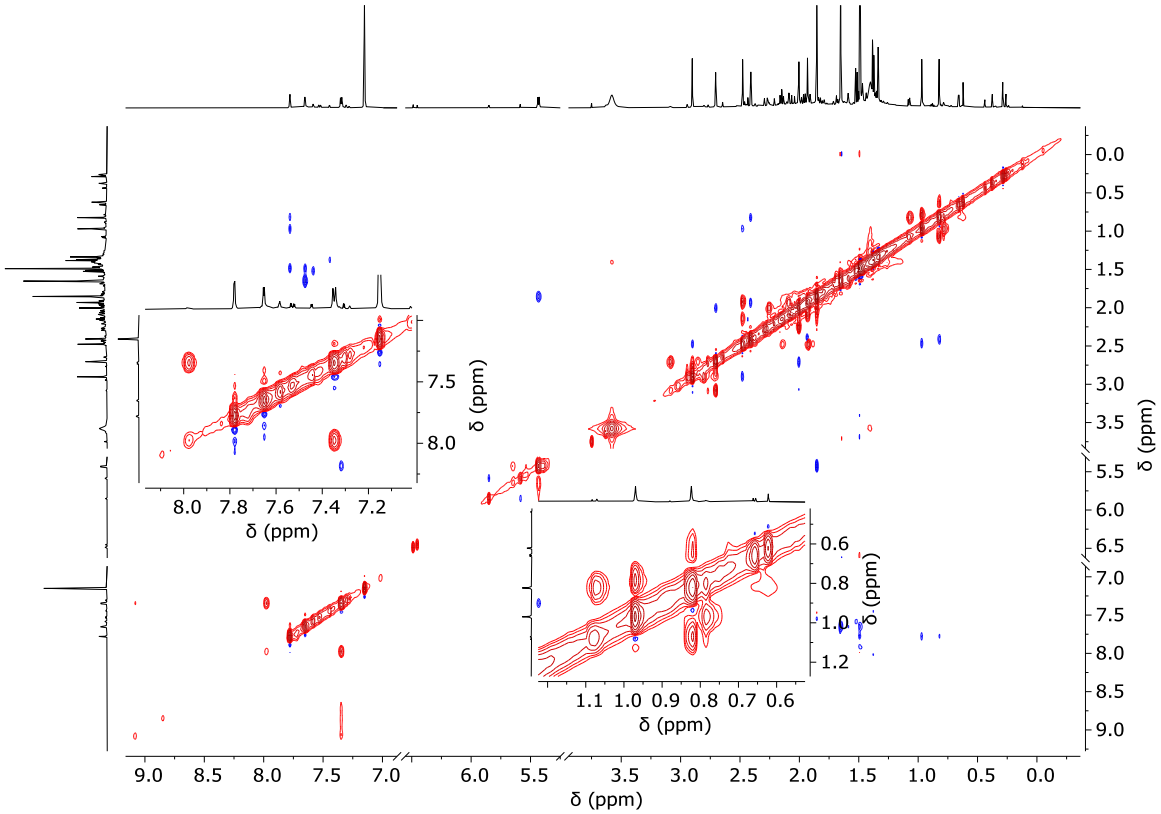


Figure A.45 ^{1}H-^{1}H NOESY spectrum (500 MHz, benzene-d_6, 298 K) of ^{Me_2}SB(^{tBu_2}ArO,I*)Sc(Cl)DMAP (**8**)

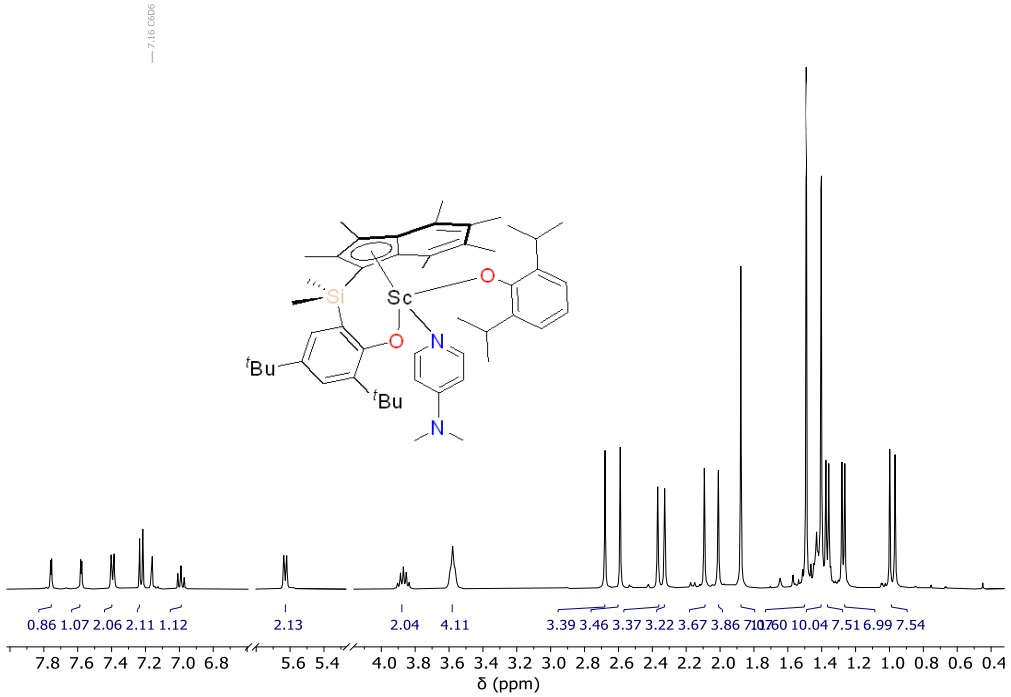


Figure A.46 ^{1}H NMR spectrum (benzene-d_6, 400 MHz, 298 K) ^{Me_2}SB(^{tBu_2}ArO,I*)Sc(ODipp)DMAP (**9**).

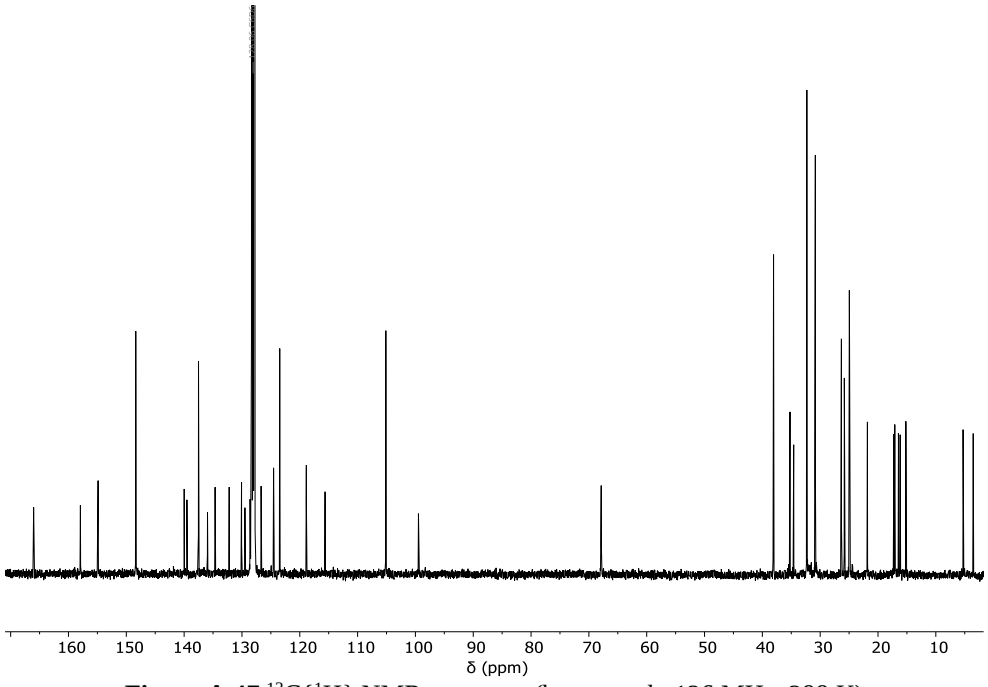


Figure A.47 ^{13}C{^{1}H} NMR spectrum (benzene-d_6, 126 MHz, 298 K) ^{Me_2}SB(^{tBu_2}ArO,I*)Sc(ODipp).DMAP (**9**).

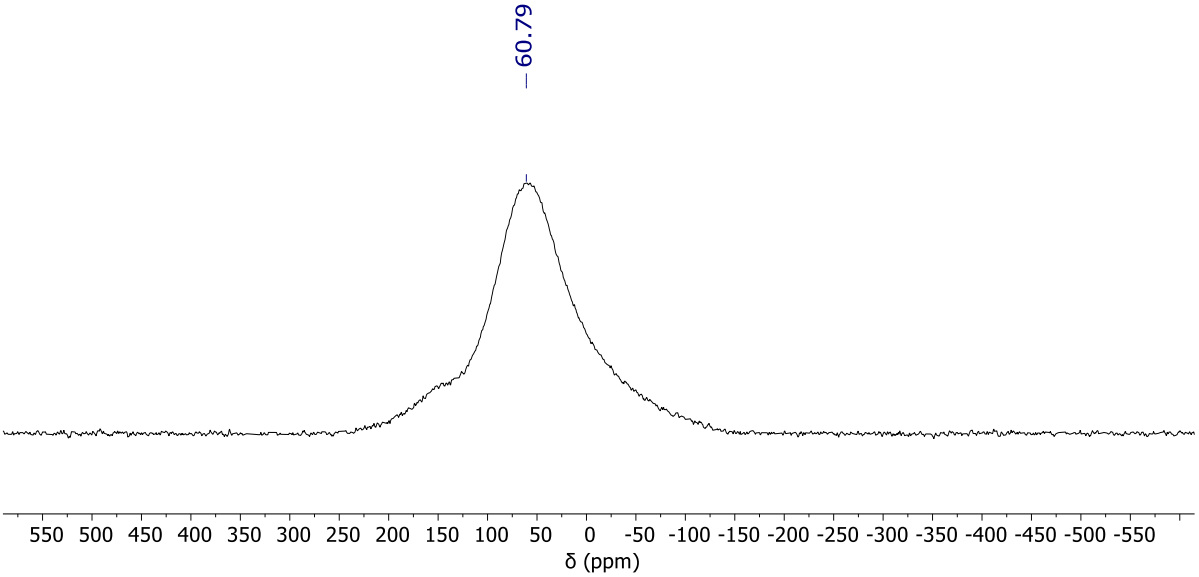


Figure A.48 ^{45}Sc{^{1}H} NMR spectrum (benzene-d_6, 121 MHz, 298 K) of ^{Me_2}SB(^{t}Bu$_2$ArO,I*)Sc(ODipp)DMAP (**9**).

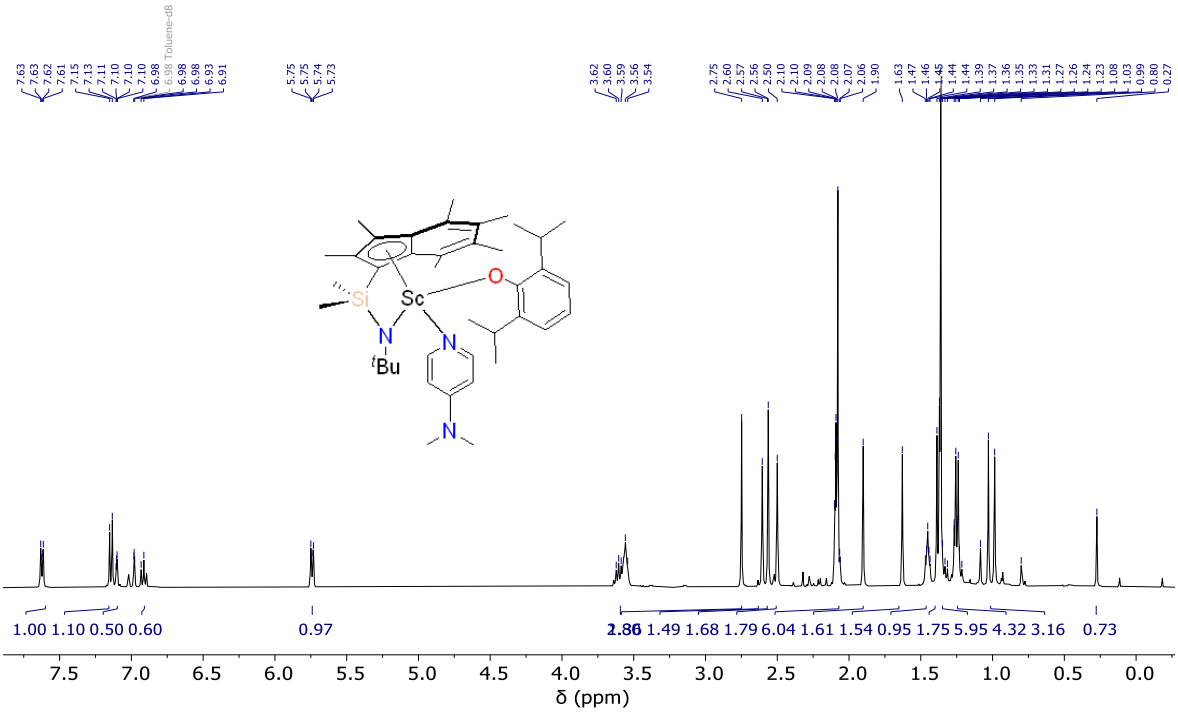


Figure A.49 ^{1}H NMR spectrum (toulene-d_8, 400 MHz, 298 K) of ^{Me_2}SB(^{t}Bu$_N$,I*)Sc(ODipp).DMAP (**10**).

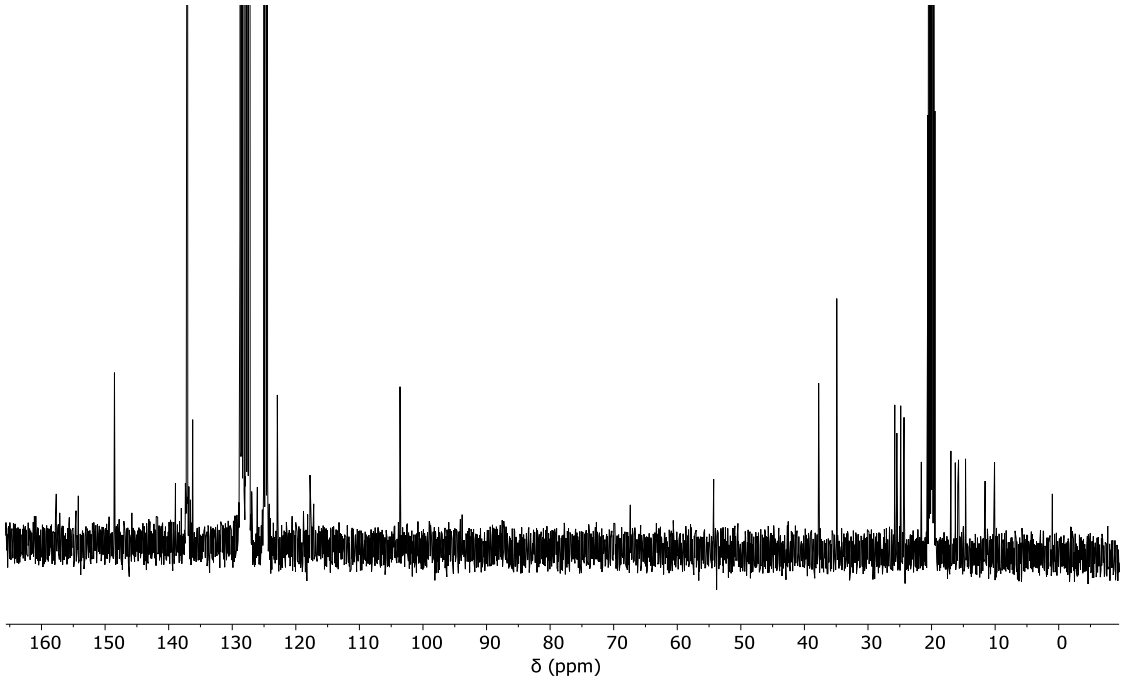


Figure A.50 $^{13}C\{^{1}H\}$ NMR spectrum (toluene-d_8, 101 MHz, 298 K) of ^{Me_2}SB($^{t\text{Bu}}$N,I*)Sc(ODipp)DMAP (**10**).

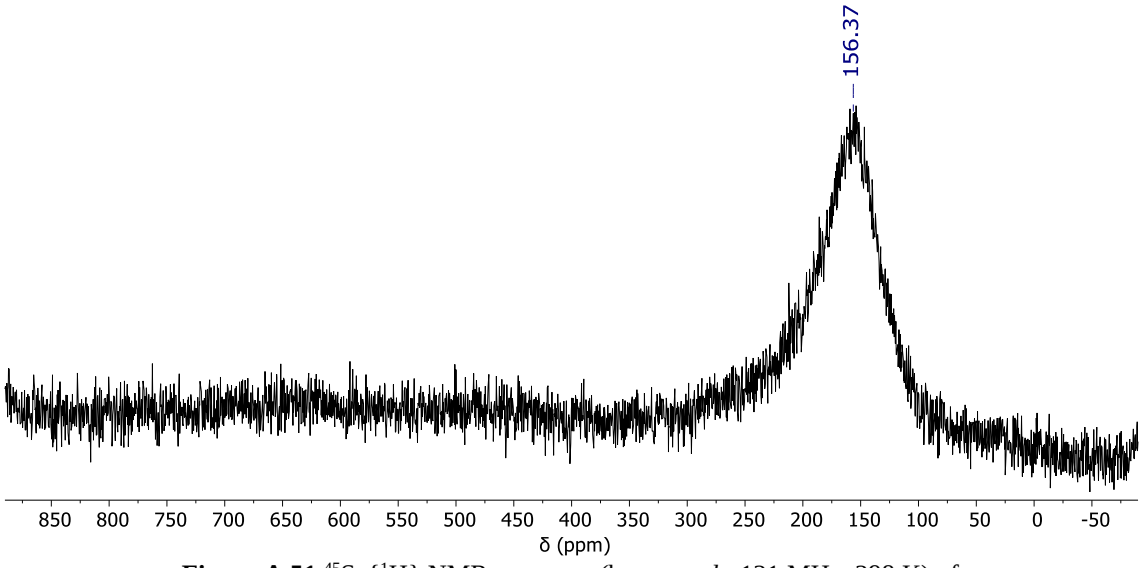


Figure A.51 $^{45}Sc\{^{1}H\}$ NMR spectrum (benzene-d_6, 121 MHz, 298 K) of ^{Me_2}SB($^{t\text{Bu}}$N,I*)Sc(ODipp)DMAP (**10**) δ 156.37 ppm.

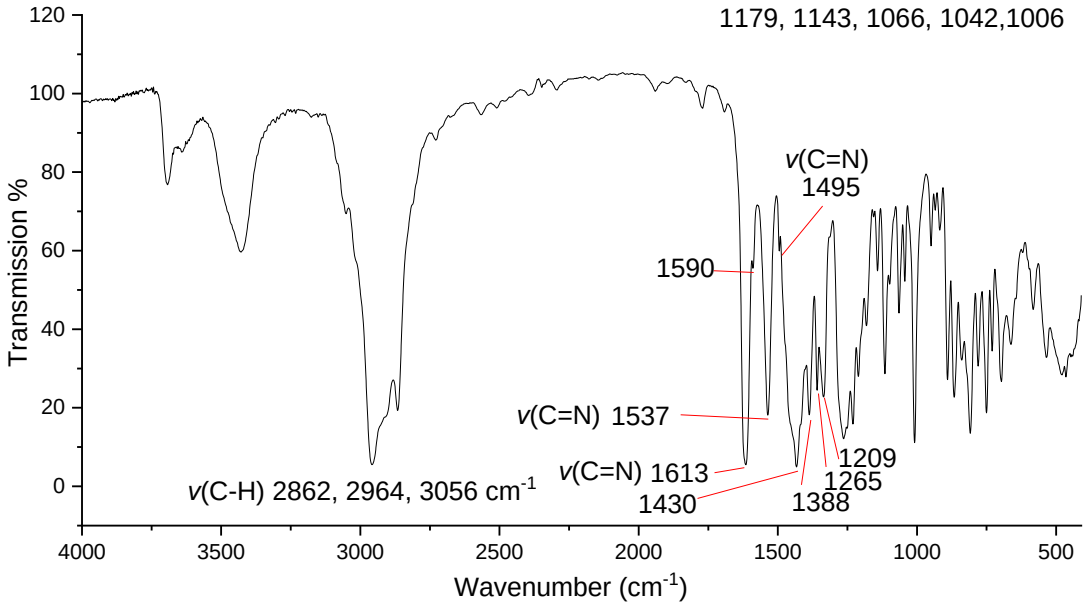


Figure A.52 IR spectrum (KBr disk) of ^{Me_2}SB($^{t Bu}$N,I*)Sc(ODipp)DMAP (**10**) 4000–450 cm^{-1}

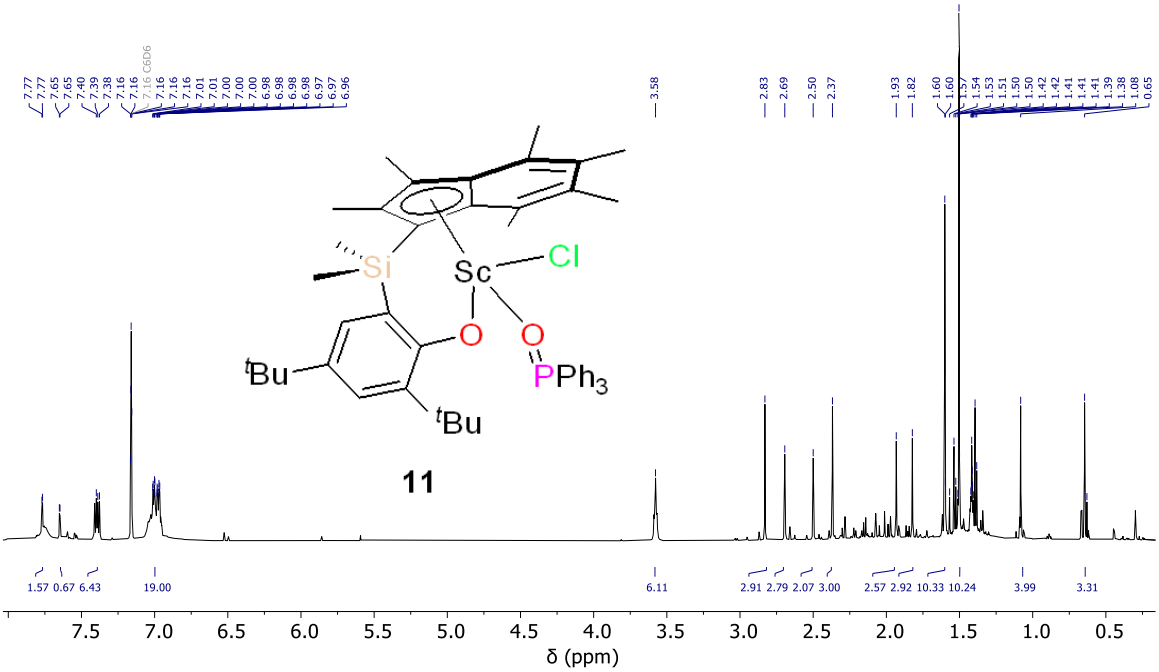


Figure A.53 ^{1}H NMR spectrum (benzene-d_6, 600 MHz, 298 K) of ^{Me_2}SB($^{t Bu_2}$ArO,I*)Sc(Cl)OPPh$_3$ (**11**)

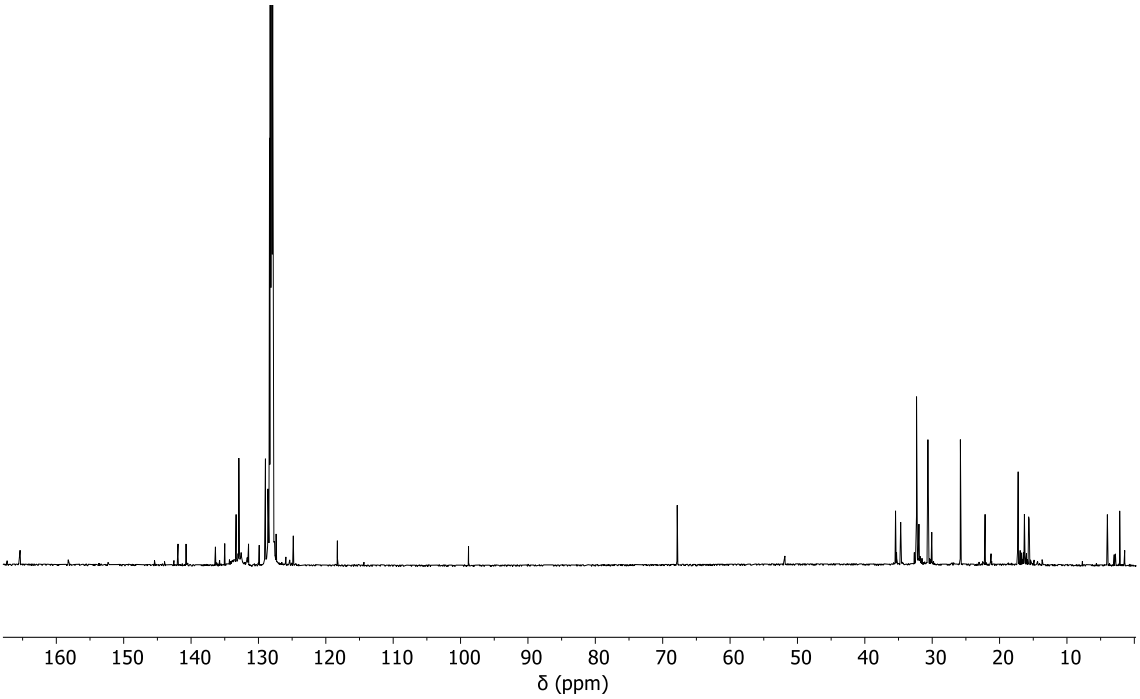


Figure A.54 $^{13}C\{^{1}H\}$ NMR spectrum (benzene-d_6, 151 MHz, 298 K) of $^{Me_2}SB(^{t Bu_2}ArO,I^*)Sc(Cl)OPPh_3$ (**11**).

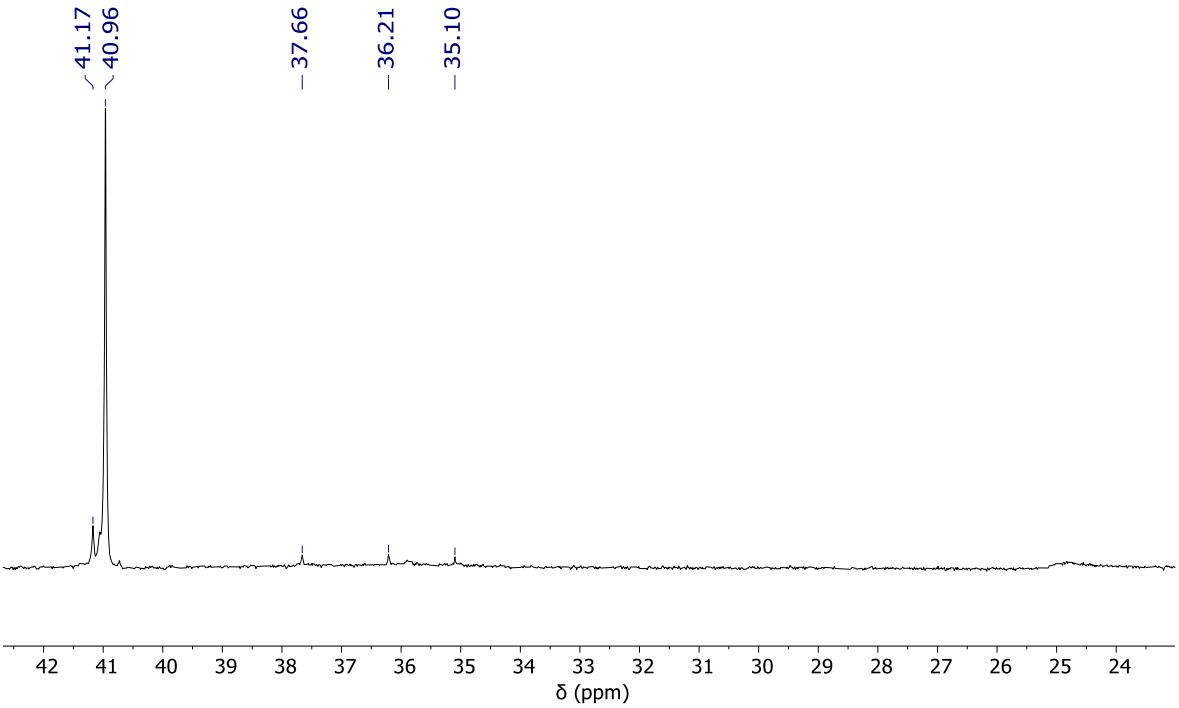


Figure A.55 $^{31}P\{^{1}H\}$ NMR spectrum of $^{Me_2}SB(^{t Bu_2}ArO,I^*)Sc(Cl)OPPh_3$ (**11**) (benzene-d_6, 243 MHz, 298 K).

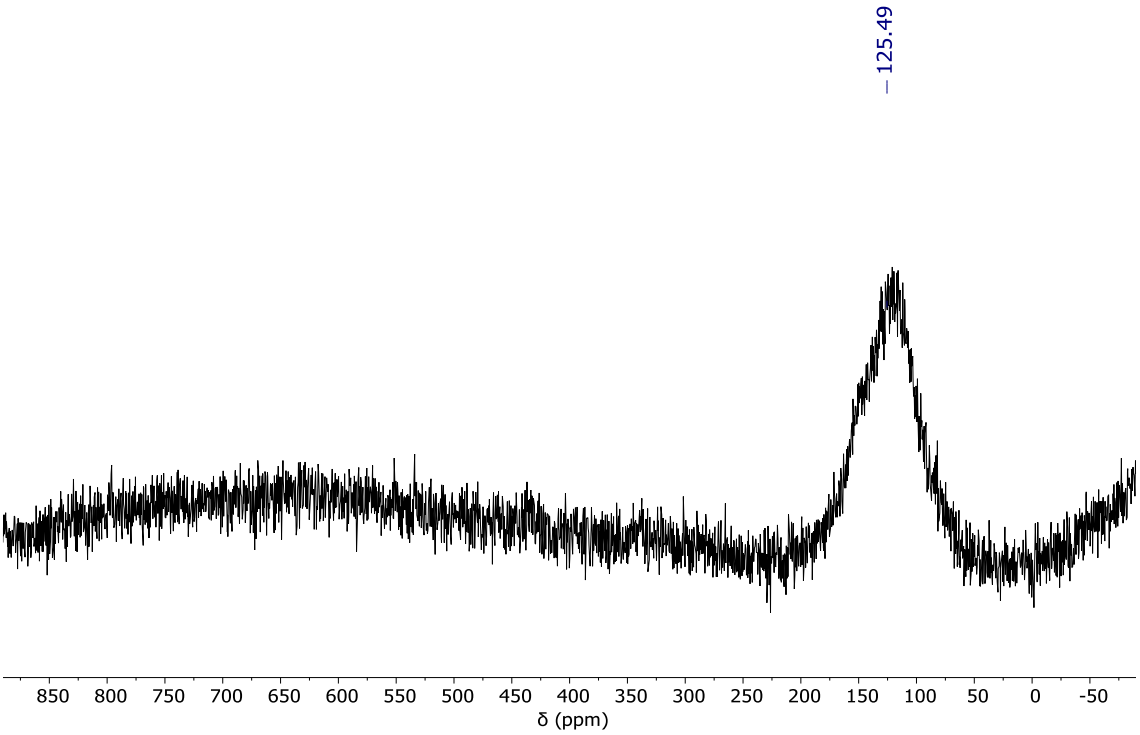


Figure A.56 $^{45}Sc\{^{1}H\}$ NMR spectrum (benzene-d_6, 121 MHz, 298 K) of $^{Me_2}SB(^{tBu_2}ArO,I^*)Sc(Cl)OPPh_3$ (**11**)

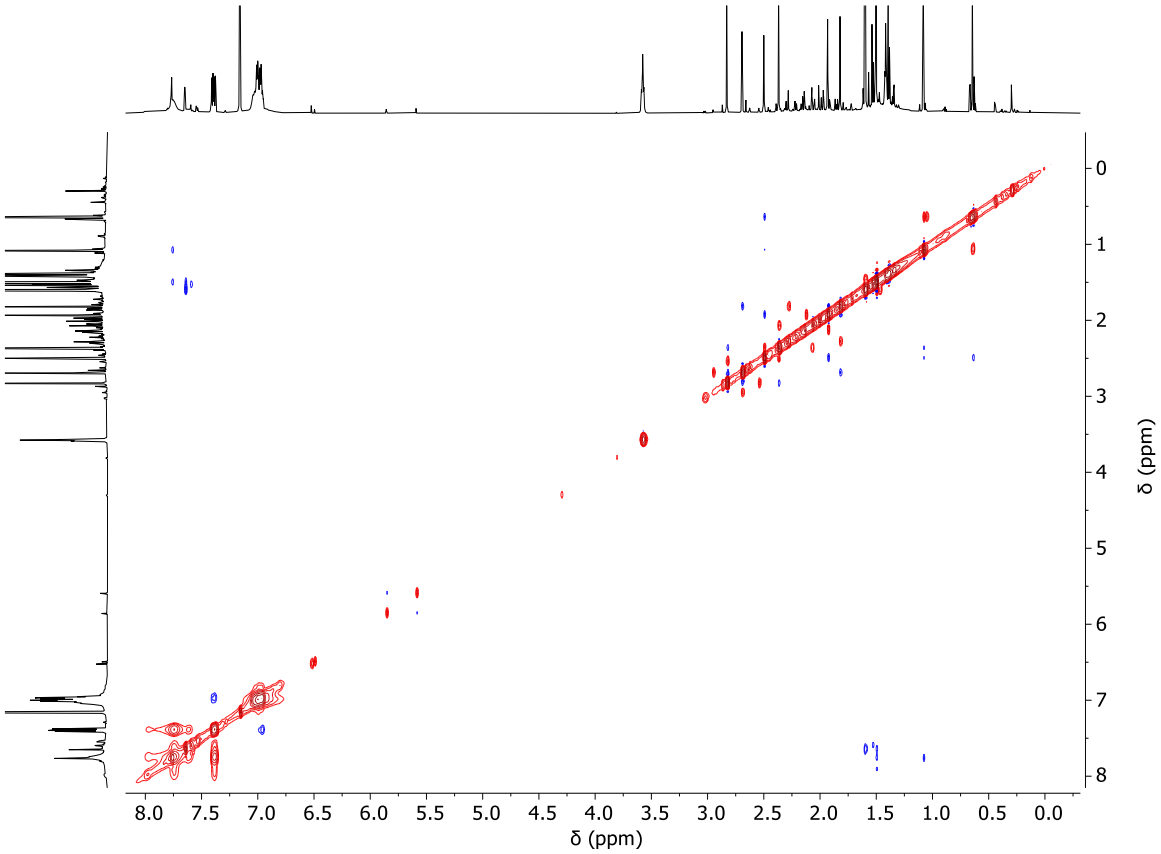


Figure A.57 ^{1}H-^{1}H NOESY spectrum (benzene-d_6, 600 MHz, 298 K) of ^{Me_2}SB($^{t Bu_2}$ArO,I*)Sc(Cl)OPPh$_3$ (**11**).

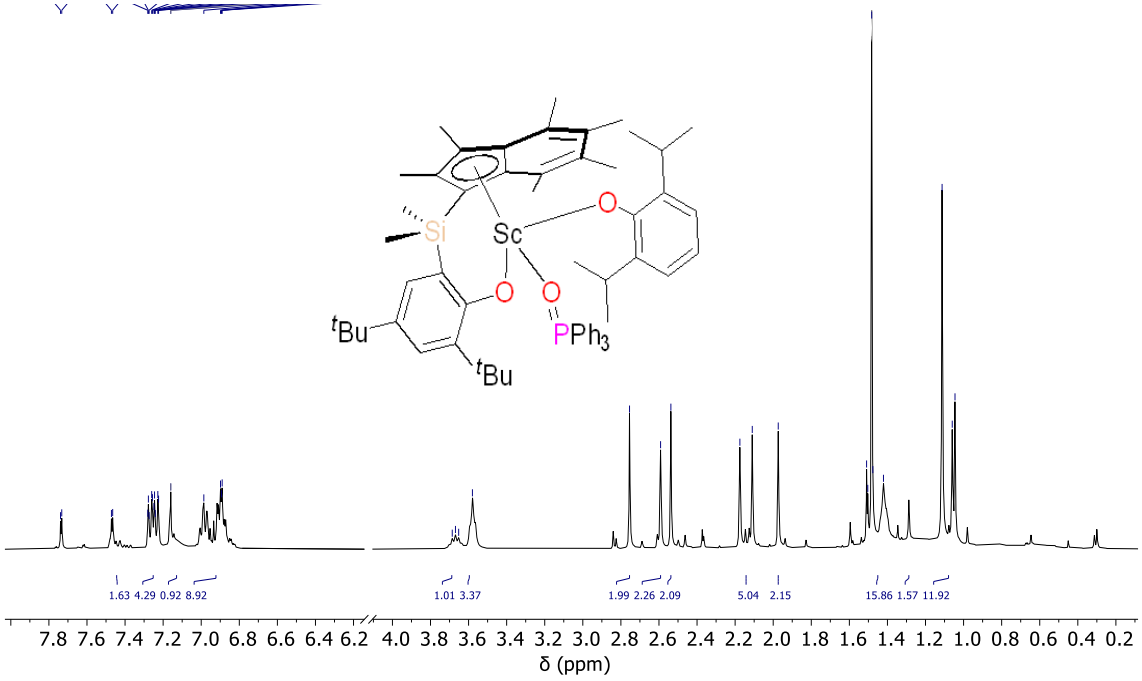


Figure A.58 ^{1}H NMR spectrum (benzene-d_6, 400 MHz, 298 K) of ^{Me_2}SB($^{t Bu_2}$ArO,I*)Sc(ODipp)OPPh$_3$ (**12**).

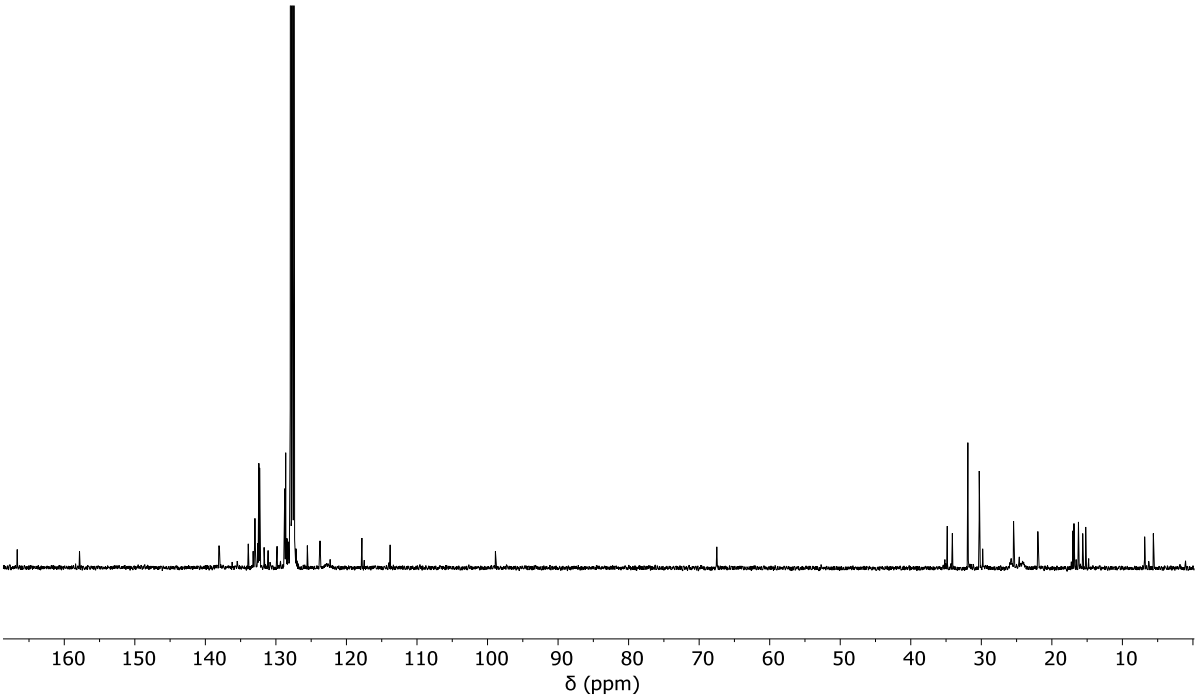


Figure A.59 $^{13}C\{^{1}H\}$ NMR spectrum (benzene-d_6, 101 MHz, 298 K) of $^{Me_2}SB(^{t Bu_2}ArO,I^*)Sc(ODipp)OPPh_3$ (**12**).

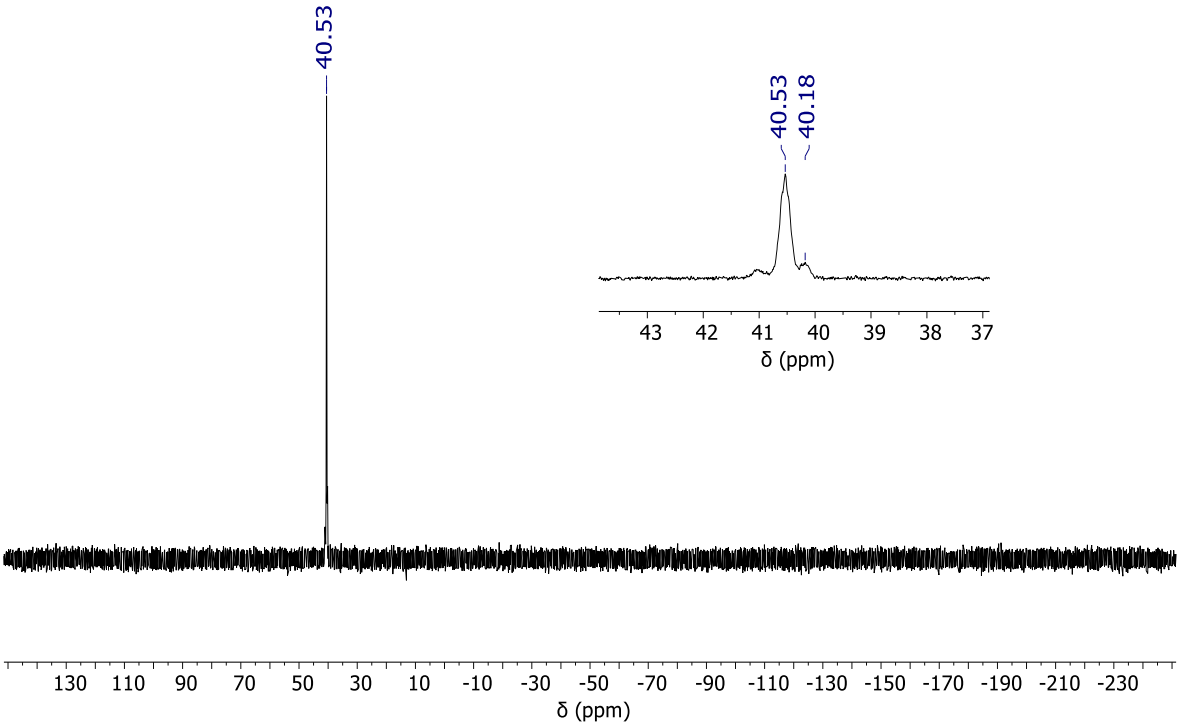


Figure A.60 $^{31}P\{^{1}H\}$ NMR spectrum (benzene-d_6, 162 MHz, 298 K) of $^{Me_2}SB(^{t Bu_2}ArO,I^*)Sc(ODipp)OPPh_3$ (**12**).

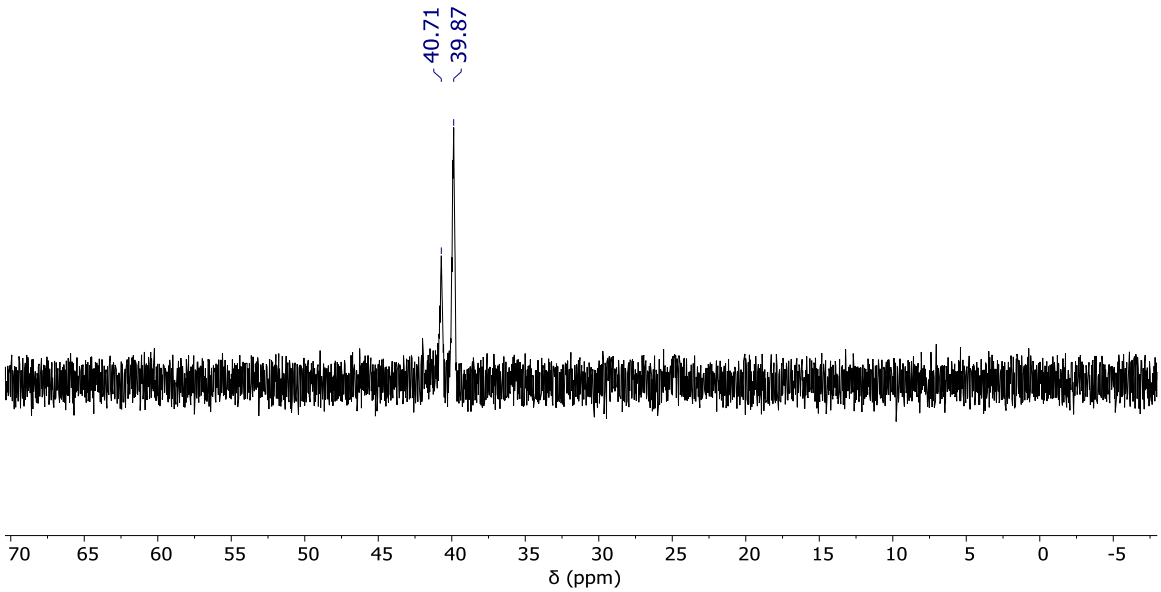


Figure A.61 $^{31}P\{^{1}H\}$ NMR spectrum (benzene-d_6, 162 MHz, 298 K) of $^{Me_2}SB(^{tBu_2}ArO,I^*)Sc(ODipp)OPPh_3$ (**12**).

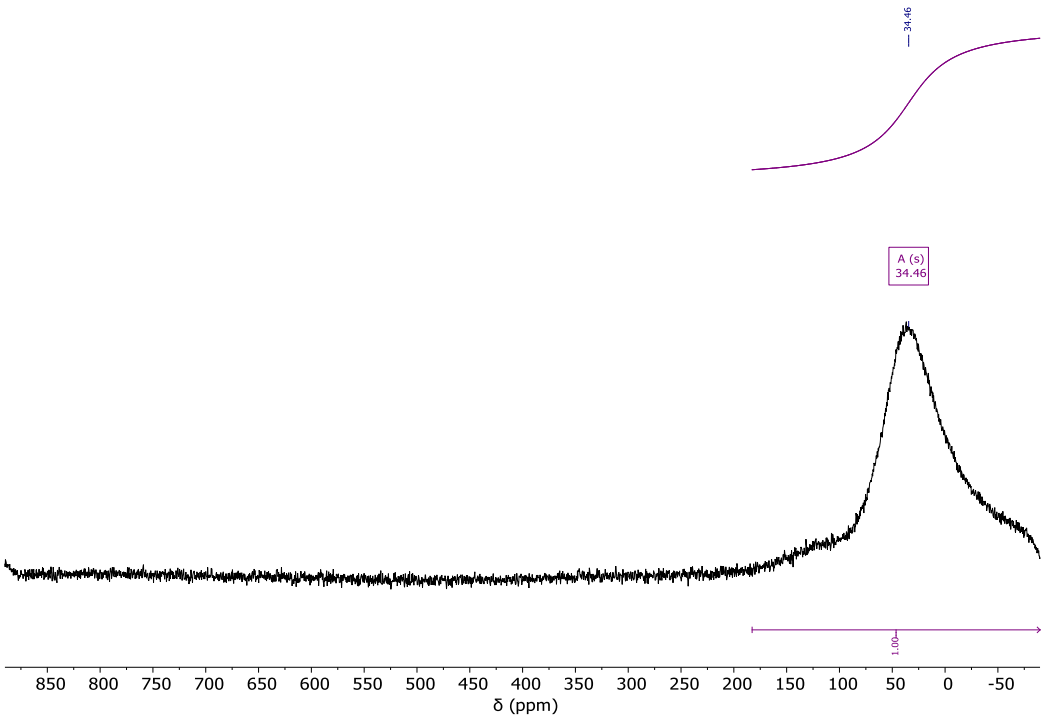


Figure A.62 $^{45}Sc\{^{1}H\}$ NMR spectrum (benzene-d_6, 121 MHz, 298 K) of $^{Me_2}SB(^{tBu_2}ArO,I^*)Sc(ODipp)OPPh_3$ (**12**)

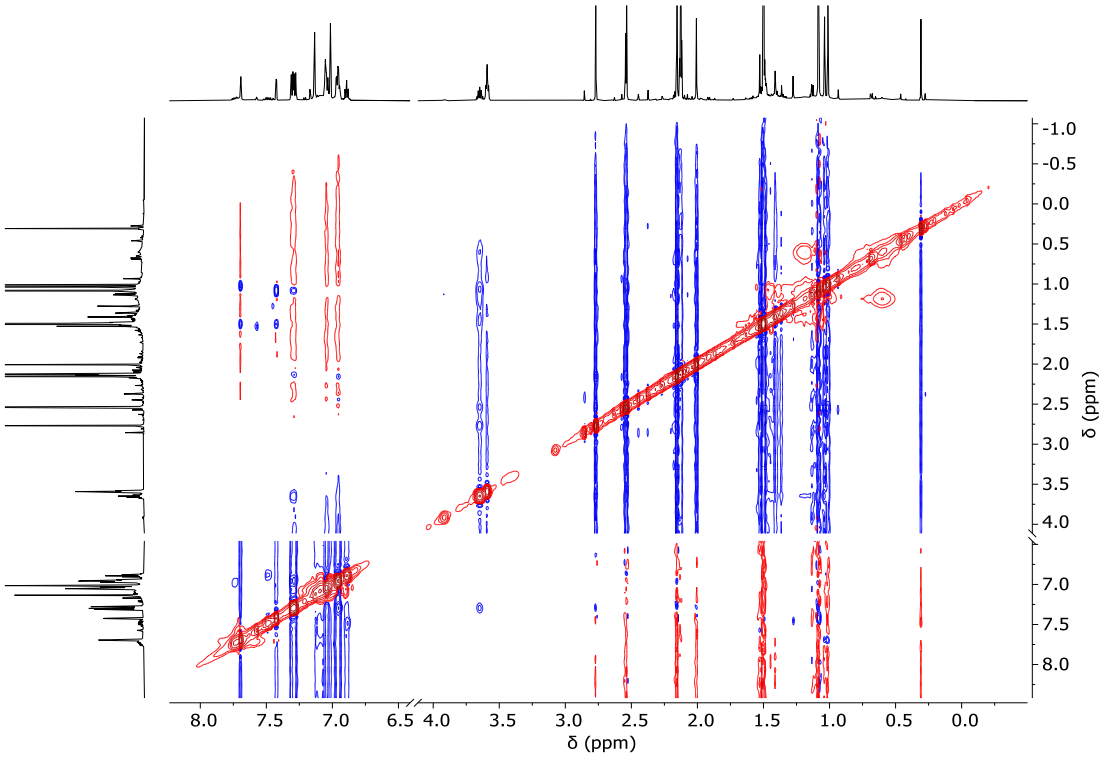


Figure A.63 ^{1}H-^{1}H NOESY spectrum (toluene-d_8, 600 MHz, 298 K) of ^{Me_2}SB($^{t Bu_2}$ArO,I*)Sc(ODipp)OPPh$_3$ (**12**)

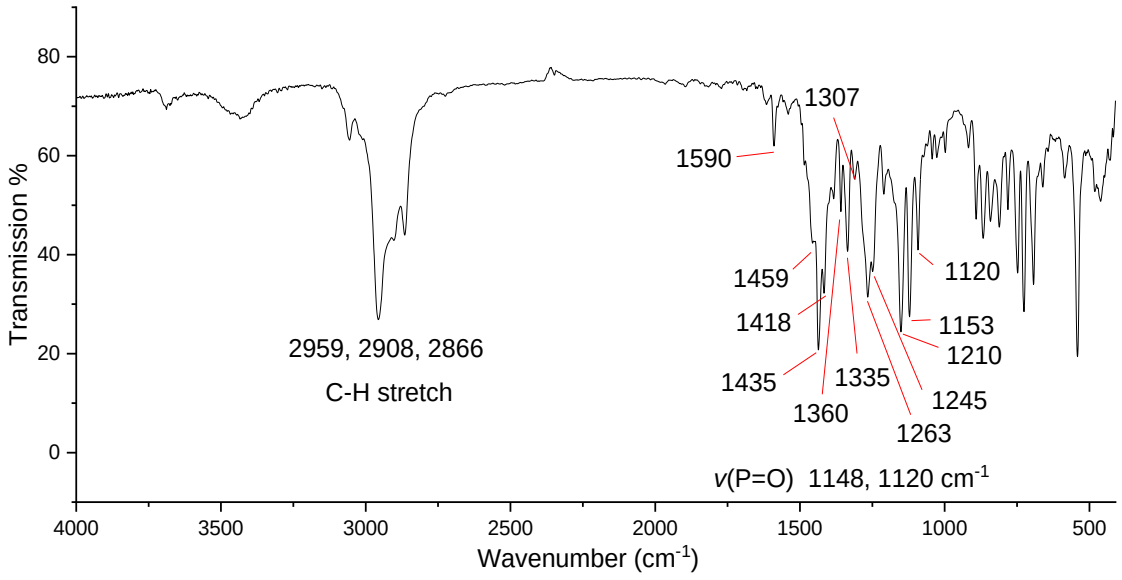


Figure A.64 IR of spectrum (KBr disk) ^{Me_2}SB($^{t Bu_2}$ArO,I*)Sc(ODipp)OPPh$_3$ (**12**) 4000–450 cm^{-1}

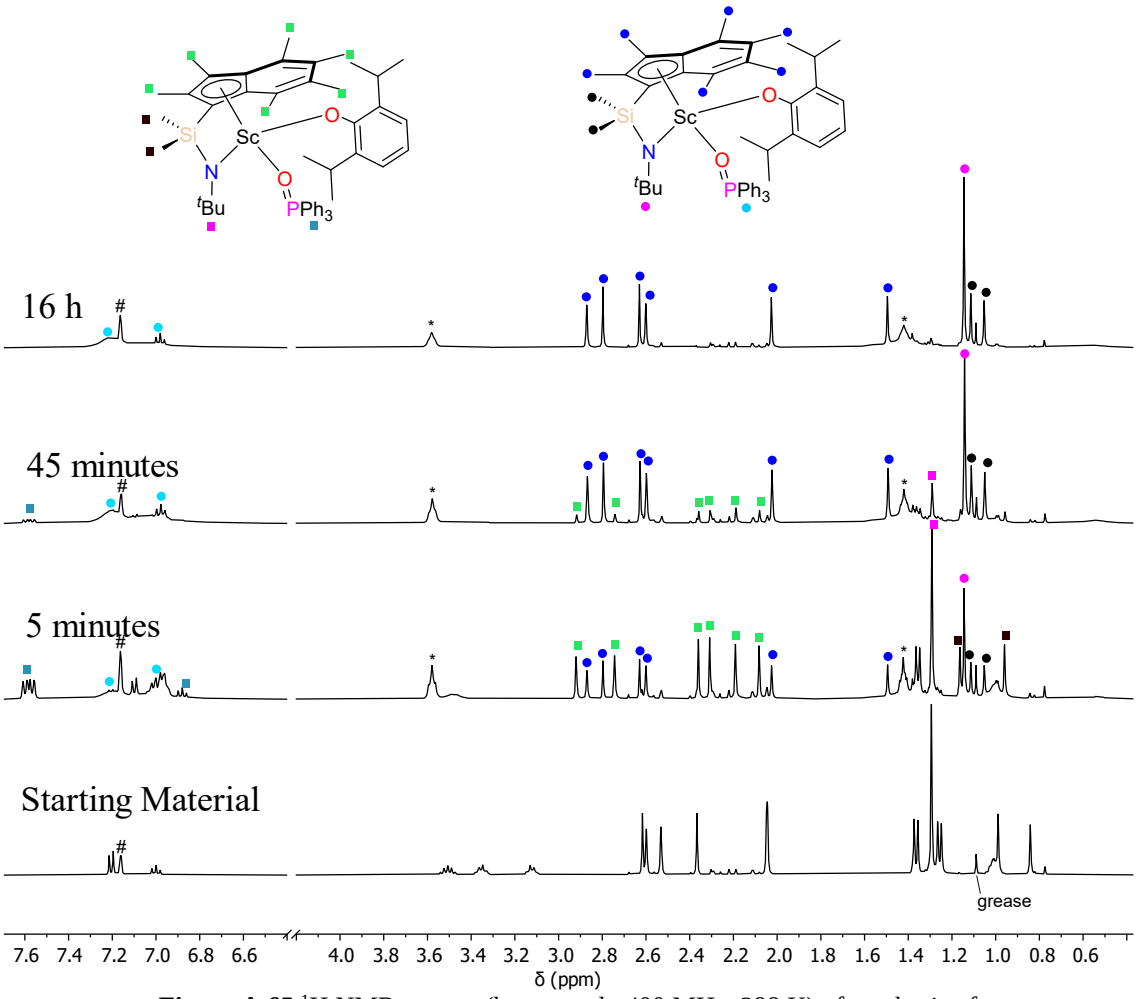


Figure A.65 ^{1}H NMR spectra (benzene-d_6, 400 MHz, 298 K) of synthesis of ^{Me_2}SB($^{t\text{Bu}}$N,I*)Sc(ODipp)OPPh$_3$ (**13**) from **7**. Shows the formation of two products at 5 minutes that fully convert to a single, thermodynamic product at room temperature over 16 hours. #protio solvent; *THF

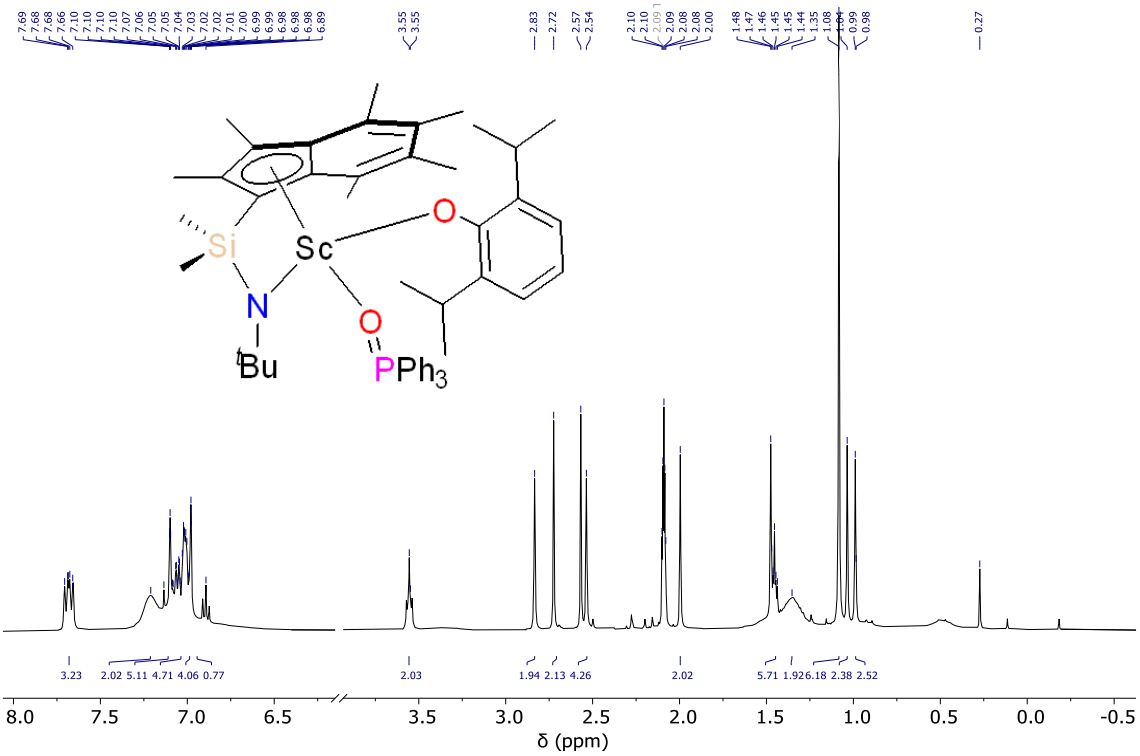


Figure A.66 ^{1}H NMR spectrum of ^{Me_2}SB($^{t Bu}$N,I*)Sc(ODipp).OPPh$_3$ (**13**) (toluene-d_8, 400 MHz, 298 K).

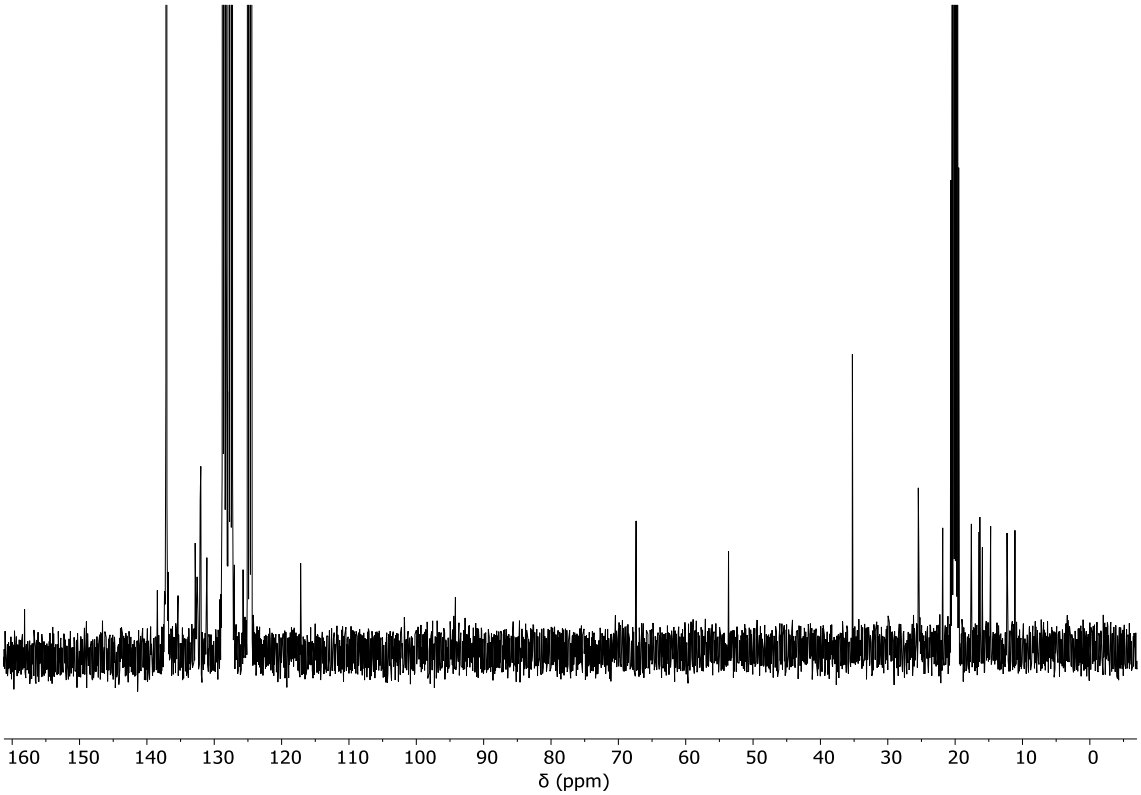


Figure A.67 ^{13}C{^{1}H} NMR spectrum (toluene-d_8, 126 MHz, 298 K) of ^{Me_2}SB($^{t Bu}$N,I*)Sc(ODipp)OPPh$_3$ (**13**).

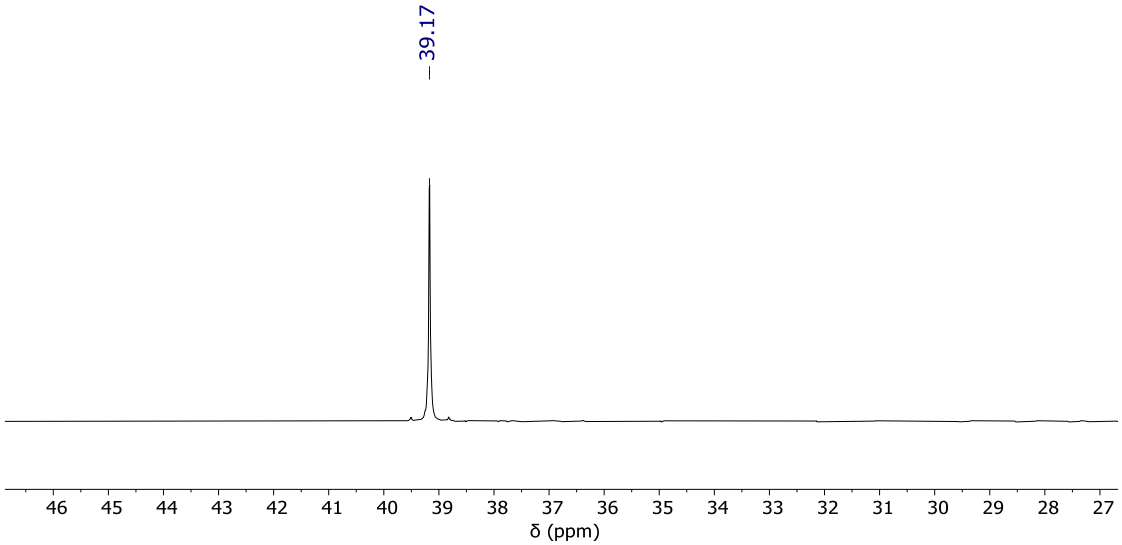


Figure A.68 $^{31}P\{^{1}H\}$ NMR spectrum (benzene-d_6, 121 MHz, 298 K) of $^{Me_2}SB(^{t Bu}N,I^*)Sc(ODipp)OPPh_3$ (**13)**.

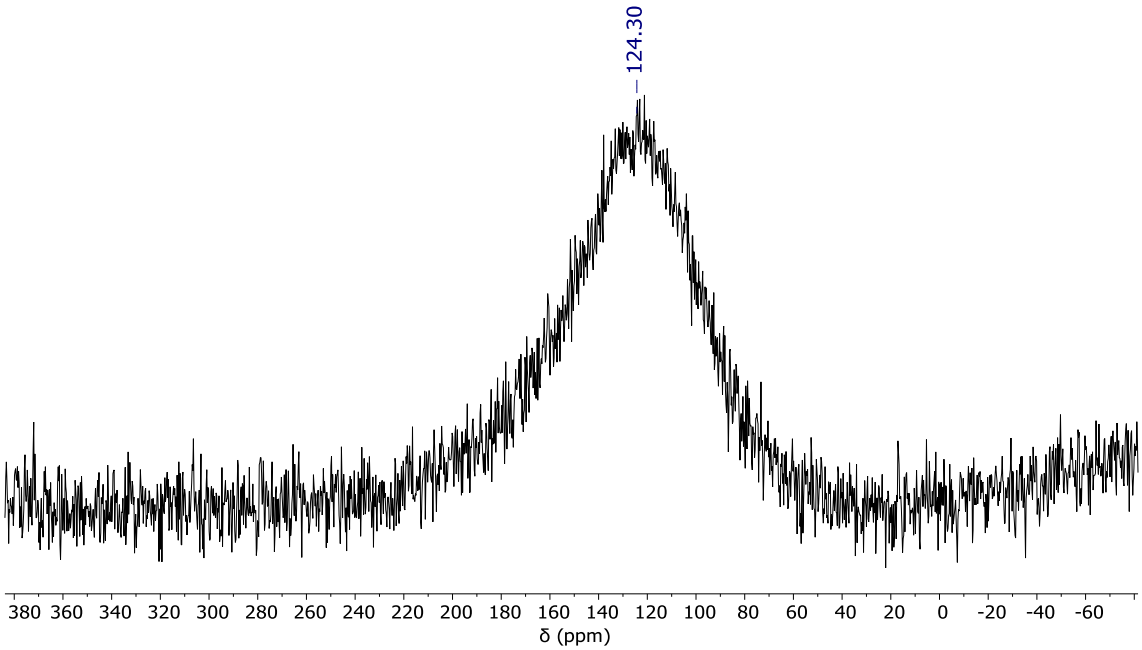


Figure A.69 $^{45}Sc\{^{1}H\}$ NMR spectrum (benzene-d_6, 121 MHz, 298 K) of $^{Me_2}SB(^{t Bu}N,I^*)Sc(ODipp).OPPh_3$ **13)**: δ 124.30 ppm.

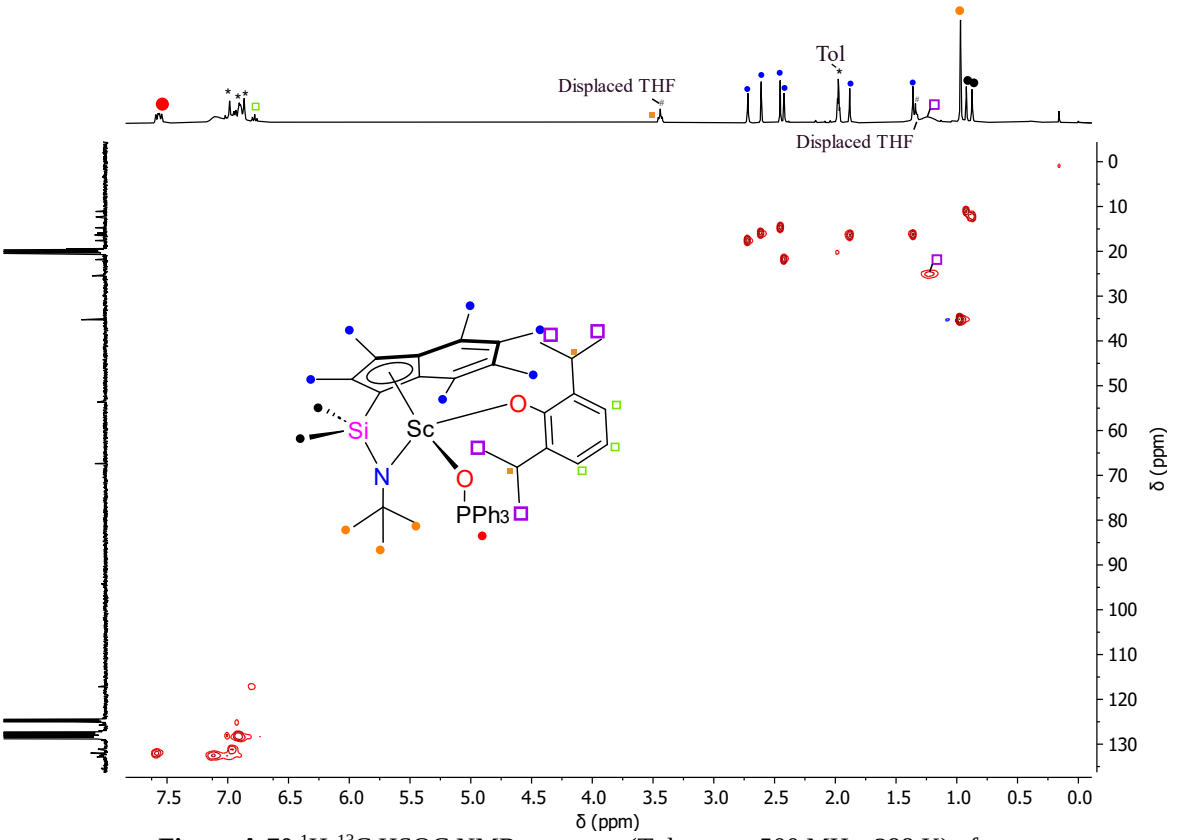


Figure A.70 ^{1}H-^{13}C HSQC NMR spectrum (Toluene-$_{d8,}$ 500 MHz, 298 K) of ^{Me_2}SB($^{t Bu}$N,I*)Sc(ODipp)OPPh (**13**).

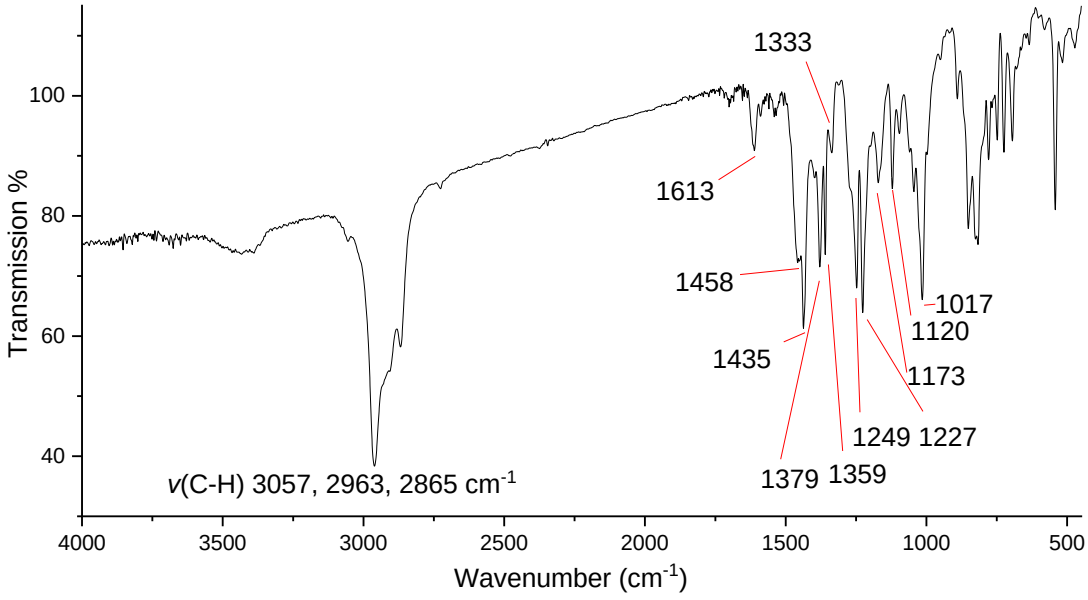


Figure A.71 IR of spectrum (KBr disk) ^{Me_2}SB($^{t Bu}$N,I*)Sc(ODipp)OPPh (**13**) 4000–450 cm^{-1}

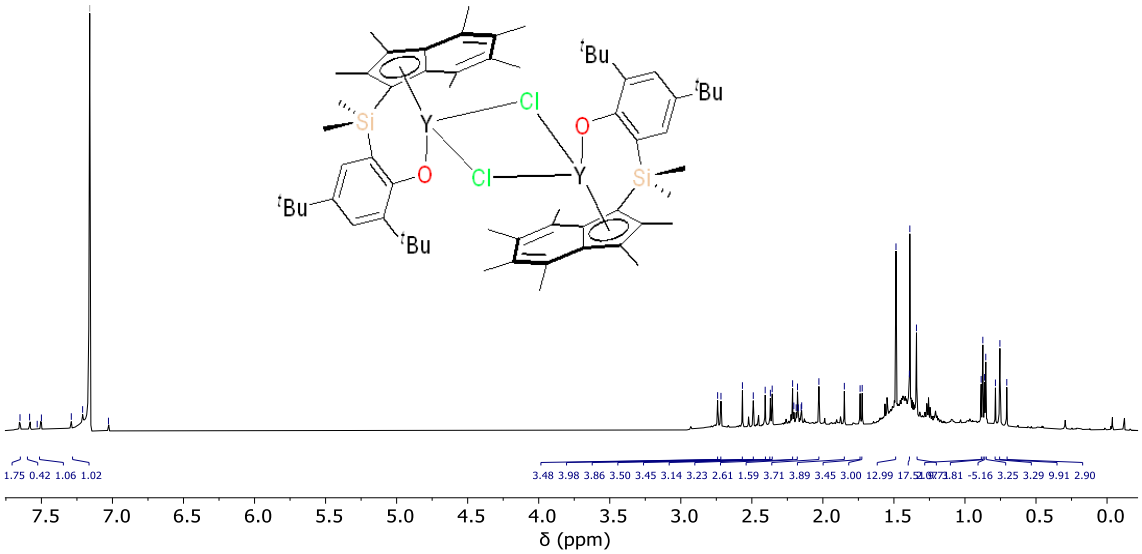


Figure A.72 ^{1}H NMR spectrum (benzene-d_6, 600 MHz, 298 K) of [^{Me_2}SB($^{t Bu_2}$ArO,I*)Y(Cl)]$_2$ **14**

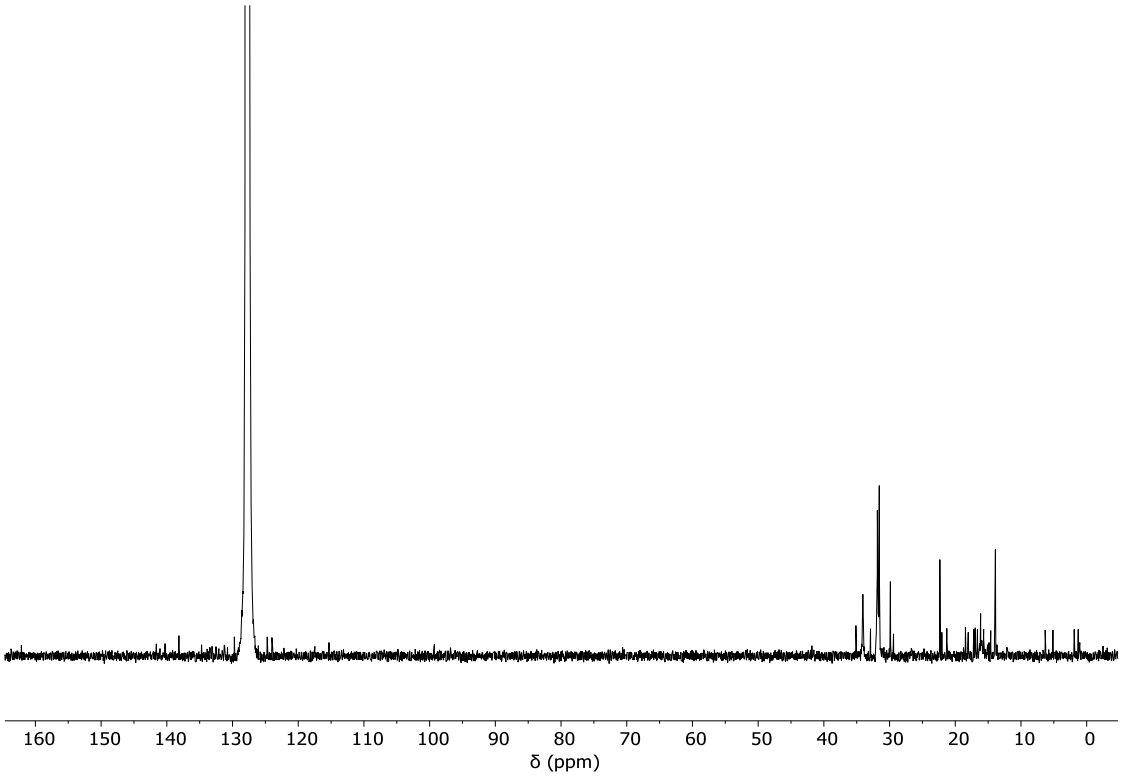


Figure A.73 ^{13}C{^{1}H} NMR spectrum (benzene-d_6, 151 MHz, 298 K).of [^{Me_2}SB($^{t Bu_2}$ArO,I*)Y(Cl)]$_2$ (**14**)

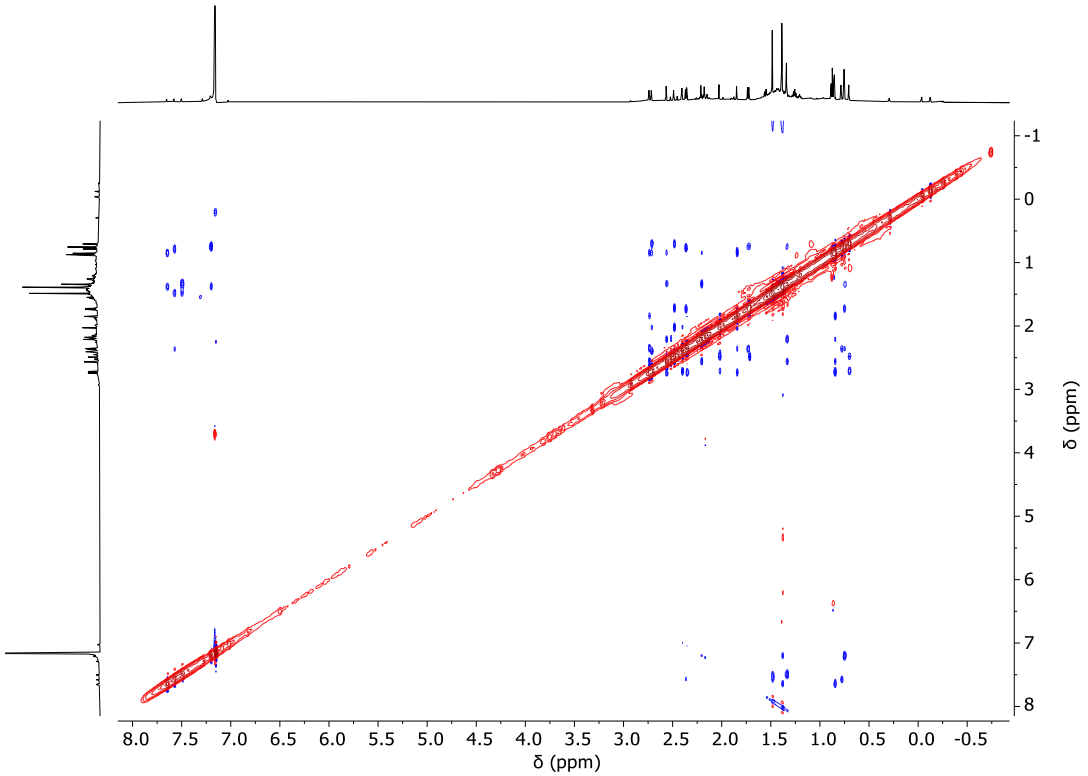


Figure A.74 ^{1}H-^{1}H NOESY spectrum of [^{Me_2}SB(^{tBu_2}ArO,I*)Y(Cl)]$_2$ (**14**) (benzene-d_6, 600 MHz, 298 K).

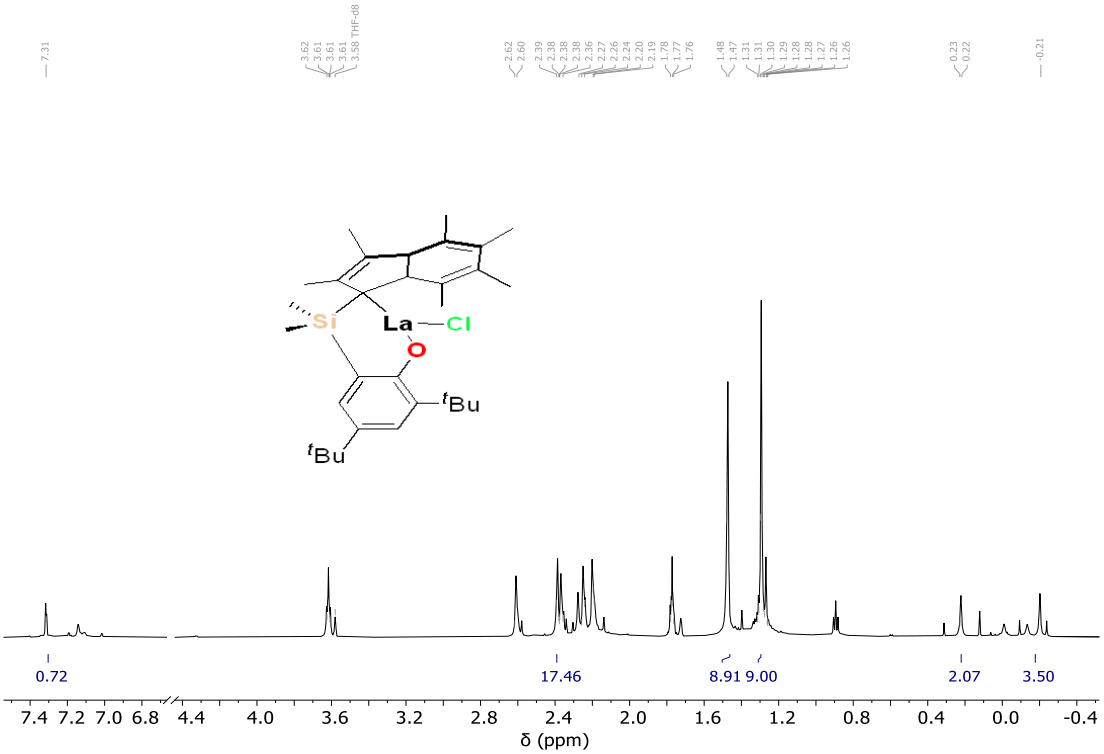


Figure A.75 ^{1}H NMR spectrum of ^{Me_2}SB(^{tBu_2}OAr,I*)La(Cl) (**15**) (THF-d_8, 600 MHz, 298 K).

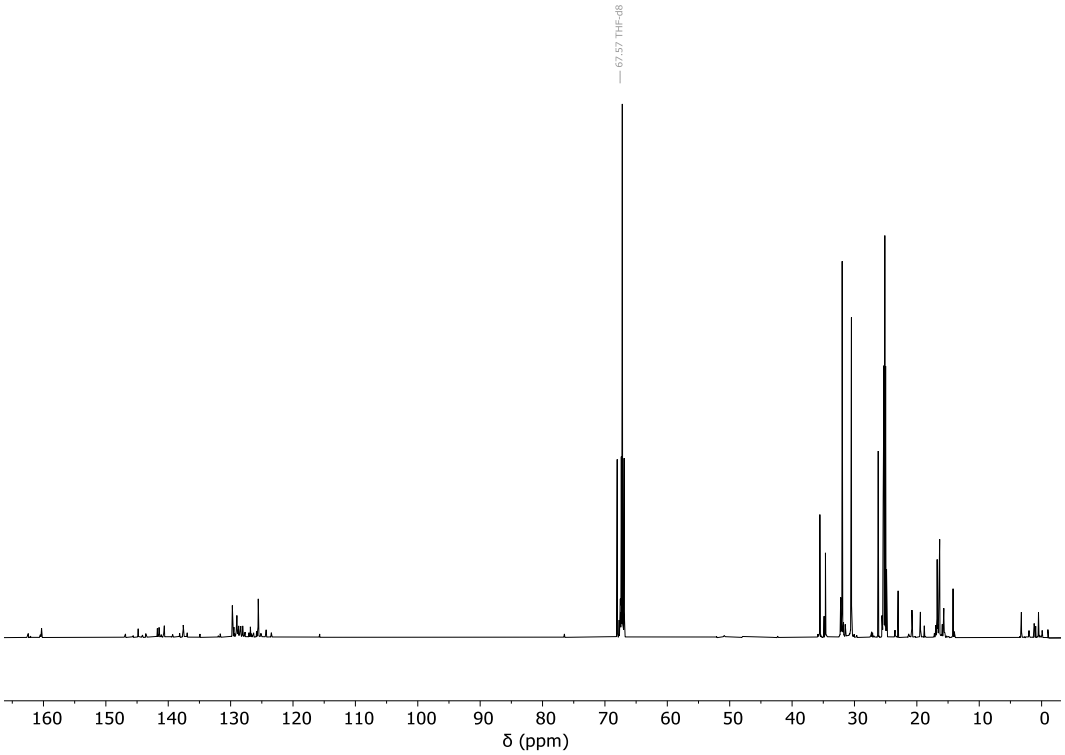


Figure A.76 $^{13}C\{^{1}H\}$ NMR spectrum (THF-d_8, 151 MHz, 298 K) of $^{Me_2}SB(^{tBu_2}OAr,I^*)La(Cl)$ (**15**).

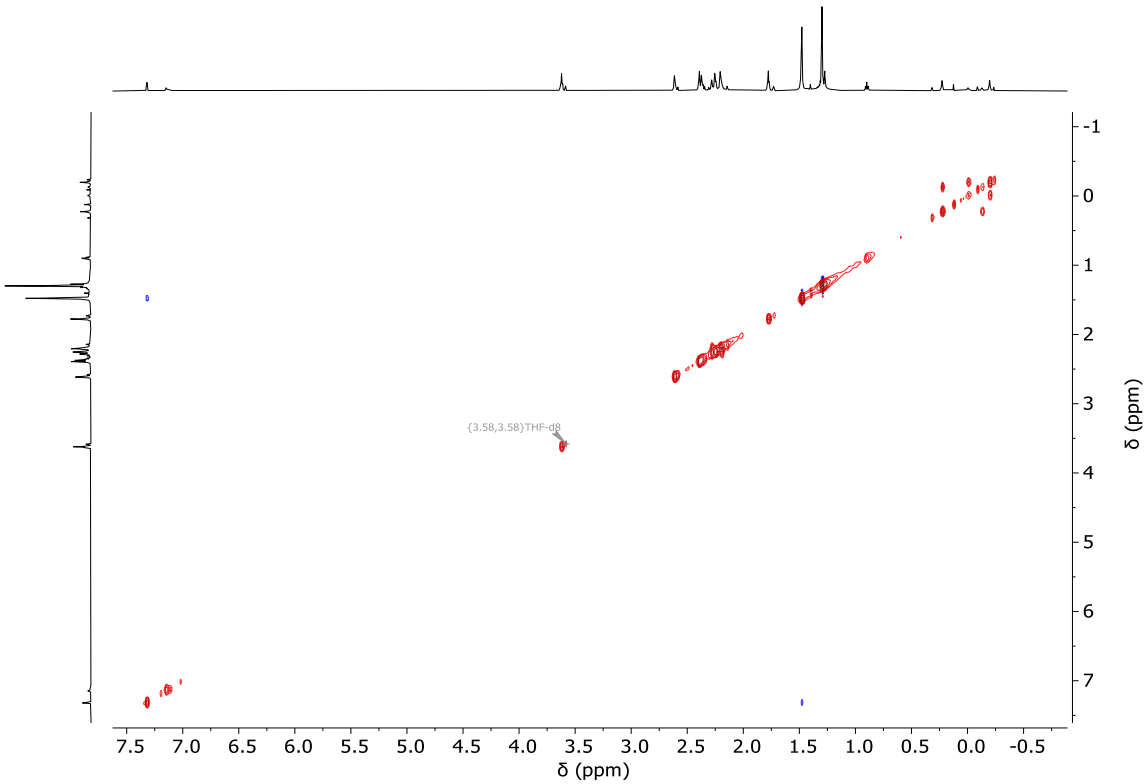


Figure A.77 ^{1}H-^{1}H NOESY spectrum (THF-d_8, 600 MHz, 298 K) of $^{Me_2}SB(^{tBu_2}OAr,I^*)La(Cl)$ (**15**).

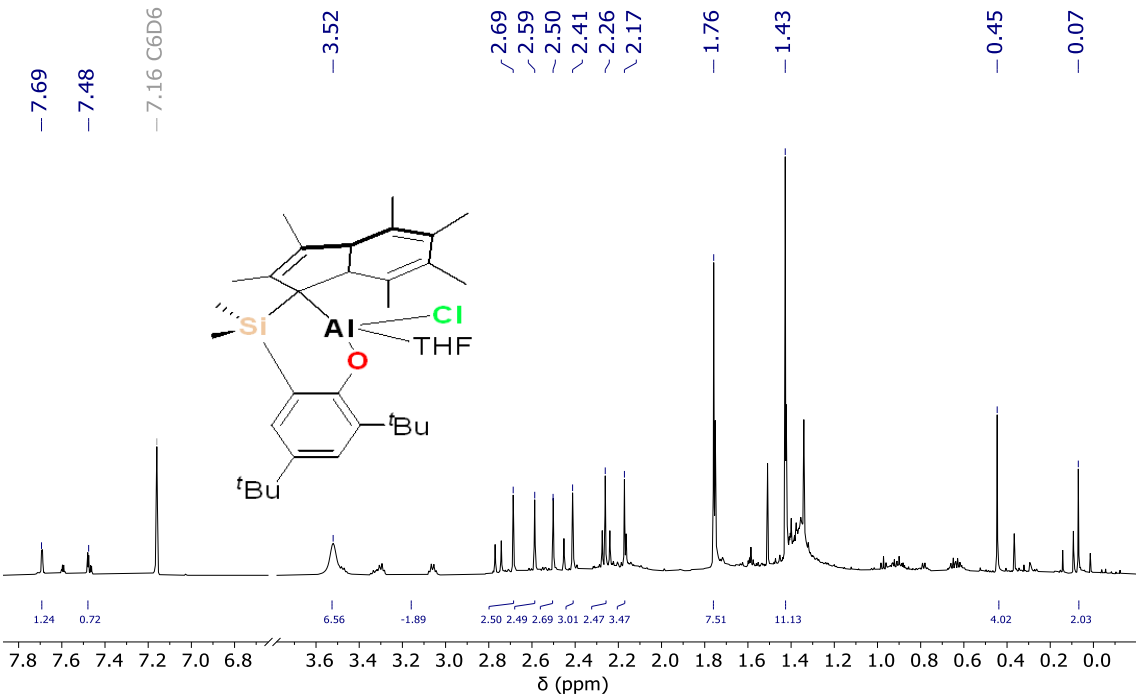


Figure A.78 ^{1}H NMR spectrum (benzene-d_6, 600 MHz, 298 K) of ^{Me_2}SB(^{tBu_2}ArO,I*)Al(Cl).THF (**16**).

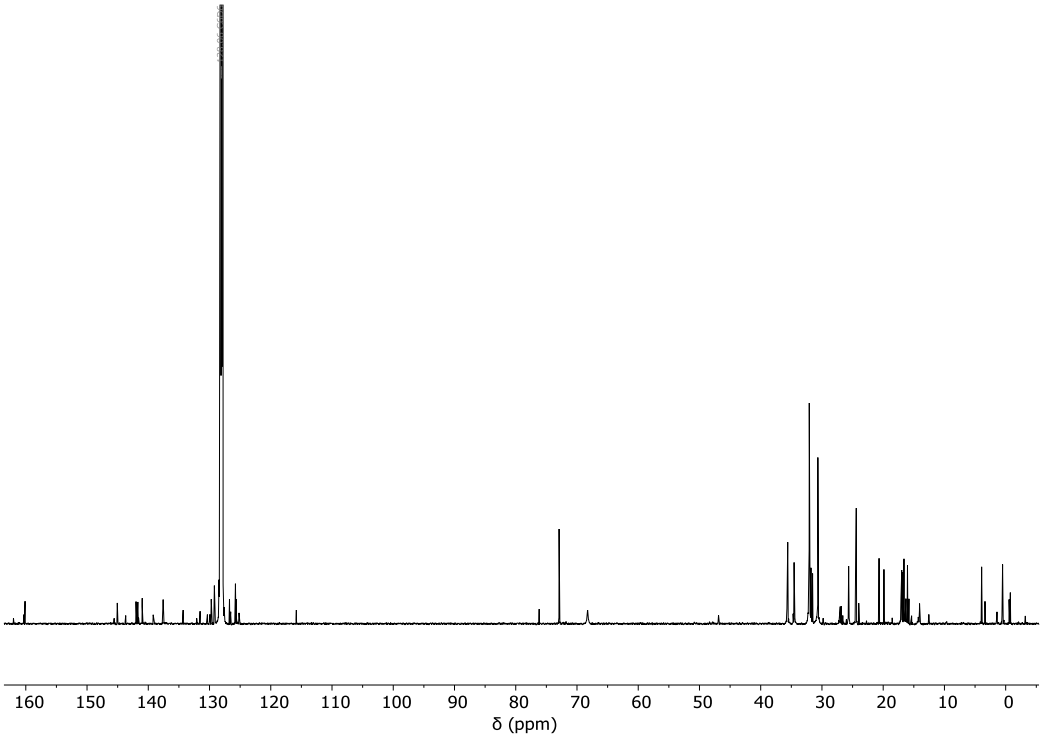


Figure A.79 ^{13}C{^{1}H} NMR spectrum (benzene-d_6, 151 MHz, 298 K) of ^{Me_2}SB(^{tBu_2}ArO,I*)Al(Cl).THF (**16**).

A.1.3. Computer Gibbs energy for 1, 2, 11, and 12

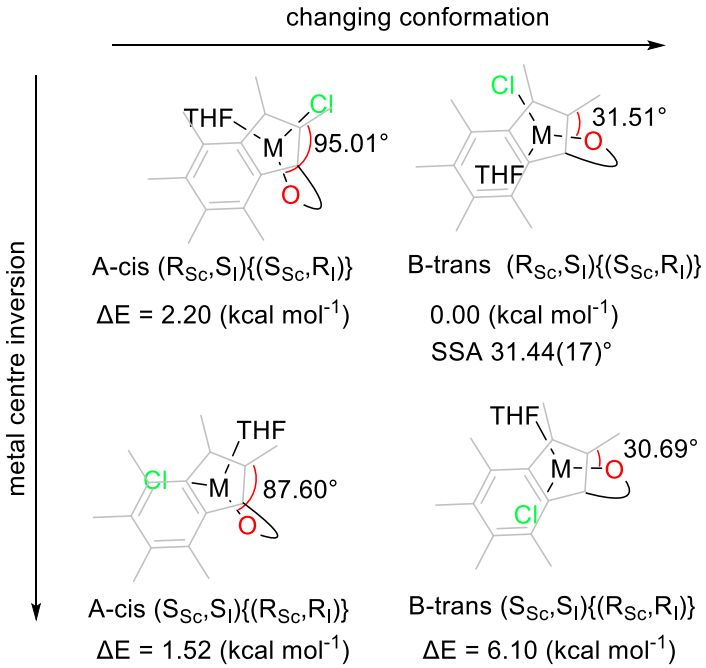


Figure A.80 Computed Gibbs energy profile for the 8 isomers **1**. The relative energies are computed using r^{2}SCAN-3c and presented as ΔG (kcal mol^{-1}) relative to the solid-state structure of **1** (B-trans R_{Sc},S_I). {} signifies enantiomer not shown. Dihedral angle ϕ TA′(M) shown in red.

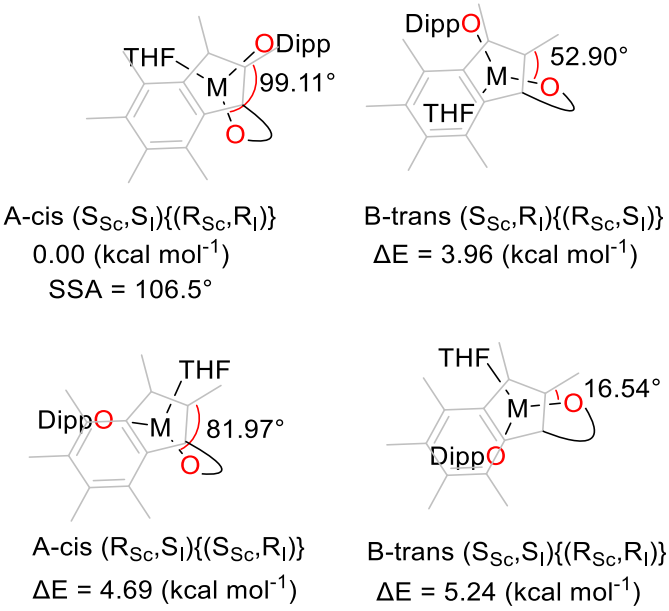


Figure A.81 Computed Gibbs energy profile for the 8 isomers **2**. The relative energies are computed using r^{2}SCAN-3c and presented as ΔG (kcal mol^{-1}) relative to the solid-state structure of **2** (A-cis S_{Sc},S_I). {} signifies enantiomer not shown. Dihedral angle ϕ TA′(M) shown in red.

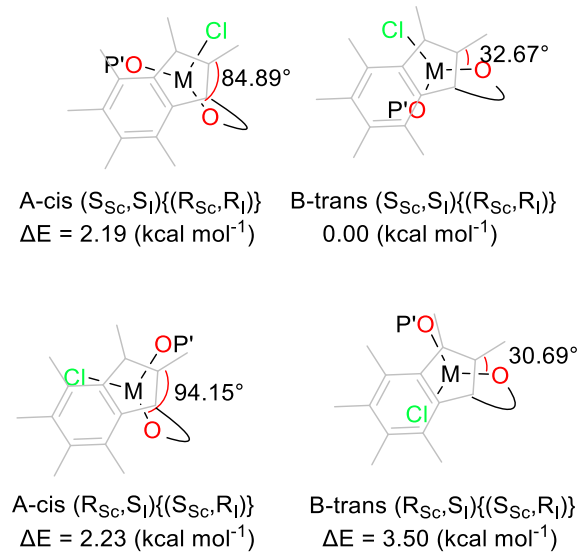


Figure A.82 Computed Gibbs energy profile for the 8 isomers of **11**. The relative energies are computed using r^{2}SCAN-3c and presented as ΔG (kcal mol^{-1}) relative to the lowest energy configuration **11** B-trans (S_{Sc},S_I). {} signifies enantiomer not shown. Dihedral angle ϕ TA′(M) shown in red.

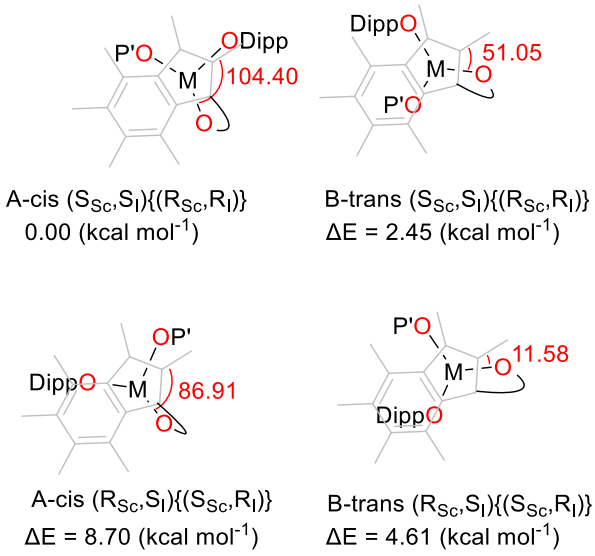


Figure A.83 Computed Gibbs energy profile for the 8 isomers of **12**. The relative energies are computed using r^{2}SCAN-3c and presented as ΔG (kcal mol^{-1}) relative to the lowest energy configuration of **12** (A cis S_{Sc},S_I). {} signifies enantiomer not shown. Dihedral angle ϕ TA′(M) shown in red.

A.2. Summary of unsuccessful chemistries

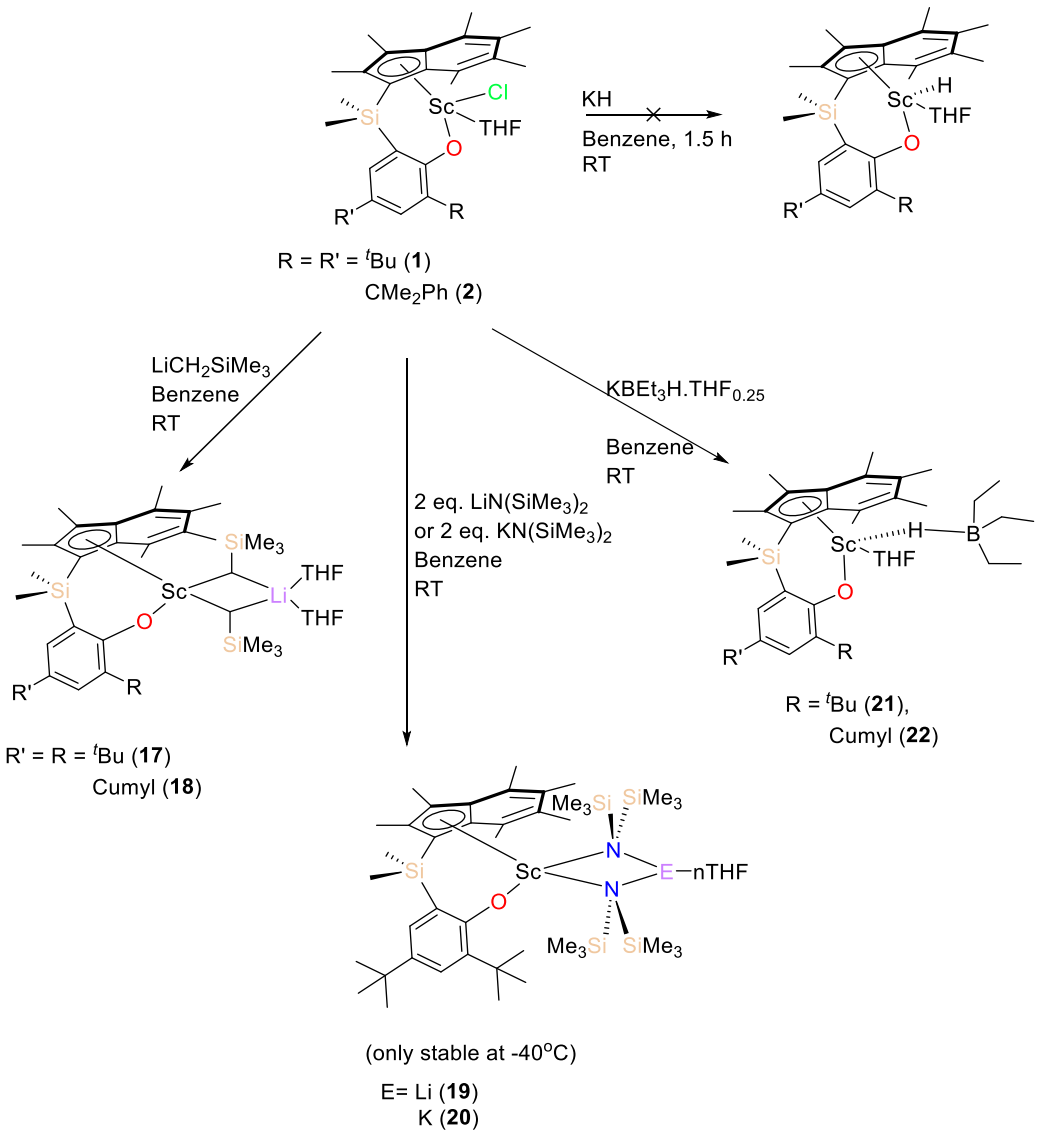
This section is devoted to reactions and synthesis of organometallic complexes that yielded results but were either (i) unstable and hence not fully characterised, (ii) contained significant impurities.

Part of this work has focused on finding alternative initiator groups for the scandium complexes discussed in this work. Previous work in the group has found titanium(IV) I* complexes react with 1 or 2 eq, of Li-alkyl (alkyl = CH_2SiMe_3) to give both single and double substituted complexes.[13] The analogous scandium complex ^{Me2}SB($^{tBu,\ tBu}$ArO,I*)ScCl.thf (**1b**) preferentially reacts with two molar equivalents of Li-alkyl to provide -*ate* complexe ^{Me2}SB($^{tBu,\ tBu}$ArO,I*)Sc(CH_2SiMe_3)$_2$Li·(thf)$_n$, according to NMR and consistent with the literature. It was suggested that the bulkier silazide ligand $(N(SiMe_3)_2)^-$ would favour formation of the monosubstituted product ^{Me2}SB($^{tBu,\ tBu}$ArO,I*)Sc($N(SiMe_3)_2$)·(thf).

The reaction was repeated with 2 equivalents of Li($N(SiMe_3)_2$ or Li($N(SiMe_3)_2$: 2 equiv. of LiHMDS or KHMDS was added to a J. Young's NMR tube containing 1 equiv. of **1** The reaction was monitored by ^{1}H NMR spectroscopy which indicated the clean formation of **1f** as the only PHENI*-containing product.

Such complexes were useful intermediates for further reactions. For example, metal alkyls have been employed as precursors to hydride complexes via further reaction with hydrogen or silanes. Two slightly different synthetic routes were used to target PHENI* supported trimethylsilyl-methyl scandium complexes. To [^{Me2}SB($^{tBu,\ tBu}$ArO,I*)ScCl·(thf)] 1-2 equivalents of LiCH_2SiMe_3 dissolved in C_6D_6 and an NMR of the crude reaction mixture was collected. Reacting with less than 2 eq. of LiCH_2SiMe_3 leads to partial conversion to the proposed product [^{Me2}SB($^{tBu,\ tBu}$ArO,I*)Sc(CH_2SiMe_3)$_2$Li(thf)$_2$]. The same product, deduced by NMR was obtained by reaction of the PHENI* dilithium salt with the homoleptic scandium tris-alkyl complex [Sc(CH_2SiMe_3)$_3$·(thf)$_2$]. In this case, both reactants were dissolved in toluene at 0℃ then

the scandium alkyl was added dropwise over 15 mins. The mixture was allowed to warm to RT overnight then filtered, and solvents removed *in vacuo.*



Scheme A.1 Synthesis of **17**–**22** from **1** and **2.**

A.2.1. NMR spectra

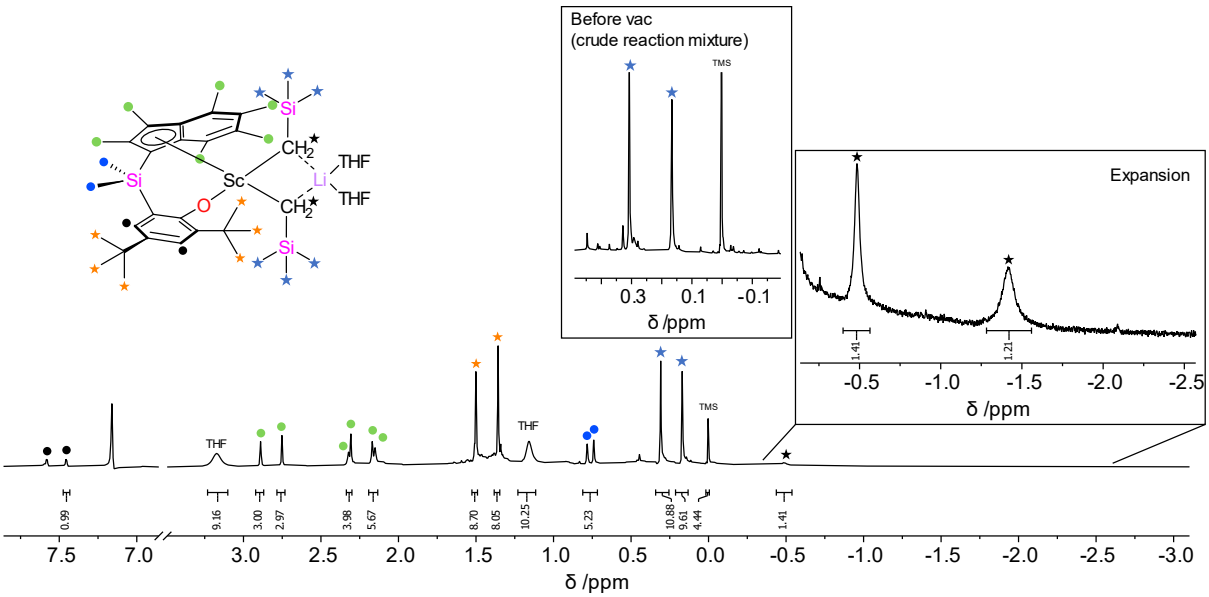


Figure A.84 ^{1}H NMR spectrum (benzne-d6, 400 Mhz, 298 K) of **17.** Expansion shows broad singlets in the negative shift. TMS is shown to be present at 0.00 ppm and can be removed partially under vacuum.

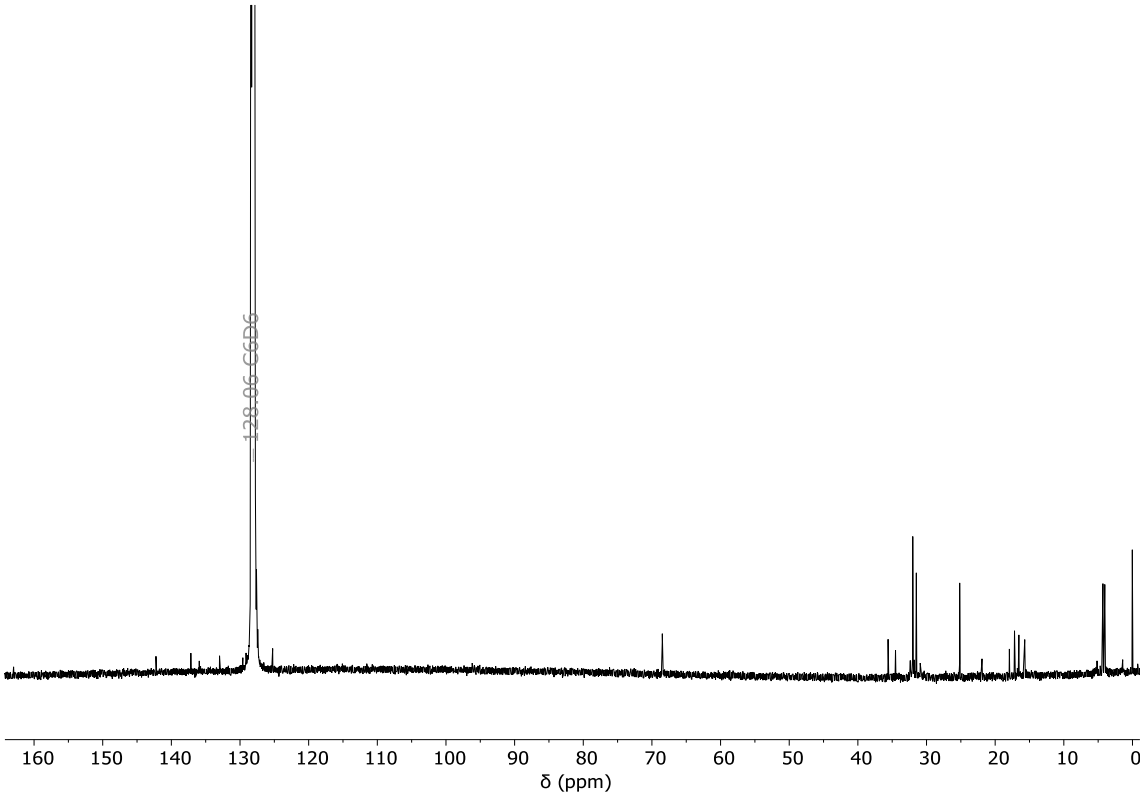


Figure A.85 ^{13}C{^{1}H} NMR spectrum (benzene-d_6, 151 MHz, 298 K) of ^{Me_2}SB($^{t Bu_2}$ArO,I*)Sc(CH_2($SiMe_3$))$_2$-μ^2Li.THF (**17**)

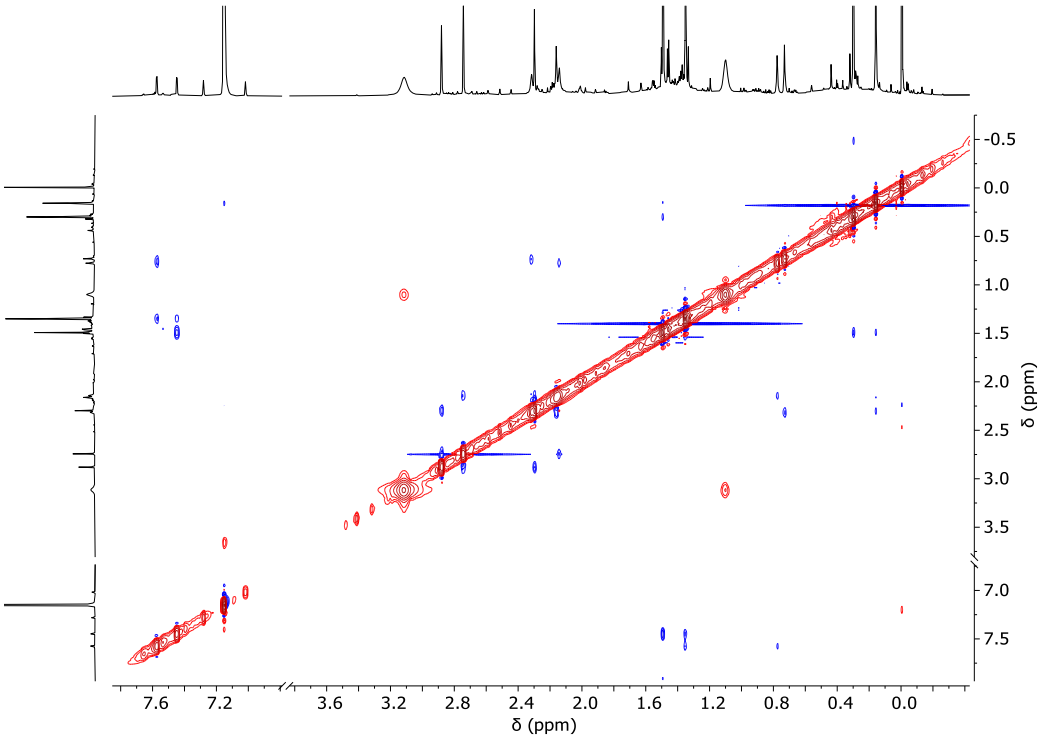


Figure A.86 ^{1}H-^{1}H NOESY spectrum (600 MHz, benzene-d_6, 298 K) of ^{Me_2}SB($^{t Bu_2}$ArO,I*)Sc(CH$_2$(SiMe$_3$))$_2$-μ^{2}Li.THF (**17**)

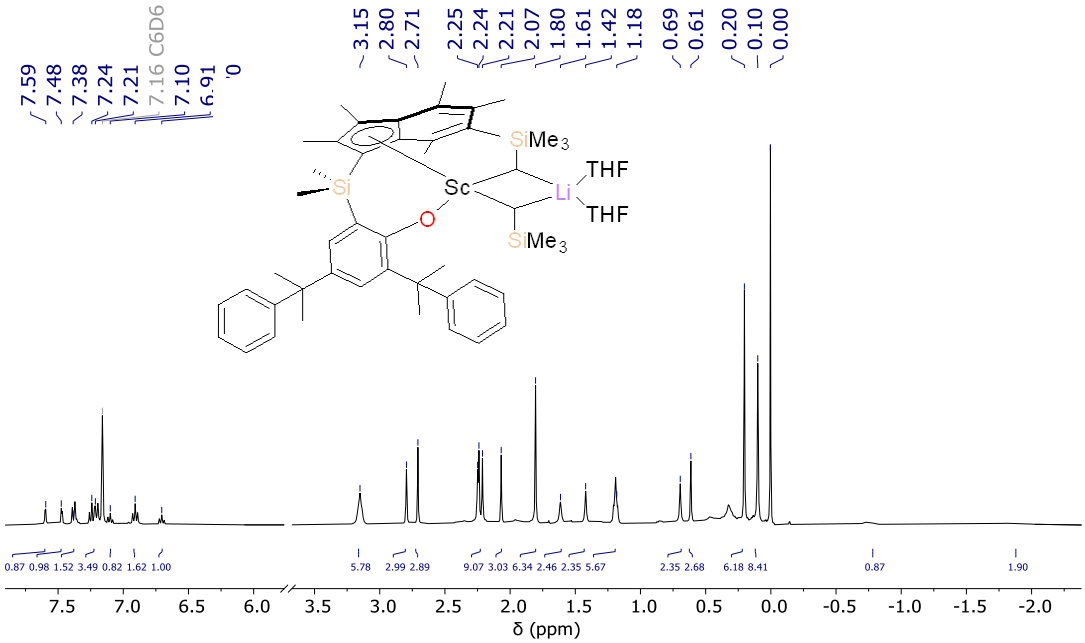


Figure A.87 ^{1}H NMR spectrum (benzene-d_6, 600 MHz, 298 K) of ^{Me_2}SB(^{Cumyl_2}ArO,I*)Sc(CH$_2$(SiMe$_3$))$_2$-μ^{2}Li.THF (**18**).

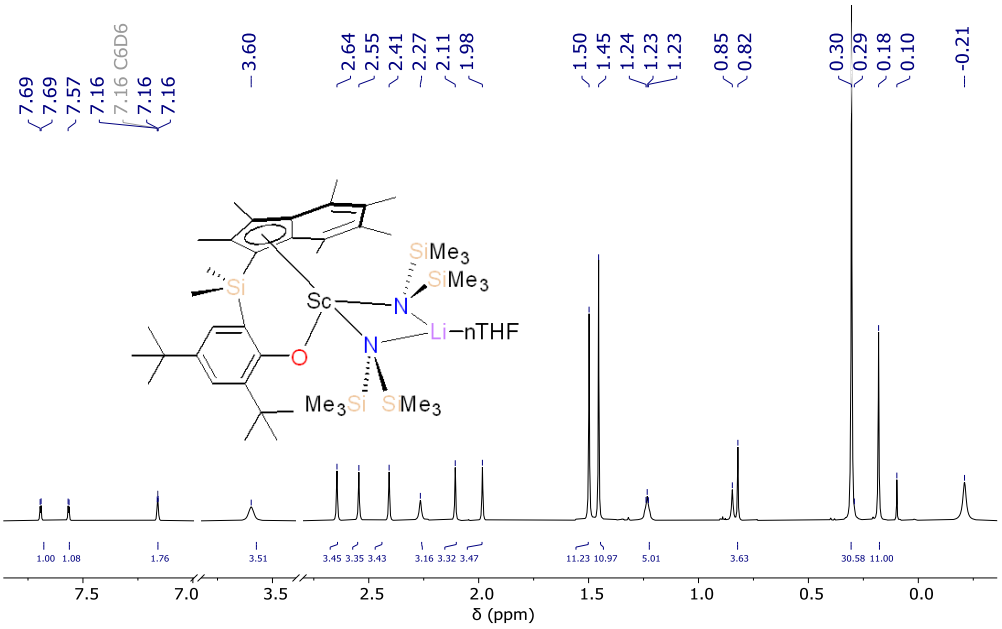


Figure A.88 ^{1}H NMR spectrum (benzene-d_6, 600 MHz, 298 K) of ^{Me2}SB(^{tBu2}ArO,I*)Sc(N(SiMe$_3$)$_2$)$_2$-μ^{2}Li.THF (**19**).

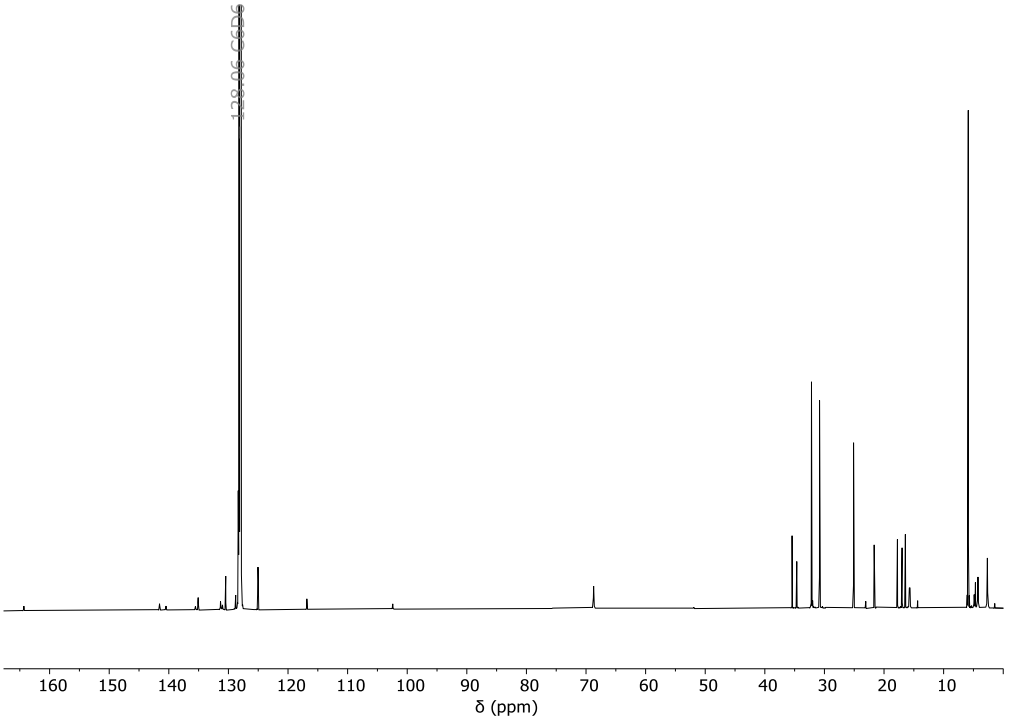


Figure A.89 ^{13}C{^{1}H} NMR spectrum (benzene-d_6, 151 MHz, 298 K) of ^{Me2}SB(^{tBu2}ArO,I*)Sc(N(SiMe$_3$)$_2$)$_2$-μ^{2}Li.THF (**19**).

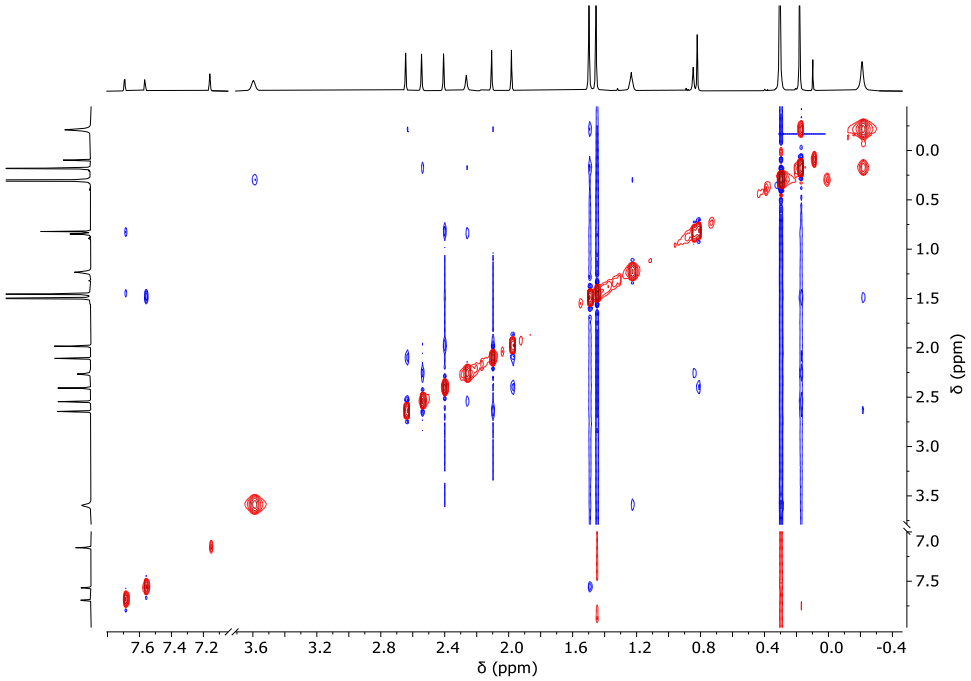


Figure A.90 ^{1}H-^{1}H NOESY spectrum (600 MHz, benzene-d_6, 298 K) of ^{Me_2}SB($^{t Bu_2}$ArO,I*)Sc(N(SiMe$_3$)$_2$)$_2$-μ^{2}Li.THF (**19**).

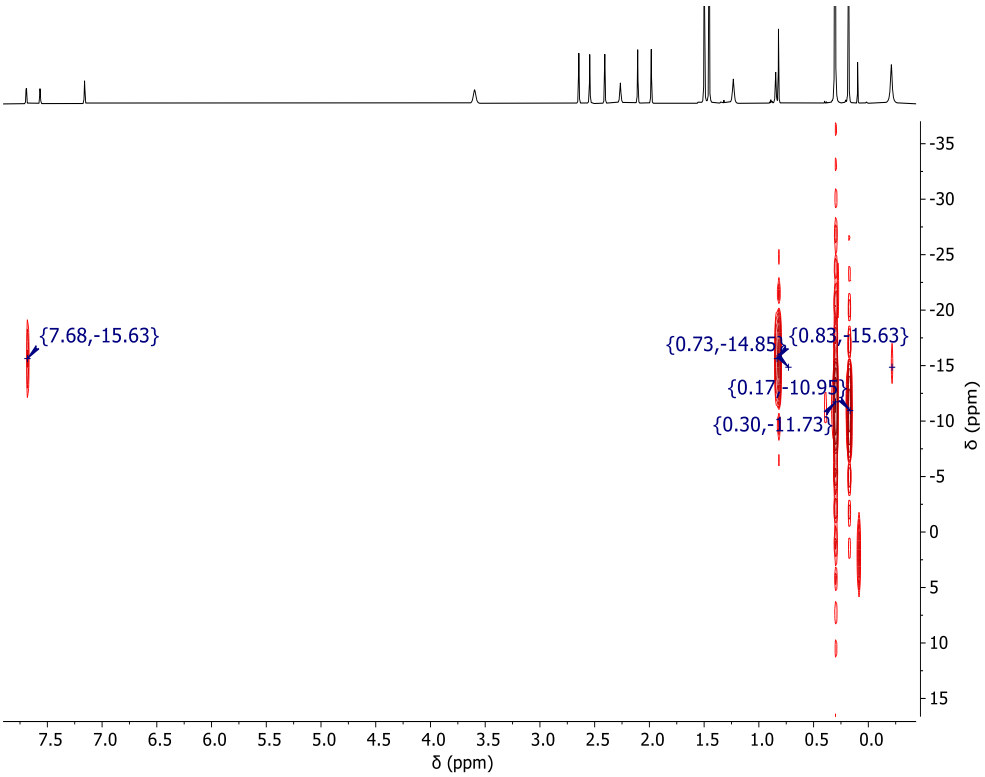


Figure A.91 ^{29}Si{^{1}H} HMBC 2D NMR spectrum (benzene-d_6, 500 MHz, 298 K) ^{Me_2}SB($^{t Bu_2}$ArO,I*)Sc(N(SiMe$_3$)$_2$)$_2$-μ^{2}Li.THF (**19**).

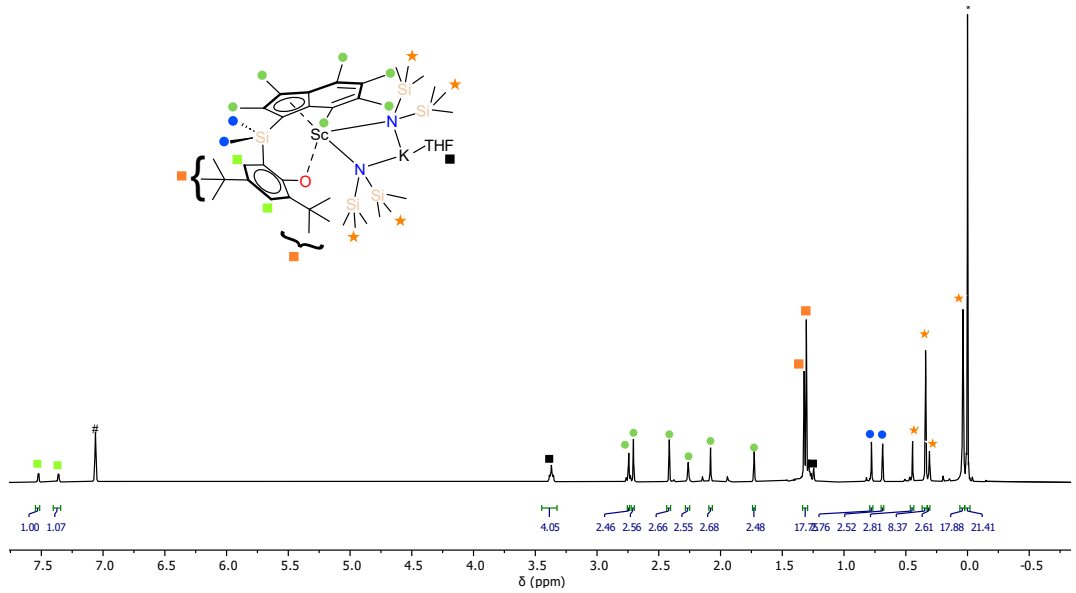


Figure A.92 ^{1}H NMR spectrum (C_6D_6, 400 MHz, 298 K) of ^{Me_2}SB(^{tBu_2}ArO,I*)Sc(N(SiMe$_3$)$_2$)$_2$.K (**20**) *denotes residual silyl impurity and * denotes residual protio solvent.

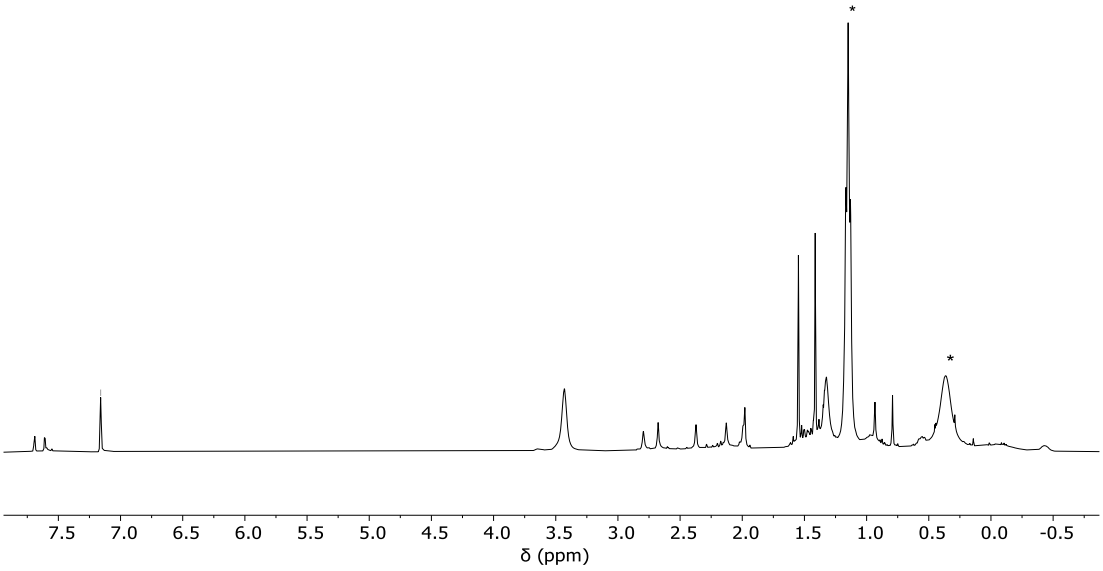


Figure A.93 ^{1}H NMR spectrum (benzene-d_6, 400 MHz, 298 K) of ^{Me_2}SB(^{tBu_2}ArO,I*)ScH(BEt$_3$)THF (**21**).* indicated KB(Et$_3$)H excess.

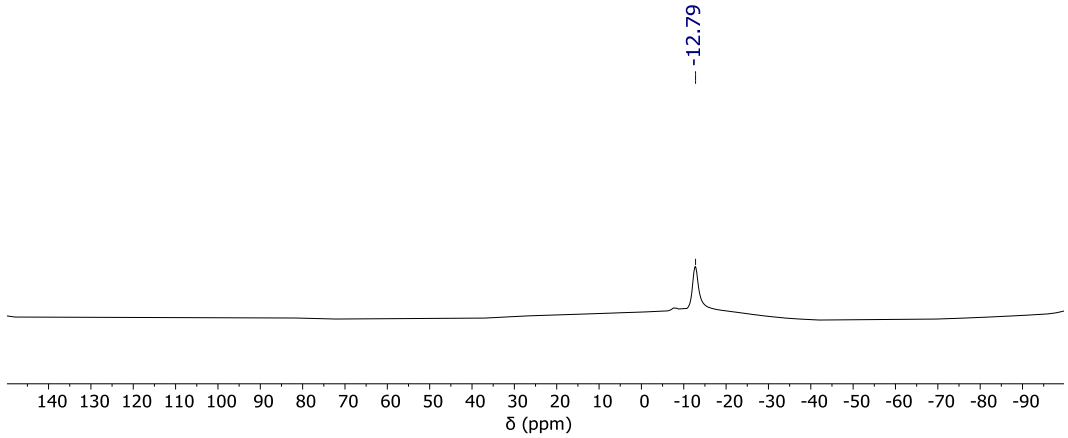


Figure A.94 $^{11}B\{^{1}H\}$ NMR spectra (benzene-d_6, 128.4 MHz, 298 K) [^{Me_2}SB(^{tBu_2}ArO,I*)ScH(BEt_3)·(thf)] (**21**).

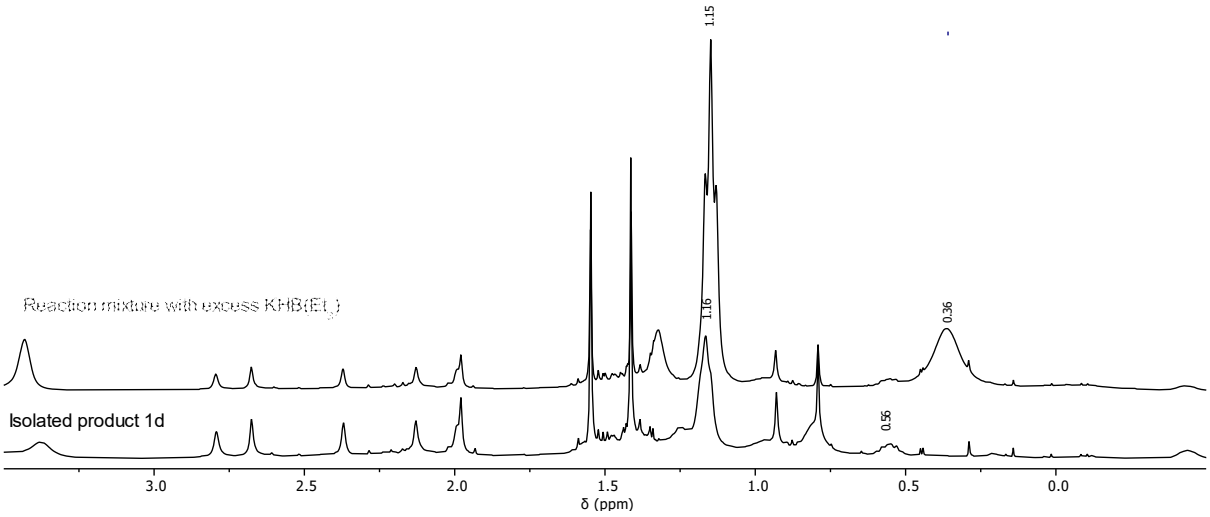


Figure A.95 ^{1}H NMR spectrum (C_6D_6, 400 MHz, 298 K) of **21.** Top; shows reaction mixture with excess $KHB(Et_3)$. Bottom; shows isolated product with peaks at δ 1.16 and 0.56 ppm corresponding to Sc-(μ-H)-BC**H**$_2$CH$_3$ and Sc-(μ-H)-BCH$_2$C**H**$_3$ environments respectively.

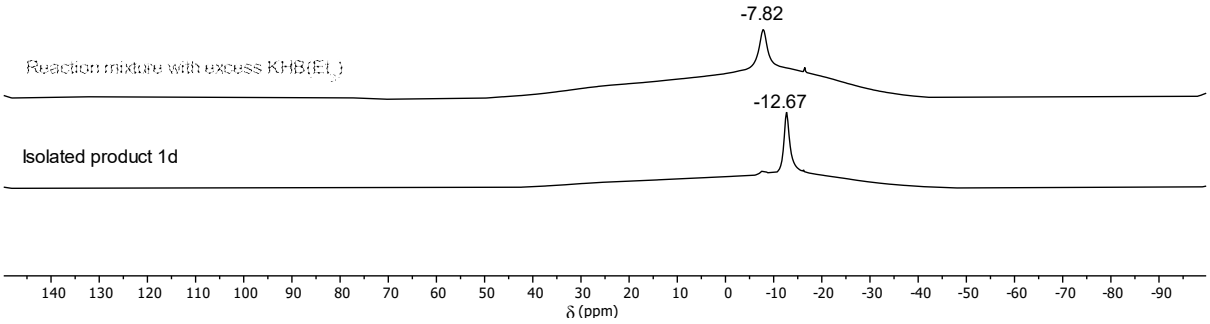


Figure A.96 $^{11}B\{^{1}H\}$ NMR spectra (benzene-d_6, 128.4 MHz, 298 K) [^{Me_2}SB(^{tBu_2}ArO,I*)ScH(BEt_3)(thf)] (**21**). Top; excess KHB(Et_3) is the only environment visible in the spectrum. Bottom; after filtering and removal of volatiles, a new boron $[BX_4]^-$ environment is present.

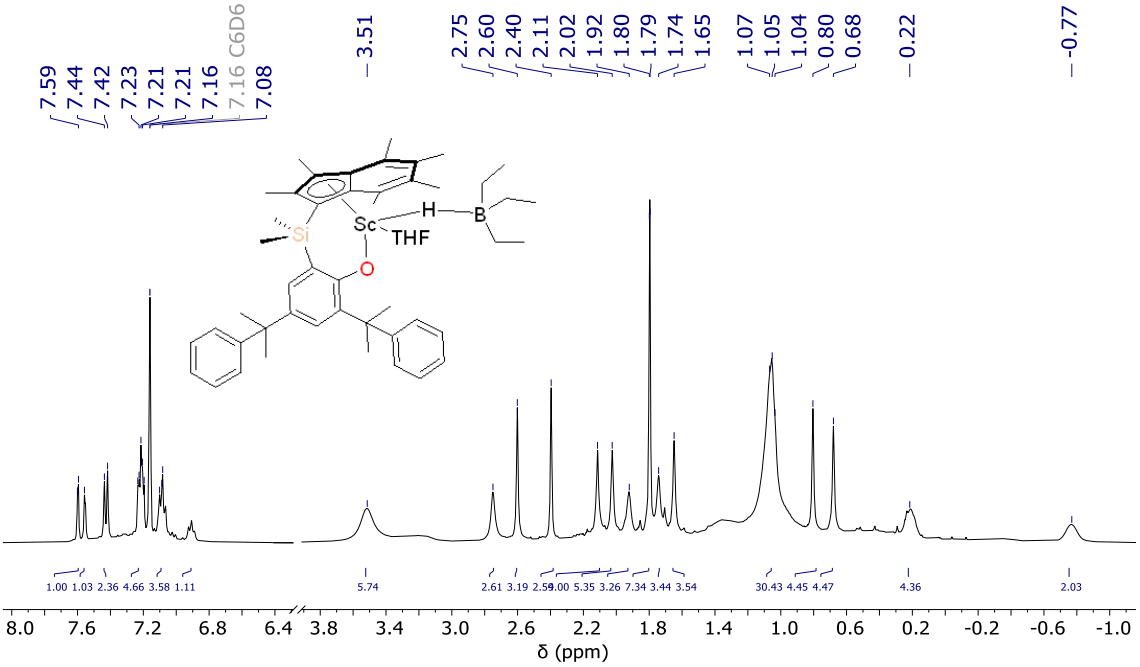


Figure A.97 ^{1}H NMR spectrum (benzene-d_6, 400 MHz, 298 K) of ^{Me_2}SB(^{Cumyl_2}ArO,I*)ScH(BEt_3)THF (**22**)

A.2.2. Crystallographic parameters

Experiments were carried out with Cu *K*α radiation. H-atom parameters were constrained.

Compound				
	^{Me_2}SB($^{t_{Bu_2}}$ArOAllyl,I*)H	^{Me_2}SB(^{Cumyl_2}ArOAllyl,I*)H	^{Me_2}SB($^{t_{Bu_2}}$ArO,I*)Sc(Cl)THF	^{Me_2}SB(^{Cumyl_2}ArO,I*)Sc(Cl)THF
			(1)	**(2)**
Crystal data				
Chemical formula	$C_{34}H_{50}OSi$	$C_{44}H_{54}OSi$	$C_{35}H_{52}ClO_2ScSi$	$C_{45}H_{55}ClO_2ScSi$
M_r	502.85	627.00	613.29	736.42
Crystal system, space group	Monoclinic, *I 2/a*	Triclinic, $P\bar{1}$	monoclinic, $P2_1/n$	Triclinic, $P\bar{1}$
Temperature (K)	150	150	150	150
a, *b*, *c* (Å)	22.3439(4), 15.8051(3), 17.2084(4)	9.2003(5), 12.9126(7), 16.6266(9)	10.78290(10), 12.62410(10), 25.8925(2)	10.5076(4), 12.0951(6), 15.4268(5)
α, β, γ (°)	90, 91.137(2), 90	90.508(4), 102.091(5), 107.826(5)	90, 99.5145 (6), 90	86.854 (3), 89.116 (3), 86.753 (3)
V (Å^3)	6075.9(2)	1833.03(18)	3476.12(5)	1954.35 (14)
Z	8	2	4	2
μ (mm^{-1})	0.84	0.79	3.049	2.80
Crystal size (mm)	0.18 × 0.13 × 0.13	0.11 × 0.10 × 0.02	0.17 × 0.04 × 0.04	0.20 × 0.14 × 0.06
Data collection				
Diffractometer	Oxford Diffraction SuperNova	Oxford Diffraction SuperNova	Oxford Diffraction SuperNova	Oxford Diffraction SuperNova
Absorption correction±	Multi-scan *CrysAlis PRO* (Rigaku Oxford Diffraction, 2017)	Multi-scan *CrysAlis PRO* (Rigaku Oxford Diffraction, 2017)	Multi-scan *CrysAlis PRO* (Rigaku Oxford Diffraction, 2017)	Multi-scan *CrysAlis PRO* (Rigaku Oxford Diffraction, 2017)
T_{min}, T_{max}	0.84, 0.90	0.95, 0.98	0.50, 0.69	0.59, 0.85
No. of measured,	17207, 6271, 5394	17566, 7576, 4916	90035, 7263, 6891	29385, 8087, 6370

independent and observed reflections				
R_{int}	0.039	0.065	0.032	0.056
$(\sin\theta/\lambda)_{max}$ (Å^{-1})	0.630	0.631	0.630	0.631
Refinement				
$R[F^2 > 2\sigma(F^2)]$, $wR(F^2)$, S	0.045, 0.128, 0.97	0.058, 0.154, 1.02	0.045, 0.135, 1.00	0.064, 0.189, 0.99
No. of reflections	6271	7575	7263	8083
No. of parameters	325	415	361	469
$(\Delta/\sigma)_{max}$	0.001	0.0004	0.002	0.001
$\Delta\rangle_{max}$, $\Delta\rangle_{min}$ (e Å^{-3})	0.51, -0.31	0.90, -0.54	1.48, -0.50	1.37, -0.44

Compound				
	^{Me_2}SB($^{t Bu}$N,I*)Sc(Cl)THF	^{Me_2}SB($^{t Bu_2}$ArO,I*)Sc(ODipp)THF	^{Me_2}SB($^{t Bu_2}$ArO,I*)Sc(Cl)*L*-La	^{Me_2}SB($^{t Bu_2}$ArO,I*)Sc(Cl)PDL
	(4)	**(5)**	**(24)**	**(25)**
Crystal Data				
Chemical formula	$C_{25}H_{41}ClNOScSi$	$C_{47}H_{69}O_3ScSi$	$C_{37}H_{52}ClO_5ScSi$	$CH_{72}ClO_3ScSi$
M_r	480.10	755.07	685.28	781.53
Crystal system, space group	Orthorhombic, *Pbca*	Triclinic, $P\bar{1}$	Monoclinic, $P2_1$	Monoclinic, P21/c
Temperature (K)	150	150	150	100
a, *b*, *c* (Å)	17.0197 (4), 16.2499 (3), 18.9958 (4)	10.042(4), 14.347(4), 34.390(3)	15.424 (3), 9.6762 (6), 16.6088 (9)	9.4443 (1), 11.0168 (1), 42.0714 (3)
α, β, γ (°)	90, 90, 90	88.911(18), 89.32(2), 70.27(3)	97.785 (9)	90, 94.304 (1), 90
V (Å^3)	5253.64 (19)	4663(2)	2455.9 (5)	4365.01 (7)
Z	8	4	2	4
μ (mm^{-1})	3.88	1.86	2.25	2.55
Crystal size (mm)	0.19 × 0.16 × 0.04	0.43 × 0.07 × 0.03	0.15 × 0.07 × 0.05	0.09 × 0.08 × 0.07
Data collection				
Diffractometer	Oxford Diffraction SuperNova	Oxford Diffraction SuperNova	SuperNova, Dual, Cu at home/near, Atlas	XtaLAB Synergy R, DW system, HyPix-Arc 150
Absorption correction	Multi-scan *CrysAlis PRO* (Rigaku Oxford Diffraction, 2017)	Multi-scan *CrysAlis PRO* (Rigaku Oxford Diffraction, 2017)	Gaussian *CrysAlis PRO* 1.171.43.90 (Rigaku Oxford Diffraction, 2023) Numerical absorption correction based on gaussian integration over a multifaceted crystal model Empirical absorption correction using spherical harmonics, implemented in SCALE3 ABSPACK scaling algorithm.	*CrysAlis PRO* 1.171.43.95a (Rigaku Oxford Diffraction, 2023) Empirical absorption correction using spherical harmonics, implemented in SCALE3 ABSPACK scaling algorithm.
T_{min}, T_{max}	0.53, 0.86	0.71, 0.95	0.805, 0.969	0.843, 1.000

No. of measured, independent and observed reflections	66653, 5488, 4147	127951, 19314, 11848	31299, 9933, 5315	56863, 8951, 8085
R_{int}	0.087	0.093	0.166	0.033
θ_{max} (°)				
$(\sin \theta/\lambda)_{max}$ (Å^{-1})	0.630	0.631	0.625	0.63
Refinement				
$R[F^2 > 2\sigma(F^2)]$, $wR(F^2)$, S	0.045, 0.132, 0.97	0.099, 0.111, 1.35	0.091, 0.270, 0.96	0.050, 0.144, 1.07
No. of reflections	5488	14007	9933	8951
No. of parameters	271	957	422	586
No. of restraints			1	321
$(\Delta/\sigma)_{max}$	0.001	0.001	0.001	0.001
$\Delta\rangle_{max}$, $\Delta\rangle_{min}$ (e Å^{-3})	0.53, -0.48	0.99, -0.43	0.58, -0.54	0.45, −0.42
Absolute structure			Classical Flack method preferred over Parsons because s.u. lower.	
Absolute structure parameter			-0.01 (2)	

Compound			
	$^{Me}{}_2$SB(^{t}Bu$_2$ArO,I*)Sc(ODipp)ϵ-CL	Sc(ODipp)$_3$.2THF	Sc(O-2,4-^{t}Bu-C$_6$H$_3$)$_3$.2THF
	(26)	**(29)**	**(30)**
Crystal Data			
Chemical formula	$C_{49}H_{71}O_4ScSi$	$C_{44}H_{67}O_5Sc$	$C_{50}H_{79}O_5Sc$
M_r	797.1	720.97	805.13
Crystal system, space group	Triclinic, $P\bar{1}$	Monoclinic, $P2_1$	Triclinic, P -1
Temperature (K)	100	100	150
a, *b*, *c* (Å)	11.1877 (2), 11.6134 (2), 17.9297 (3)	9.5052(3), 19.1442(5), 12.0869(3)	11.4448(4), 16.3910(4), 18.0125(7)
α, β, γ (°)	84.145 (1), 78.973 (2), 87.280 (1)	90, 109.231(3), 90	98.969(3), 90.312(3), 98.759(3)
V (Å^3)	2273.69 (7)	2076.71(10)	3297.28(19)
Z	2	2	2
μ (mm^{-1})	1.95	0.22	1.62
Crystal size (mm)	0.09 × 0.07 × 0.06	0.16 × 0.03 × 0.02	0.27 × 0.15 × 0.06
Data collection			
Diffractometer	XtaLAB Synergy R, DW system, HyPix-Arc 150	XtaLAB Synergy DW	Oxford Diffraction SuperNova
Absorption correction	Multi-scan. CrysAlis PRO 1.171.43.95a (Rigaku Oxford Diffraction, 2023) Empirical absorption correction using spherical	Multi-scan *CrysAlis PRO* (Rigaku Oxford Diffraction, 2017)	Multi-scan *CrysAlis PRO* (Rigaku Oxford Diffraction, 2017)

	harmonics, implemented in SCALE3 ABSPACK scaling algorithm.		
T_{min}, T_{max}	0.770, 1.000	0.76, 1.00	0.76, 0.91
No. of measured, independent and observed reflections	97519, 9322, 8602	66985, 12643, 9379	56116, 10036, 8671
R_{int}	0.036	0.086	0.042
θ_{max} (°)			
$(\sin\theta/\lambda)_{max}$ (Å^{-1})	0.630	0.714	0.631
Refinement			
$R[F^2 > 2\sigma(F^2)]$, $wR(F^2)$, S	0.042, 0.113, 1.07	0.042, 0.087, 0.87	0.039, 0.109, 0.99
No. of reflections	9322	12643	10034
No. of parameters	545	451	505
No. of restraints	18	1	
$(\Delta/\sigma)_{max}$	0.001	0.0003	0.001
$\Delta\rangle_{max}$, $\Delta\rangle_{min}$ (e Å^{-3})	0.91, −0.58	0.55, -0.51	0.59, -0.34

Computer programs: SuperNova, (Oxford Diffraction, 2010), *CrysAlis PRO* 1.171.39.46 (Rigaku OD, 2018), *CrysAlis PRO* 1.171.41.93a (Rigaku OD, 2020), *CrysAlis PRO* (Rigaku Oxford Diffraction, 2017), *SUPERFLIP* (Palatinus & Chapuis, 2007), *SUPERFLIP* Palatinus, L.; Chapuis, G. J. Appl. Cryst. 2007, 40, 786-790., *CRYSTALS* (Betteridge *et al.*, 2003), *SHELXL2014* (Sheldrick, 2014), *SHELXL2018*/3 (Sheldrick, 2018), *CAMERON* (Watkin *et al.*, 1996), *ORTEP-3 for Windows* (Farrugia, 1997), *ORTEP-3 for Windows* Farrugia, L. J. J. Appl. Cryst. 1997, 30, 565., *WinGX* publication routines (Farrugia, 1999).

.

A.3. Supplementary data for Chapter Four

A.3.1. NMR and IR spectra of synthesised compounds

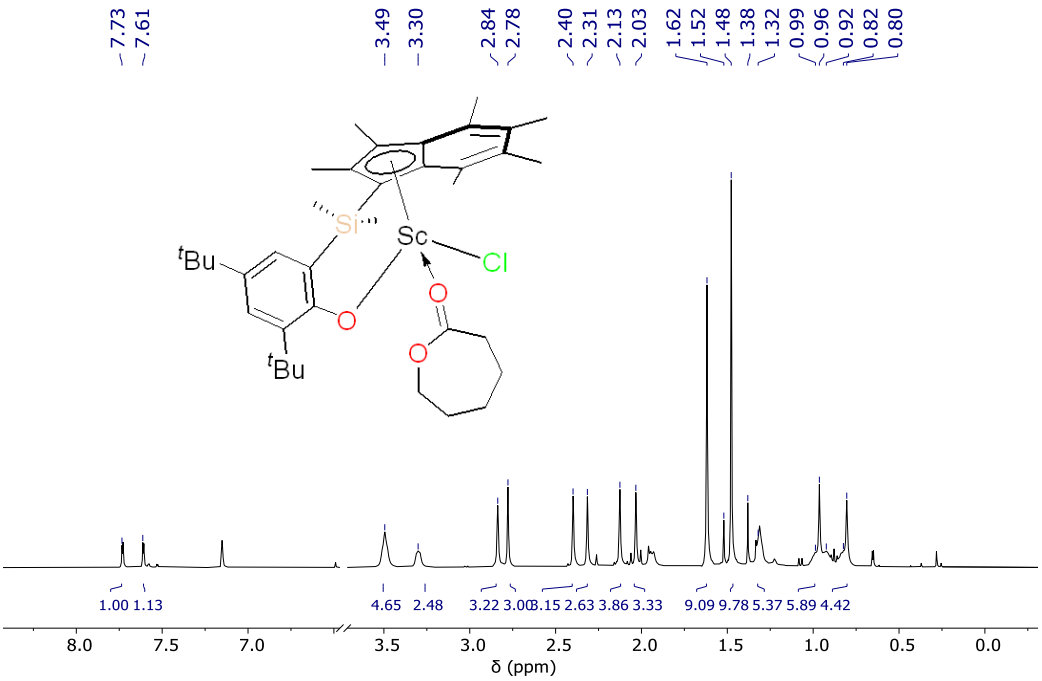


Figure A.98 ^{1}H NMR spectrum (benzene-d_6, 600 MHz, 298 K) of ^{Me_2}SB($^{t\text{Bu}}$OAr,I*)Sc(Cl)ϵ-CL (**23**)

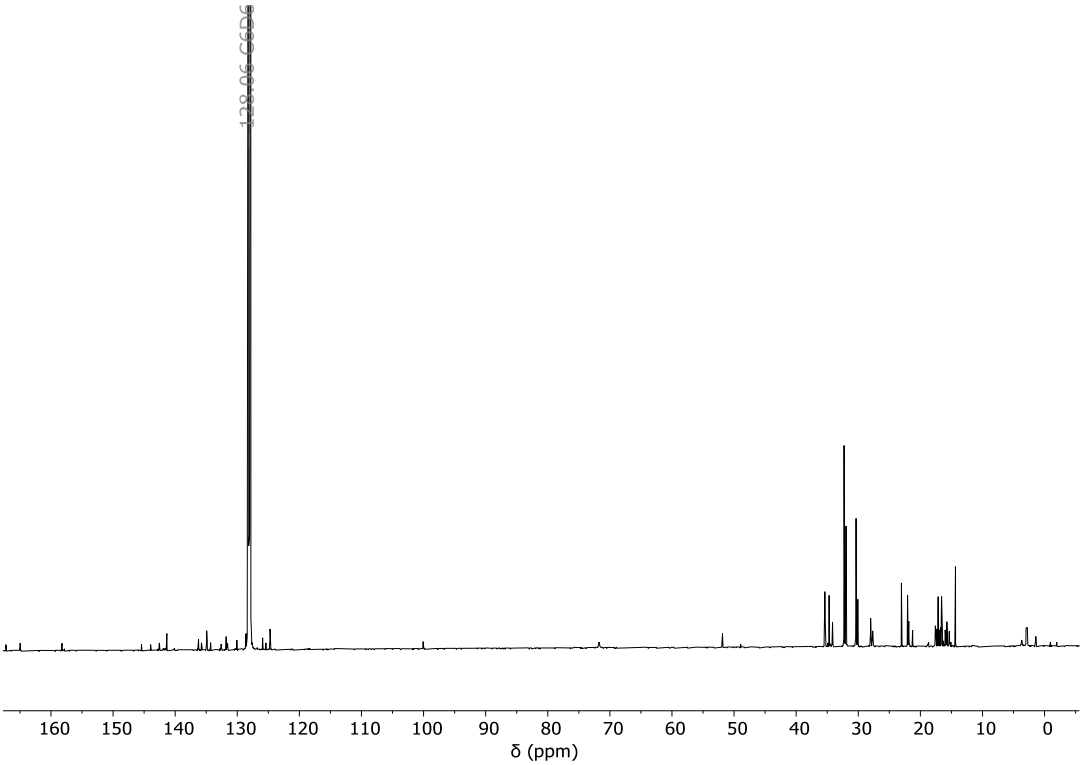


Figure A.99 ^{13}C{^{1}H} NMR spectrum (benzene-d_6, 151 MHz, 298 K) of ^{Me_2}SB($^{t\text{Bu}}$OAr,I*)Sc(Cl)ϵ-CL (**23**)

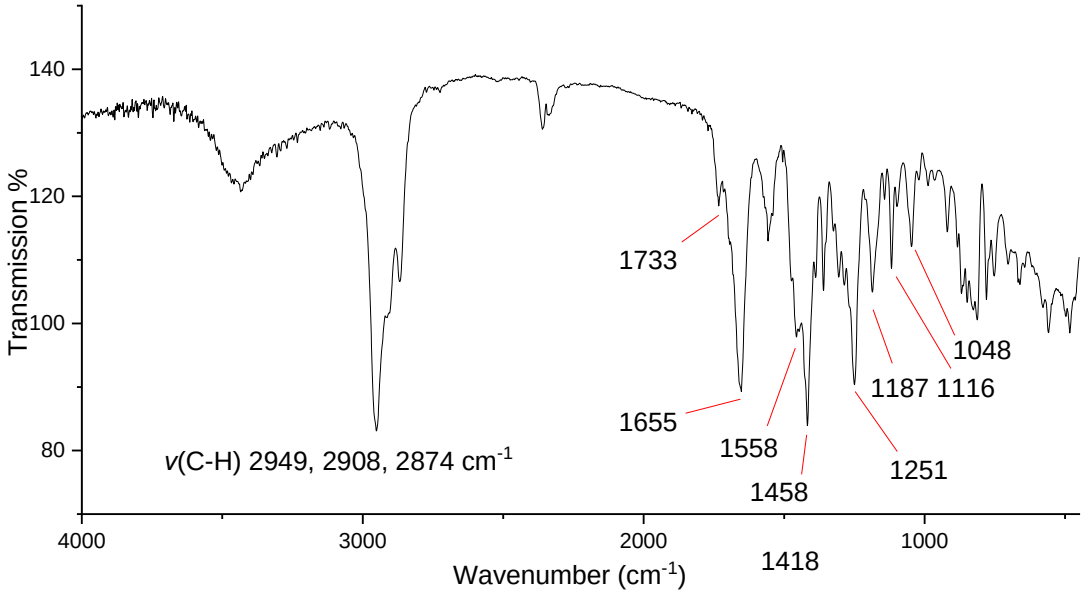


Figure A.100 IR of spectrum (KBr disk) ^{Me_2}SB(^{tBu}OAr,I*)Sc(Cl)ϵ-CL (**23**) 4000–450 cm^{-1}

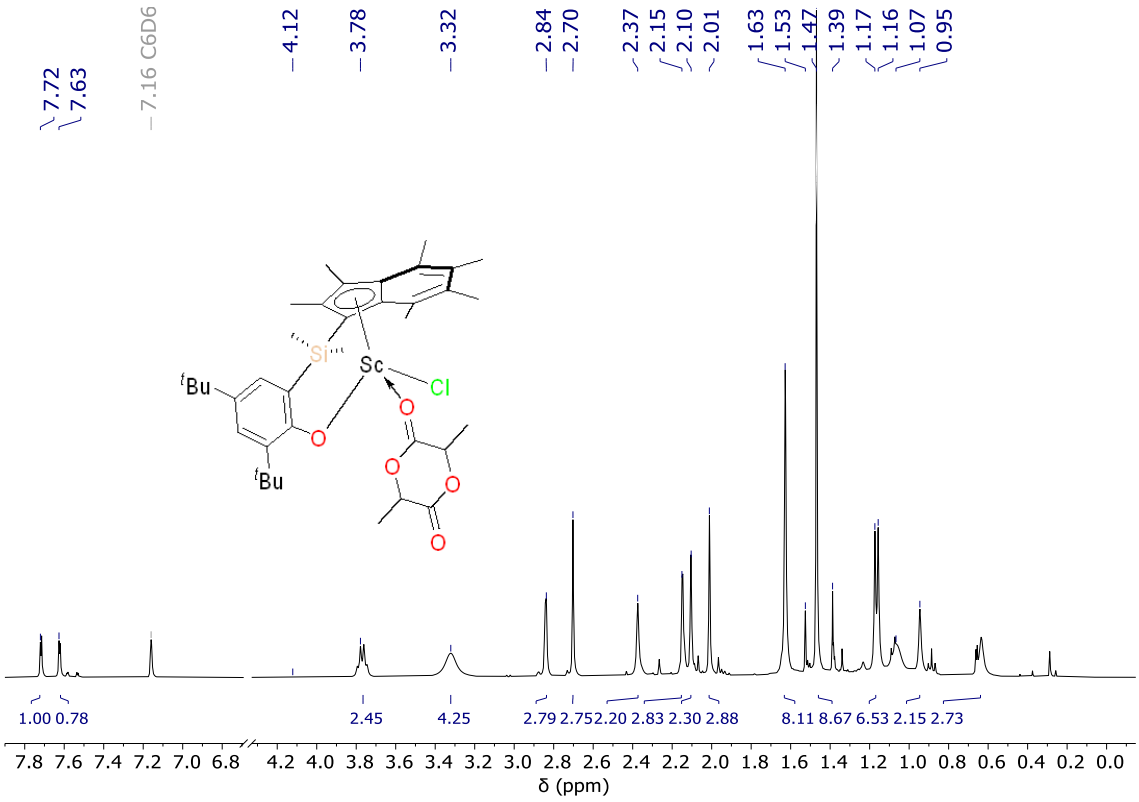


Figure A.101 ^{1}H NMR spectrum (benzene-d_6, 600 MHz, 298 K) of ^{Me_2}SB(^{tBu}OAr,I*)Sc(Cl)*L*-La (**24**)

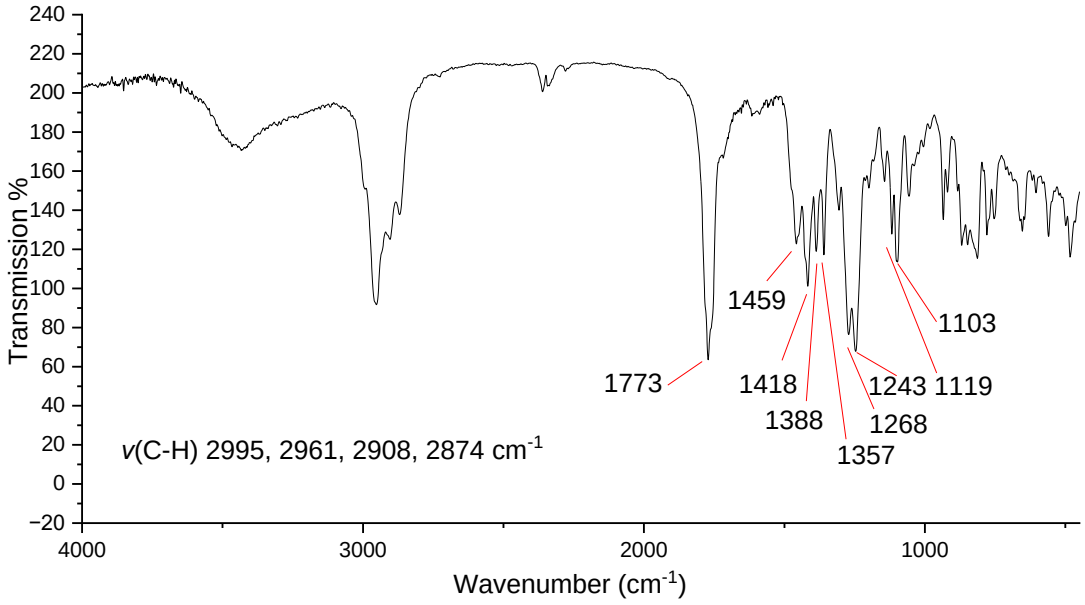


Figure A.102 IR of spectrum (KBr disk) ^{Me_2}SB(^{tBu}OAr,I*)Sc(Cl)L-La (**24**) 4000–450 cm^{-1}

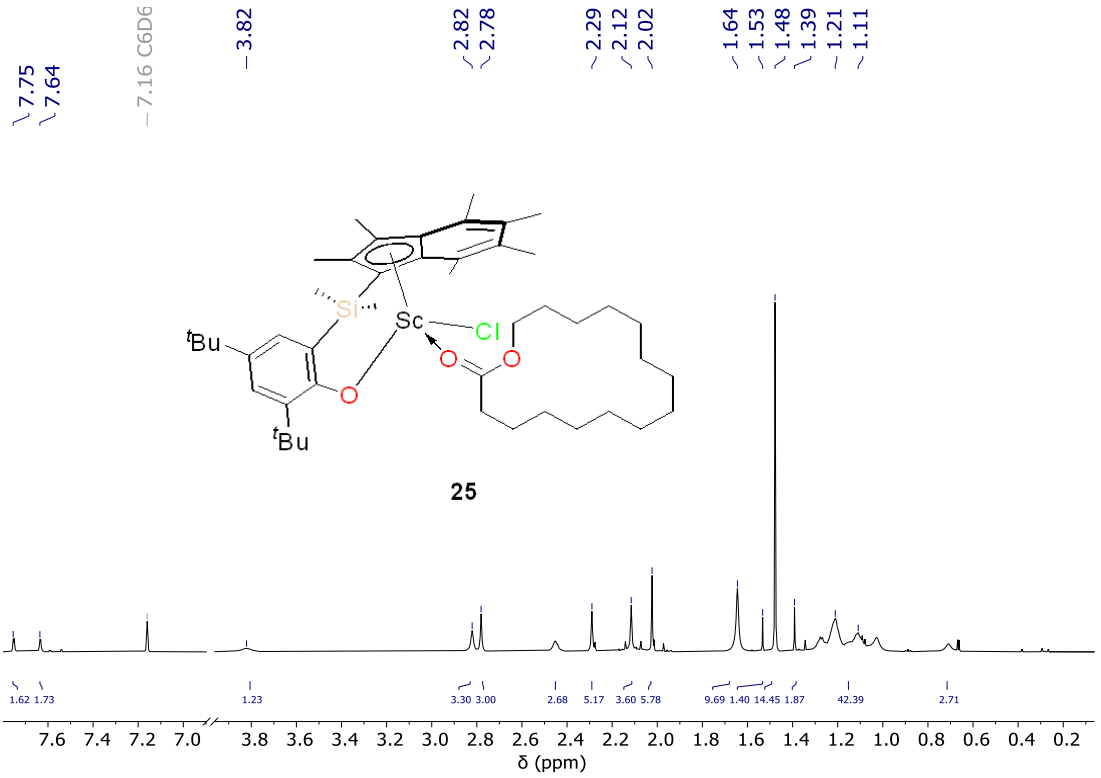


Figure A.103 ^{1}H NMR spectrum (benzene-d_6, 600 MHz, 298 K) of ^{Me_2}SB(^{tBu}OAr,I*)Sc(Cl)PDL **(25)**

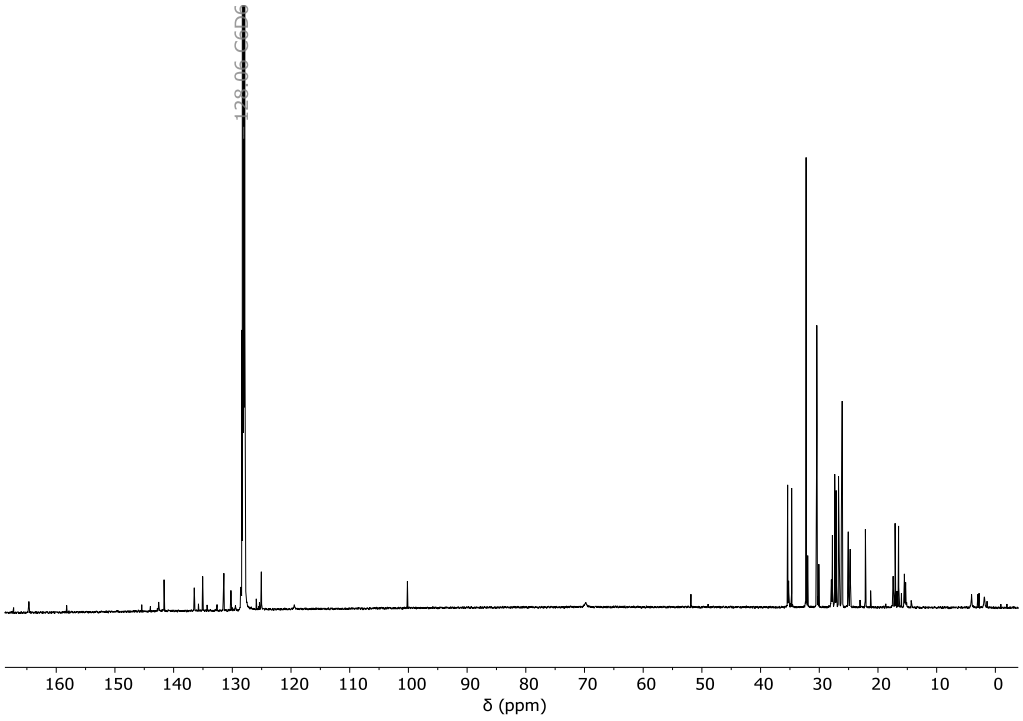


Figure A.104 $^{13}C\{^{1}H\}$ NMR spectrum (benzene-d_6, 151 MHz, 298 K) of ^{Me_2}SB($^{t\text{Bu}}$OAr,I*)Sc(Cl)PDL (**25**)

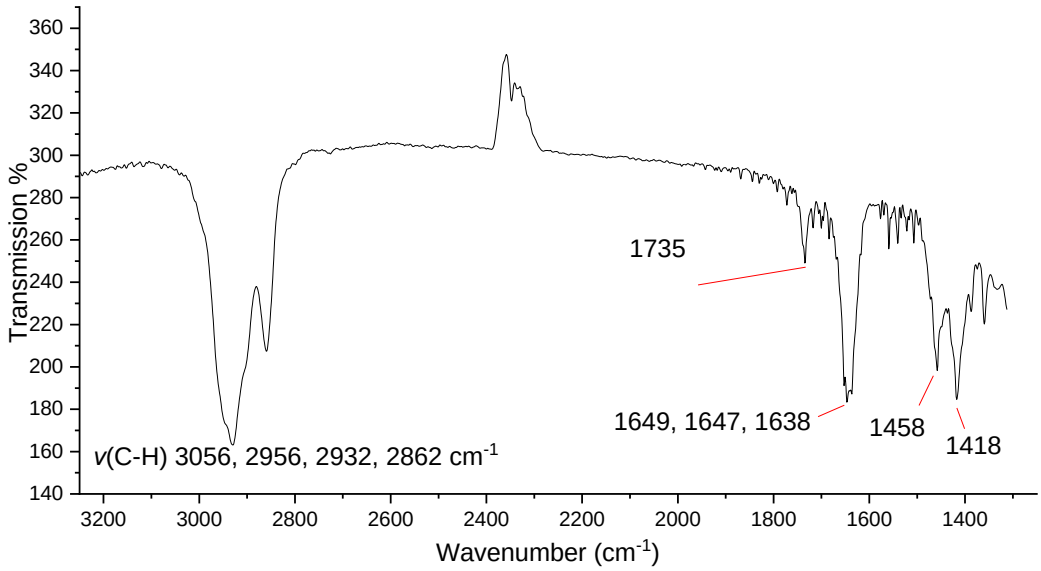


Figure A.105 IR of spectrum (KBr disk) ^{Me_2}SB($^{t\text{Bu}}$OAr,I*)Sc(Cl)PDL (**25**) 3325–1250 cm^{-1}

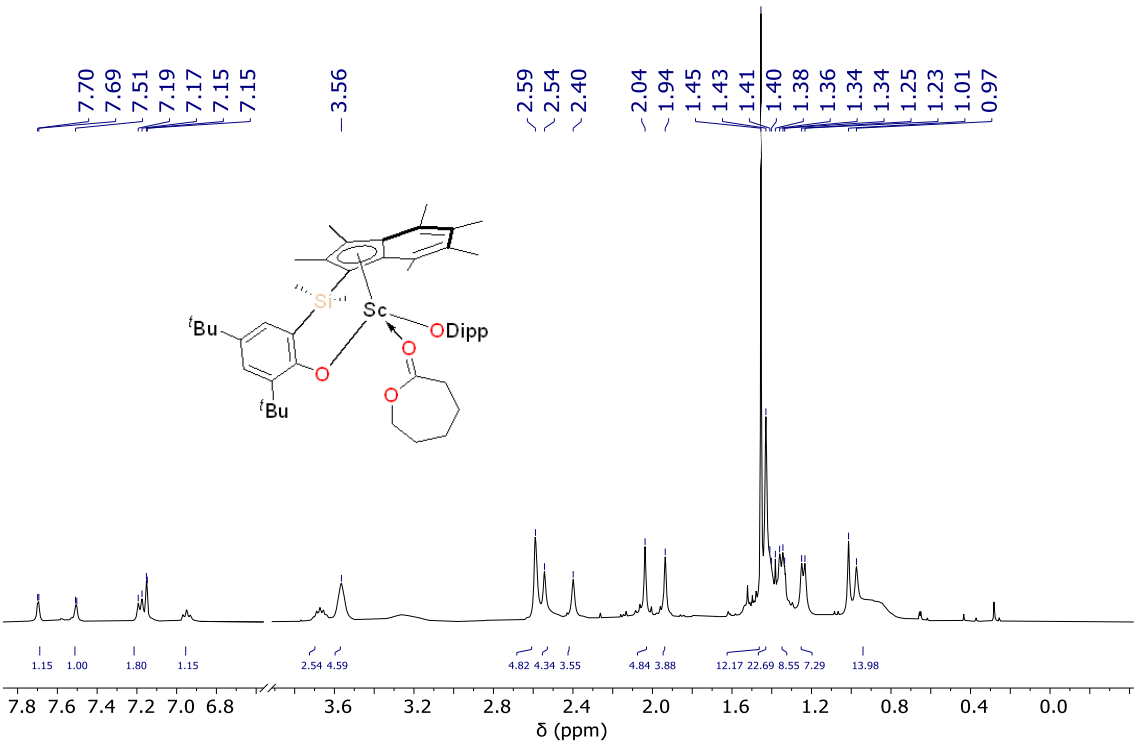


Figure A.106 ^{1}H NMR spectrum (benzene-d_6, 600 MHz, 298 K) of ^{Me_2}SB(^{tBu}OAr,I*)Sc(ODipp)ϵ-CL **(26)**

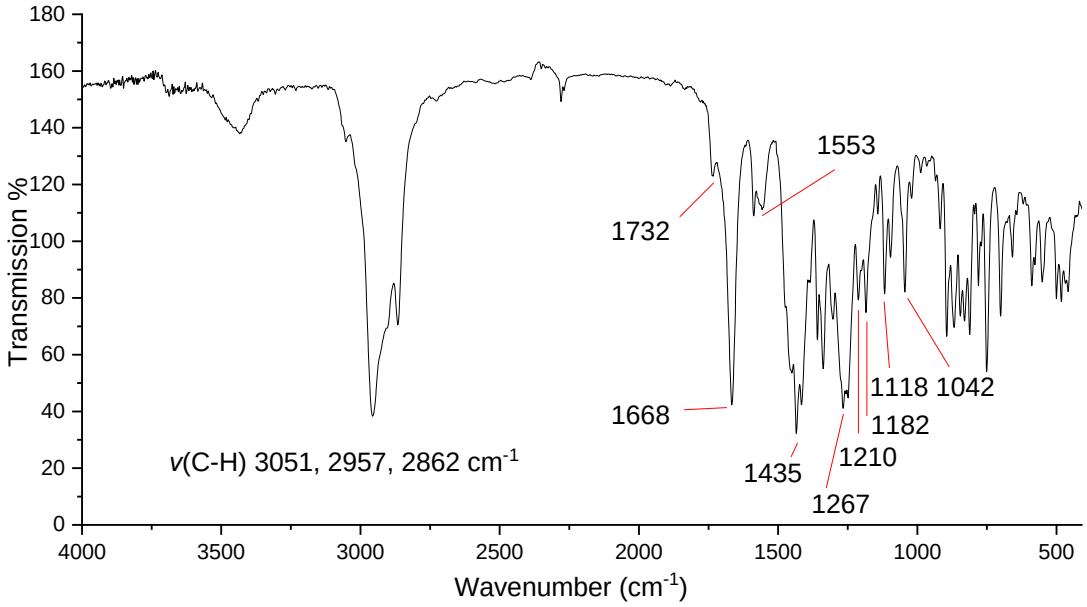


Figure A.107 IR of spectrum (KBr disk) ^{Me_2}SB(^{tBu}OAr,I*)Sc(ODipp)ϵ-CL (**26**) 4000–450 cm^{-1}

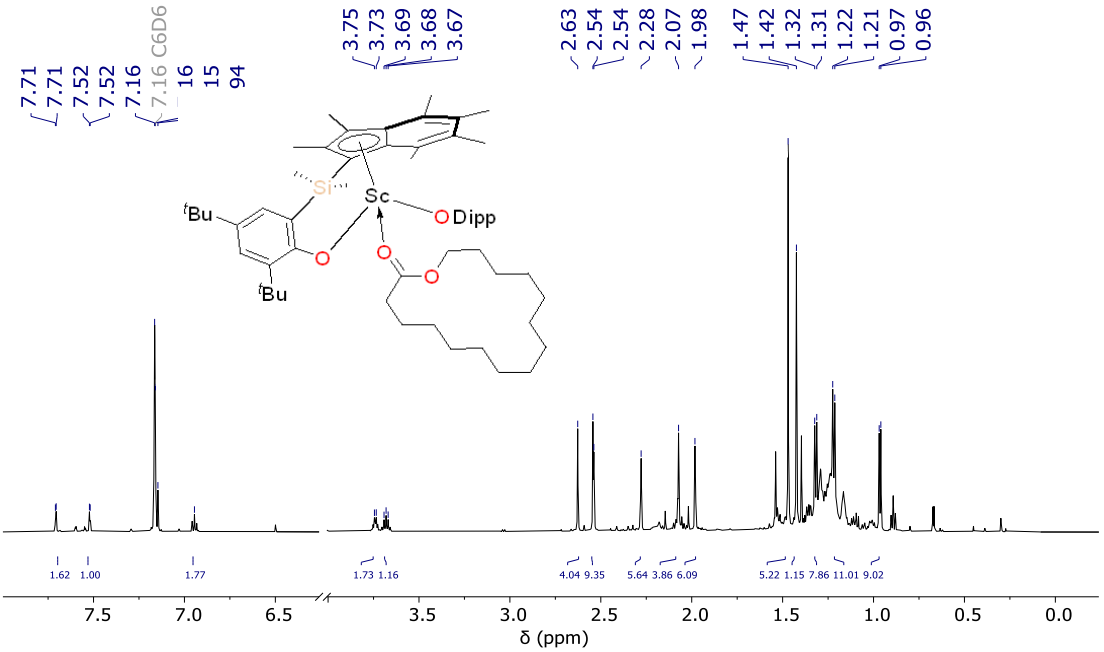


Figure A.108 ^{1}H NMR spectrum (benzene-d_6, 600 MHz, 298 K) of ^{Me_2}SB($^{t Bu}$OAr,I*)Sc(ODipp)PDL (**28**)

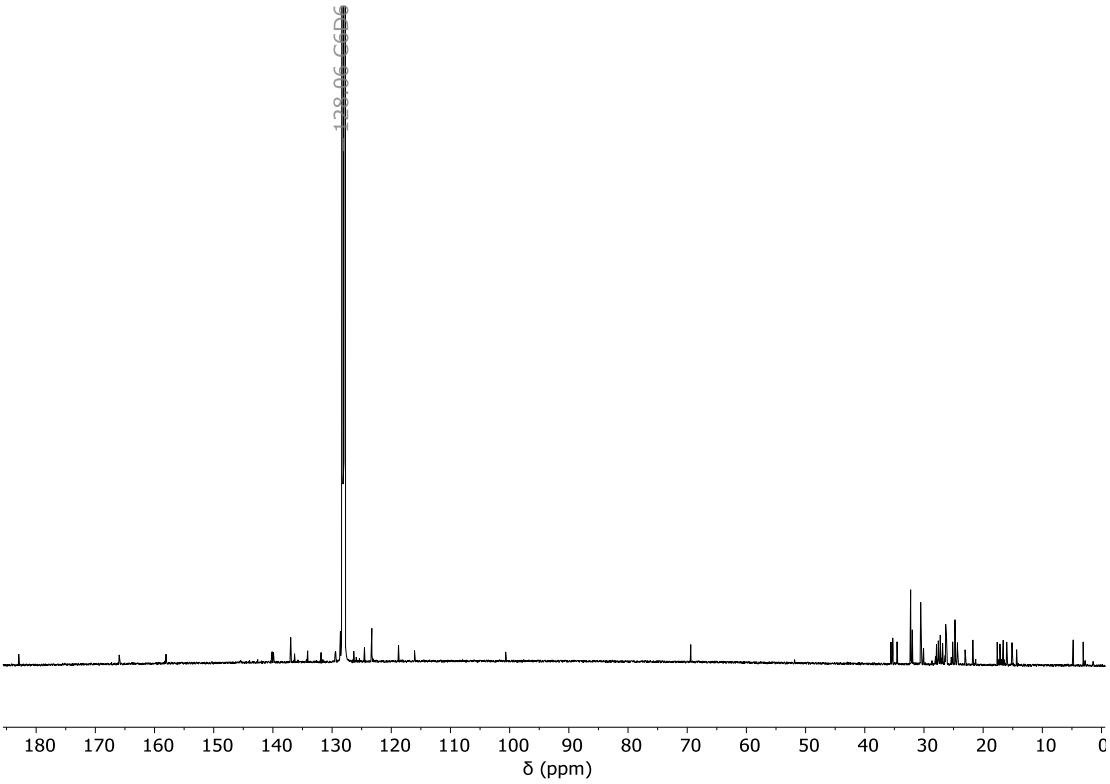


Figure A.109 ^{13}C{^{1}H} NMR spectrum (benzene-d_6, 151 MHz, 298 K) of ^{Me_2}SB($^{t Bu}$OAr,I*)Sc(ODipp)PDL (**28**)

28

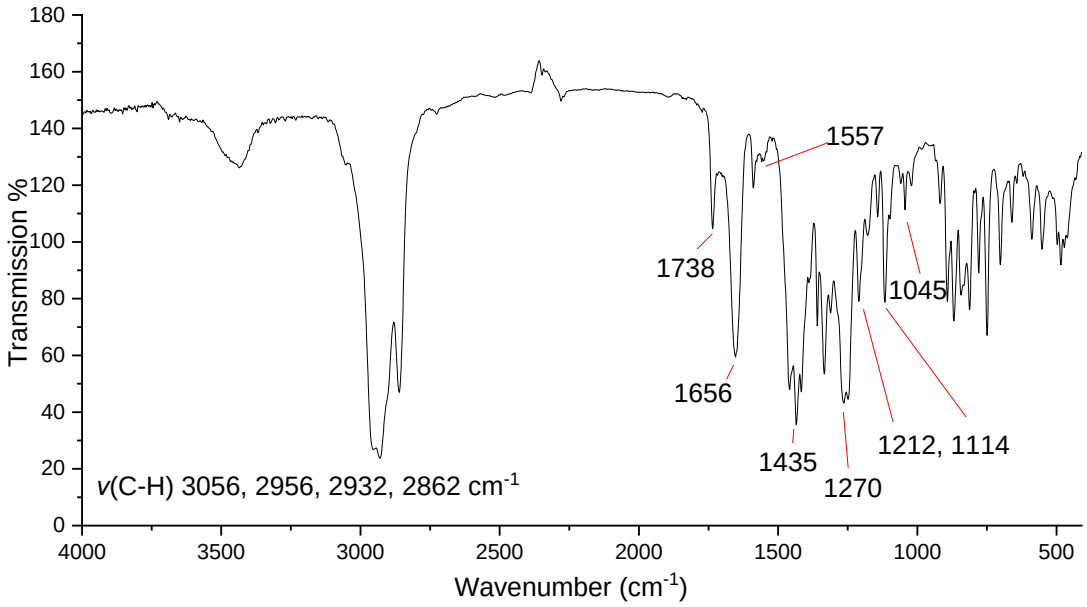


Figure A.110 IR of spectrum (KBr disk) ^{Me_2}SB($^{t\text{Bu}}$OAr,I*)Sc(ODipp)PDL (**28**) 4000–450 cm^{-1}

A.3.2. Additional crystallographic information

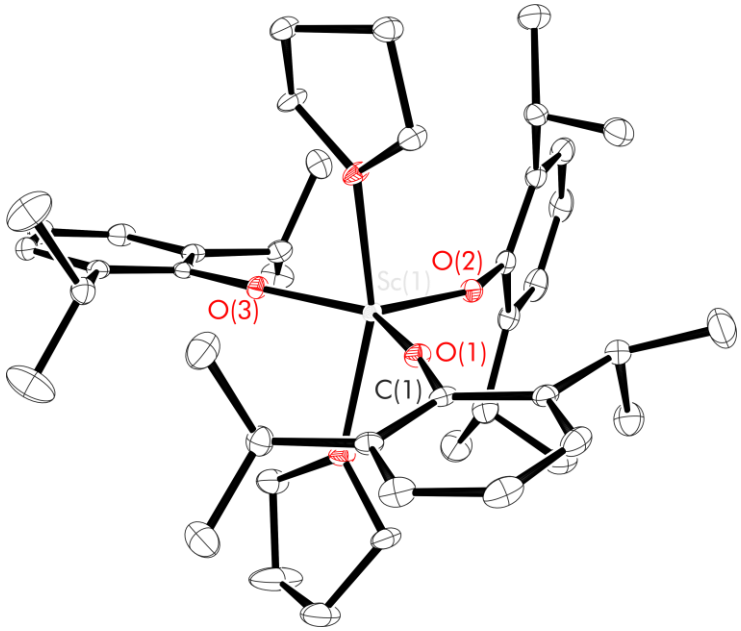


Figure A.111 Solid state structure of Sc(ODipp)$_3$.2THF (**29**) Ellipsoids are drawn at 30% probability and all non-chiral hydrogen atoms are omitted for clarity.

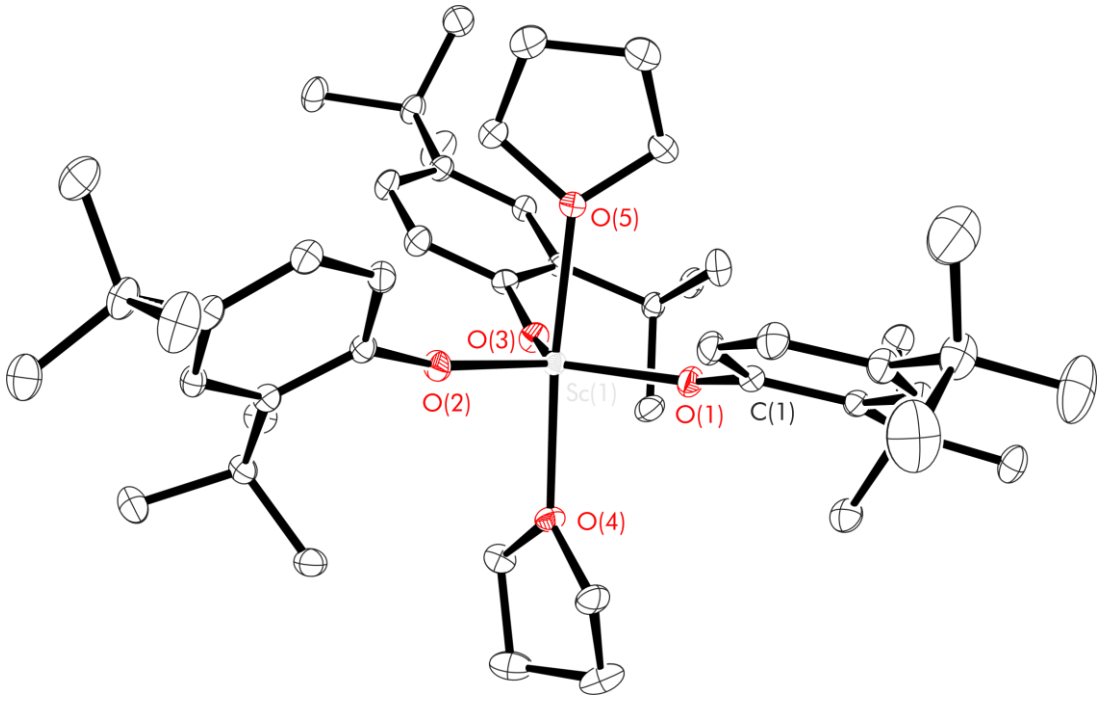


Figure A.112 Solid state structure of Sc(^{t}Bu$_2$ArO)$_3$.2THF (**30)** Ellipsoids are drawn at 30% probability and all non-chiral hydrogen atoms are omitted for clarity.

Table A.1 Experimental metrical parameters (bond lengths (Å) and angles (°)) for **29** and **30.** Estimated standard deviations shown in brackets

Parameter	(**29**)	(**30**)
X	ODipp	^{t}Bu
Sc-O	1.9283(12)	1.9657(11)
Sc-O	1.9338(12)	1.9221(12)
Sc-O	1.9356(13)	1.9356(12)
Sc-O^{THF}	2.2061(13)	2.1969(11)
Sc- O^{THF}	2.2092(13)	2.2000(13)

For Sc(^{R}$_2$ArO)$_3$.2THF, X is anionic ligand

A.3.3. Polymerisation Characterisation for Chapter 4

A.3.3.1. 1–3 and ϵ-CL (BnOH)

Table A.2 ROP of ϵ-CL initiated by Sc complexes **1**–**3** with BnOH co-intiator.

Cat.	$[M]_0/[Sc]_0$	Time (h)	Conv.[a] (%)	k_{obs} (h^{-1})	R^2	$M_{n,SEC}$[b] (kDa)	$M_{n,th}$[a,c] (kDa)	$Đ_M$[b]
1	50	2.0	80	0.90±0.010	0.993	9.7(6.3)	4.6	1.58(1.51)
1	400	24.0	90	0.09±0.003	0.999	15.8(10.0)	41.0	1.14(1.13)
2	50	7.6	66	0.14±0.003	0.999	7.7(5.1)	3.7	1.30(1.26)
3	50	3.8	70	0.31±0.003	0.999	12.4(7.6)	4.0	1.17(1.15)

Conditions: $[ϵ\text{-CL}]_0$:$[Sc]_0$:[BnOH] as 50:1:1, $[ϵ\text{-CL}]_0$ = 0.5 M in 0.6 mL benzene-d_6 at 25 °C. [a] Measured by ^{1}H NMR spectroscopic analyses. First-order rate constant (k_{obs}) and R^2 were obtained from plots of $\ln([ϵ\text{-CL}]_0/[ϵ\text{-CL}]_t)$ *vs* time. [b] [c] Calculated from monomer conversion data: $[M]_0/[Sc]_0$ × conv. (%) × 114.14 × 0.01 + (MW of end groups (α+ω)) in kDa.[d] Houwink correction factor used for values in brackets; K = 13.95 × 10^{-5} dL/g; a = 0.786.[15]

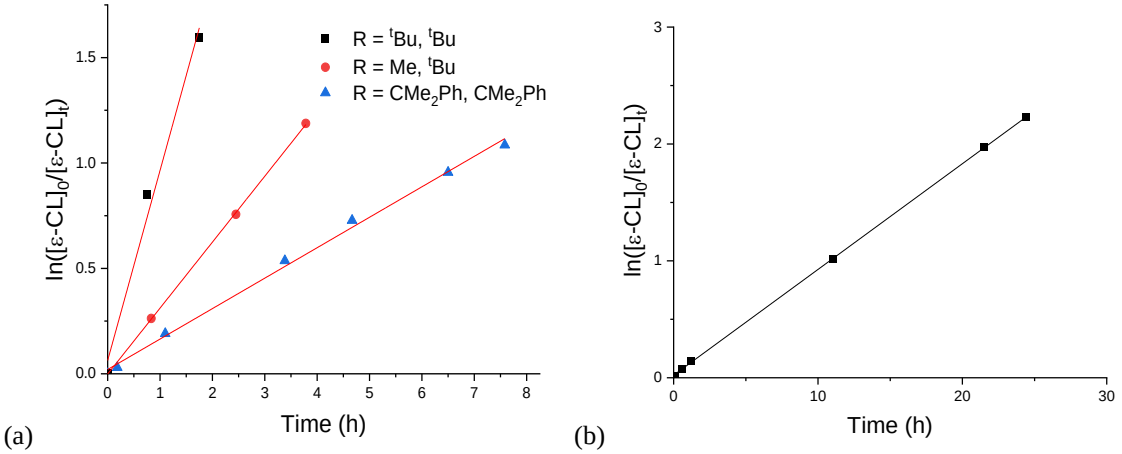


Figure A.113 Plots of $\ln([ϵ\text{-CL}]_0/[ϵ\text{-CL}]_t)$ *vs.* Time (h) (a) 1, Black square (k_{obs} = 0.90±0.010^{-1}. R^2 = 0.993); **2** red circles (k_{obs} = 0.14±0.003^{-1}. R^2 = 0.999); **3**, blue upward triangles (k_{obs} = 0.31±0.003^{-1}). Conditions: $[ϵ\text{-CL}]_0$:[**Sc**]$_0$ = 50:1, $[ϵ\text{-CL}]_0$ = 0.5 M in 0.6 mL benzene-d_6.(b) (k_{obs} = 0.09±0.003^{-1}. R^2 = 0.999). Conditions: $[ϵ\text{-CL}]_0$:[**1**]$_0$ = 400:1; $[ϵ\text{-CL}]_0$ = 0.5 M in 0.6 mL (**5**) Benzene-d_6

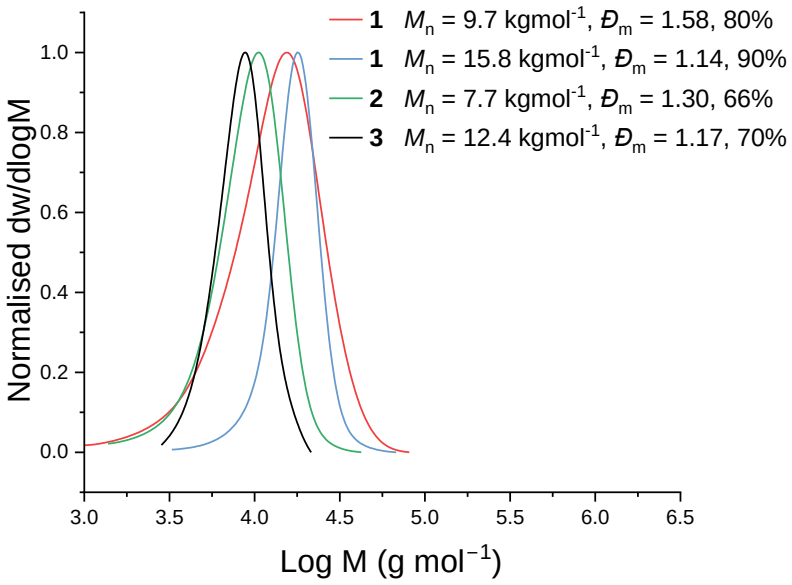


Figure A.114 Gel permeation chromatograms of ϵ-CL synthesised by **1**, **2**, and **3**. Conditions: [ϵ-CL]$_0$:[Sc]$_0$ = 50:1 or blue = 400:1; [ϵ-CL]$_0$ = 0.5 M in 0.6 mL (**5**) Benzene-d_6

A.3.3.2. ϵ-CL using 1

Table A.3 ROP of ϵ-CL initiated by Sc complexes **1**.

Cat.	[M]$_0$/[Sc]$_0$	Time (h)	Conv.[a] (%)	k_{obs} (h^{-1})	R^2	$M_{n,SEC}$[b] (kDa)	$M_{n,\ th}$[a,c] (kDa)	$Đ_M$[b]
1	50	70	99	0.079±0.0002	0.999	44(27)	5	1.74(1.65)

Conditions: [ϵ-CL]$_0$:[Sc]$_0$ as 50:1, [ϵ-CL]$_0$ = 0.5 M in 0.6 mL benzene-d_6 at 25 °C. [a] Measured by ^{1}H NMR spectroscopic analyses. First-order rate constant (k_{obs}) and R^2 were obtained from plots of ln([ϵ-CL]$_0$/[ϵ-CL]$_t$) *vs* time. [b] [c] Calculated from monomer conversion data: [M]$_0$/[Sc]$_0$ × conv. (%) × 114.14 × 0.01 + (MW of end groups (α+ω)) in kDa.[d] Houwink correction factor used for values in brackets; K = 13.95 × 10^{-5} dL/g; a = 0.786.[16]

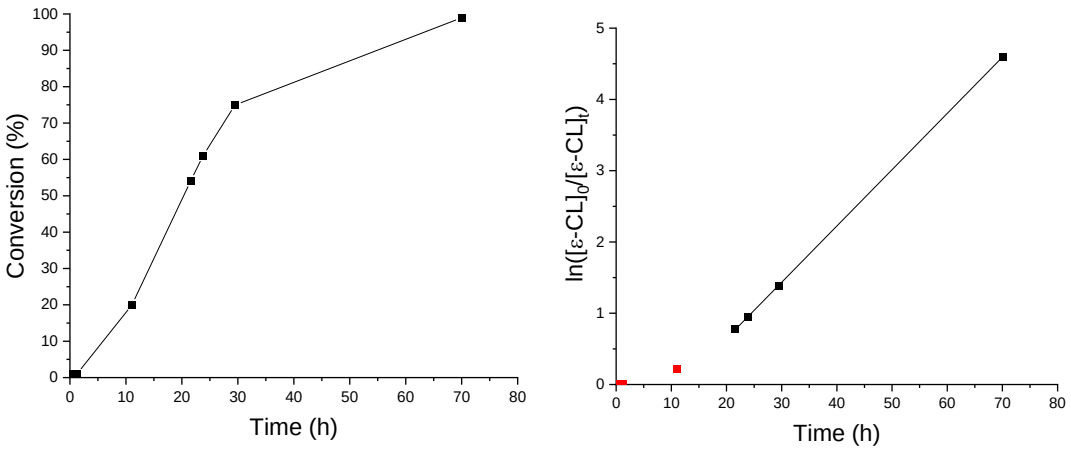


Figure A.115 (a) Plots of percentage conversion *vs.* time synthesised by **1**. (b) Plots of ln([ϵ-CL]$_0$/[ϵ-CL]$_t$) *vs.* Time (h) (k_{obs} = 0.079±0.0002^{-1}. R^2 = 0.999). Conditions: [ϵ-CL]$_0$:[**1**]$_0$ = 50:1, [ϵ-CL]$_0$ = 0.5 M in 0.6 mL benzene-d_6.

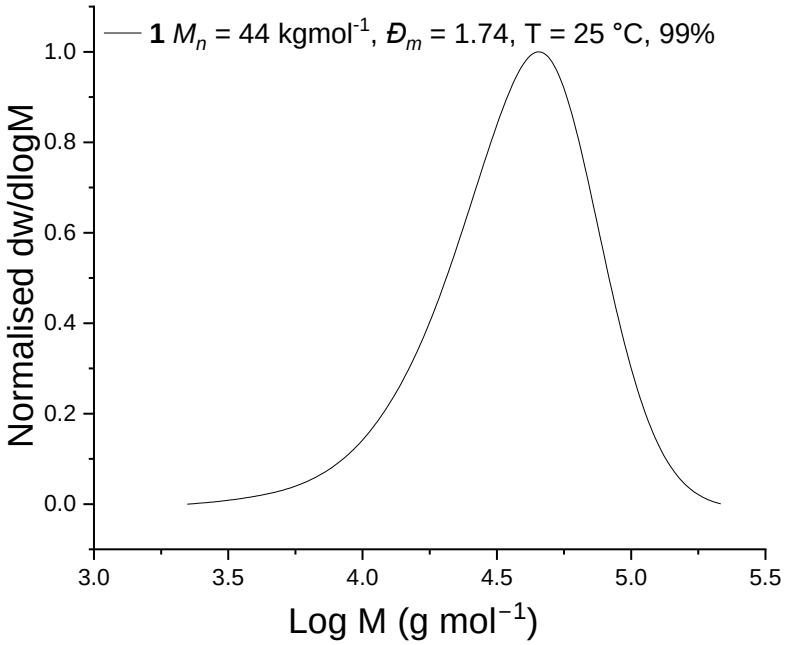


Figure A.116 Gel permeation chromatograms of ϵ-CL synthesised by **1.** Conditions: [ϵ-CL]$_0$:[**1**]$_0$ = 50:1, [ϵ-CL]$_0$ = 0.5 M in 0.6 mL benzene-d_6.

A.3.3.3. ϵ-CL using 5 - Variable concentration and temperature

Table A.4 ROP of ϵ-CL using **5** at various stoichiometries

Cat.	$[M]_0/[Sc]_0$	Temp. (°C)	Time (min)	Conv.[a]	k_{obs} (h^{-1})	R^2	$M_{n,SEC}$[b,(d)]	$M_{n,\,th}$[a,c]	$Đ_M$[b]
5	200	25	460	80	0.24±0.01	0.998	144	23	1.90
5	400	25	1740	80	0.067±0.01	0.999	111	44	2.30
5	800	25	1750	45	0.02±0.003	0.998	-[e]	-	-

Conditions: $[ϵ\text{-CL}]_0:[Sc]_0$ as stated; $[ϵ\text{-CL}]_0$ = 0.5 M in 0.6 mL (**5**) Benzene-d_6. First-order rate constant (k_{obs}) and R_2 were obtained from plots of $\ln([ϵ\text{-CL}]_0/[ϵ\text{-CL}]_t)$ *vs* time. [c] Calculated from monomer conversion data: $[M]_0/[Sc]_0$ × conv. (%) × 114.14 × 0.01 + (MW of end groups (α+ω)).[d] polystyrene standard used. [e] Sample blocked column, hence no measurement taken.

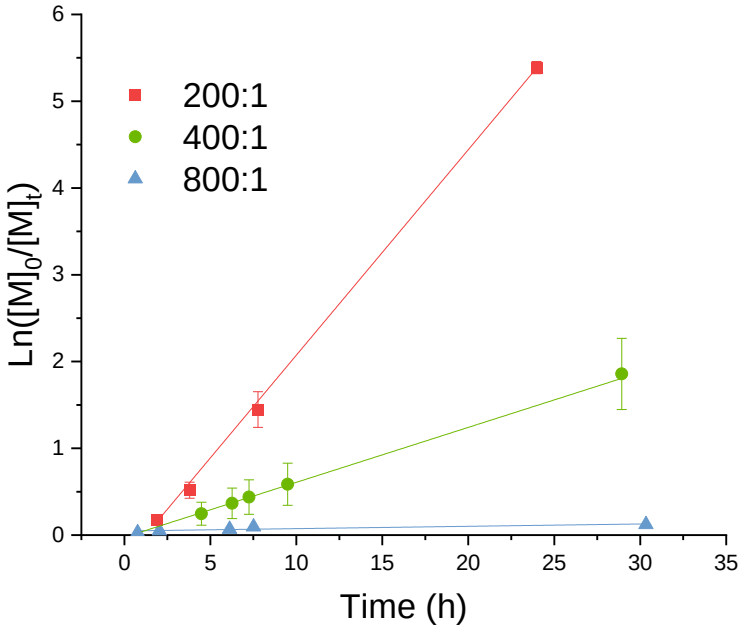


Figure A.117 Plots of $\ln([ϵ\text{-CL}]_0/[ϵ\text{-CL}]_t)$ *vs.* time. Red squares: 200 (k_{obs} = 0.24±0.01 h^{-1}. R^2 = 0.998); blue circles: 40 °C (k_{obs} = 0.396 h^{-1}. R^2 = 0.999); green upward triangles: 50 °C (k_{obs} = 0.612 h^{-1}. R^2 = 0.999); Conditions: $[ϵ\text{-CL}]_0:[Sc]_0$ as stated; $[ϵ\text{-CL}]_0$ = 0.5 M in 0.6 mL (**5**) Benzene-d_6

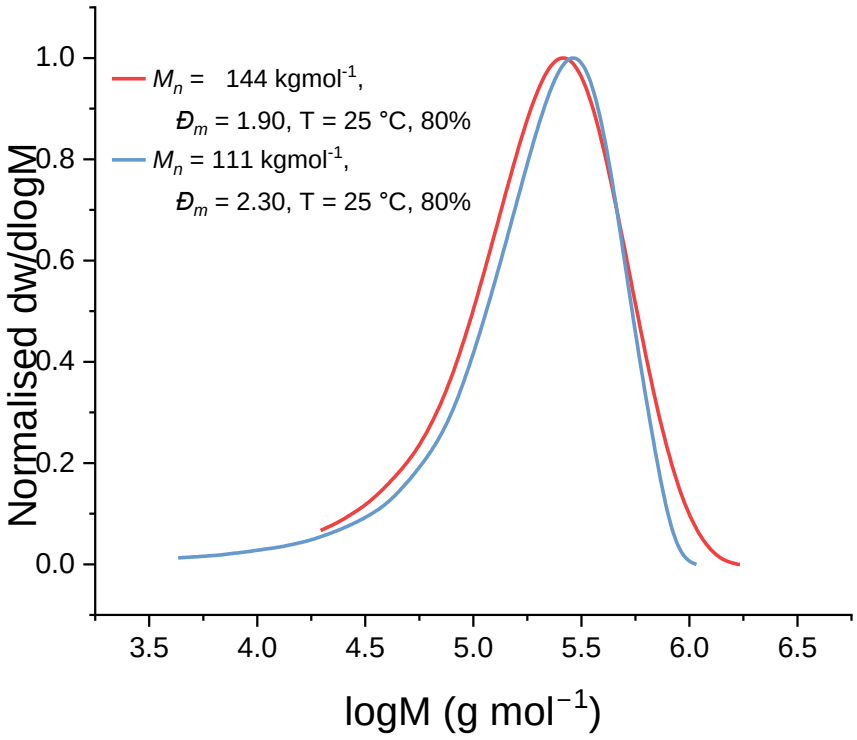


Figure A.118 Gel permeation chromatograms of ϵ-CL synthesised by **5** as a function of concentration: Conditions: $[\epsilon\text{-CL}]_0$:$[Sc]_0$ as stated; $[\epsilon\text{-CL}]_0$ = 0.5 M in 0.6 mL (**5**) Benzene-d_6

Table A.5 ROP of ϵ-CL initiated by **5** across variable temperature at 200:1 [ϵ-Cl]:[**5**].

Temp. (°C)	Time (h)	Conv.[a] (%)	k_{obs} (h^{-1})	R^2	$M_{n,SEC}$[b] *(kDa)*	$M_{n,\,th}$[a,c] *(kDa)*	$Đ_M$[b]
30	7.4	76	0.224±0.004	0.999	93	23	1.82
40	2.2	63	0.441±0.012	0.999	143	16	1.97
50	2.0	69	0.612±0.007	0.999	87	16	2.33
60	1.1	70	1.116±0.009	0.998	105	16	1.64

Conditions: $[\epsilon\text{-CL}]_0$:$[Sc]_0$ as stated; $[\epsilon\text{-CL}]_0$ = 0.5 M in 0.6 mL Tol-d_8 at 30 °C. Reported for outlined shapes in Figure xx; measured by ^{1}H NMR spectroscopic analyses. First-order rate constant (k_{obs}) and R^2 were obtained from plots of $\ln([\epsilon\text{-CL}]_0/[\epsilon\text{-CL}]_t)$ *vs* time. [c] Calculated from monomer conversion data: $[M]_0/[Sc]_0$ × conv. (%) × 114.14 × 0.01 + (M_w of end groups (α+ω)).

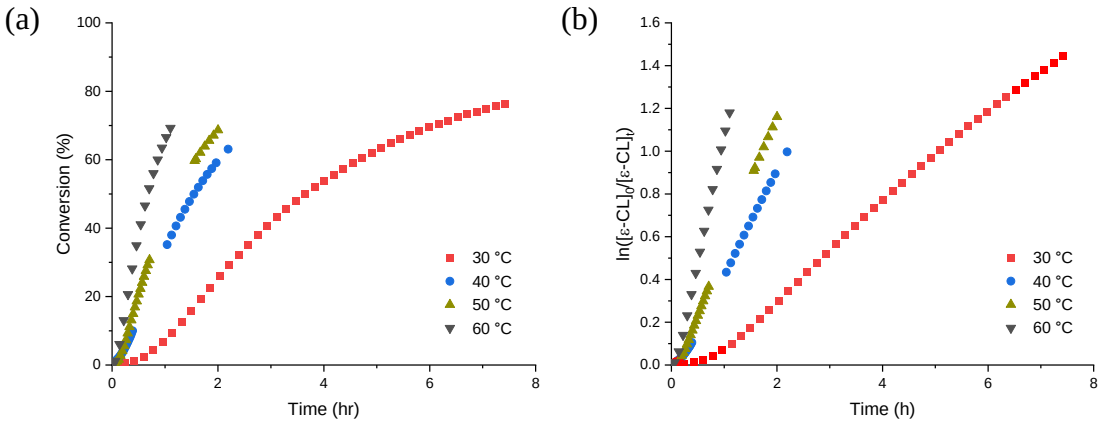


Figure A.119 (a) Plots of percentage conversion *vs.* time. (b) Plots of $\ln([\epsilon\text{-CL}]_0/[\epsilon\text{-CL}]_t)$ *vs.* time. Red squares: 30 °C (k_{obs} = 0.220 h^{-1}. R^2 = 0.999); blue circles: 40 °C (k_{obs} = 0.396 h^{-1}. R^2 = 0.999); green upward triangles: 50 °C (k_{obs} = 0.612 h^{-1}. R^2 = 0.999); black downward triangles (k_{obs} = 1.143 h^{-1}. R^2 = 0.998). Conditions: $[\epsilon\text{-CL}]_0$:[**5**]$_0$ = 200:1, $[\epsilon\text{-CL}]_0$ = 0.5 M in 0.6 mL toluene-d_8.

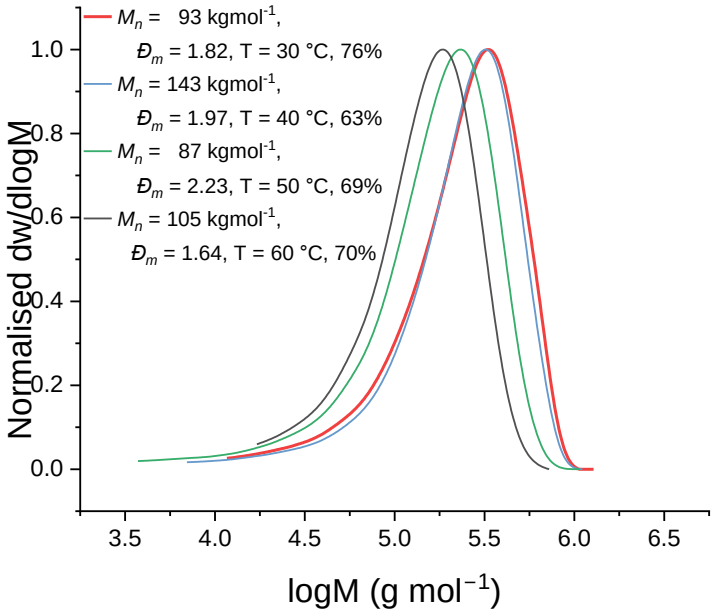


Figure A.120 Gel permeation chromatograms of ϵ-CL synthesised by **5** as a function of temperature. Polymerisation conditions: Conditions: $[\epsilon\text{-CL}]_0$:[**5**]$_0$ = 200:1, $[\epsilon\text{-CL}]_0$ = 0.5 M in 0.6 mL toluene-d_8.

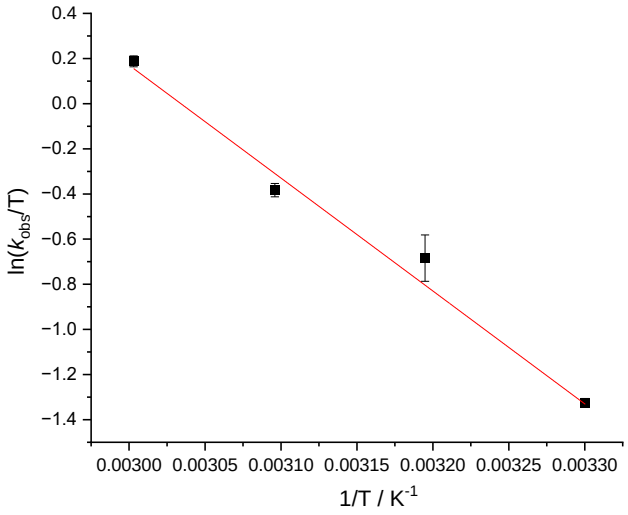


Figure A.121 Eyring plot of ln(k_{obs}/T) *vs.* 1/T. Slope = –5001.1 ± 214.7, intercept = 15.17 ± 0.67, R^2 = 0.9688, $\Delta H^{\ddagger}$ = 41.6 ± 1.8 kJ mol^{-1}, $\Delta S^{\ddagger}$ = –71.4 ± 5.6 J mol^{-1} K^{-1} for the ROP of *ϵ-CL* using ^{Me2}SB(^{tBu2}ArO,I*)Sc(ODipp)THF (**5**)

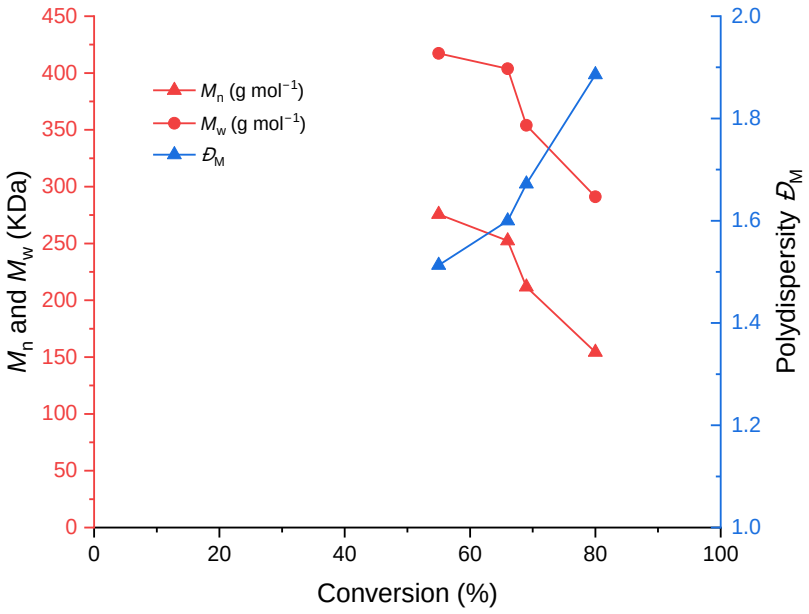


Figure A.122 Conversion vs M_n and M_w (Left, Red). Conversion vs Polydispersity ($Đ_M$) (Right, Blue). Conditions: Conditions: [ϵ-CL]:[**5**]$_0$ = 200:1, [ϵ-CL]$_0$ = 0.2 M, 6.0 mL Toluene at 25 °C.

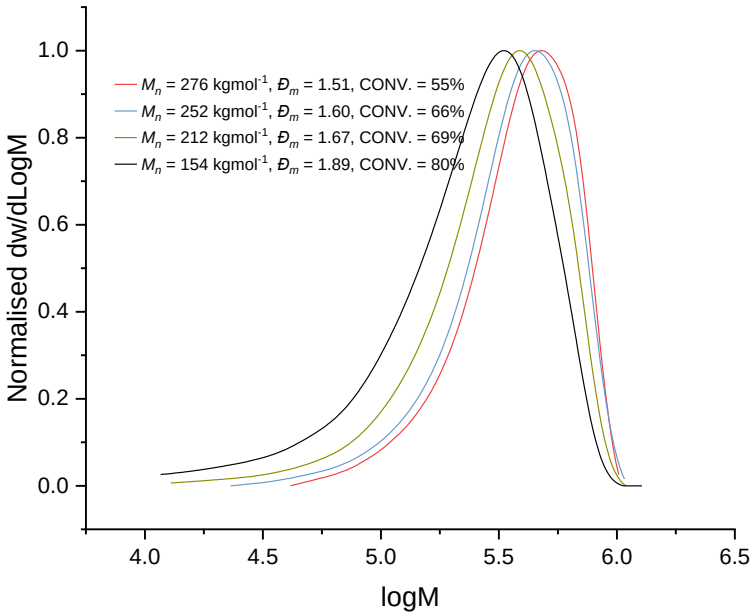


Figure A.123 Gel permeation chromatograms of ϵ-CL synthesised by **5** as a function of conversion: Conditions: [ϵ-CL]:[**5**]$_0$ = 200:1, [ϵ-CL]$_0$ = 0.2 M, 6.0 mL Toluene at 25 °C

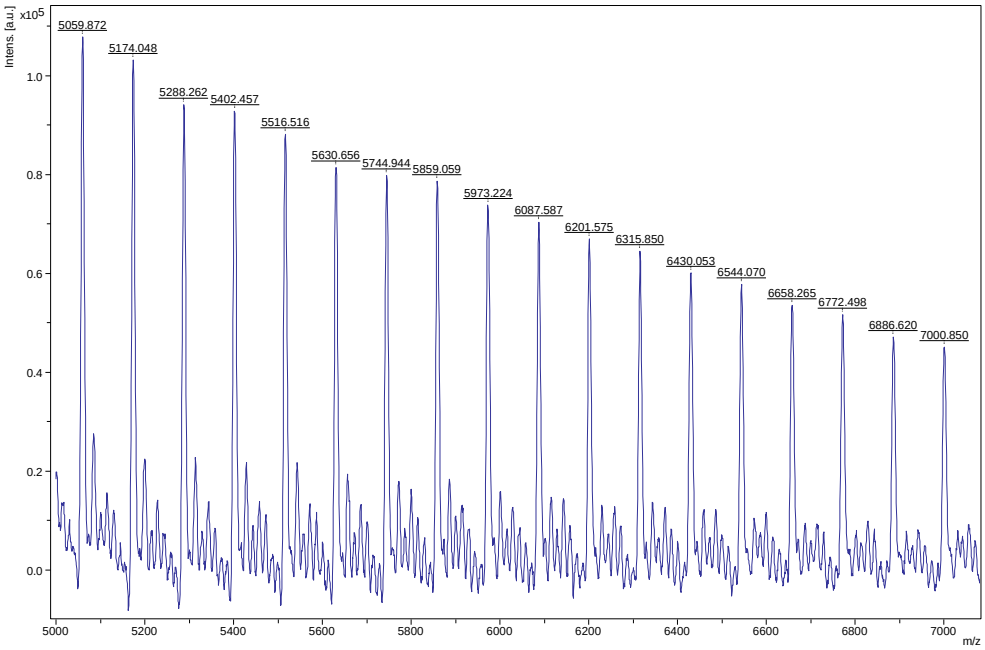


Figure A.124 MALDI-ToF mass spectrum of PCL synthesised using **5**. Mn(GPC) = 23 g mol^{-1}. Conditions: [ϵ-CL]:[**5**]$_0$ = 200:1, [ϵ-CL]$_0$ = 0.5 M, 0.6 mL Toluene at 25 °C. The cationisation agent was KTFA, and the matrix was DCTB. Δm/z = 114.1(4) Da between peak envelopes. Peak envelope centred at 5744.94 Da corresponds to 50 units of ϵ-CL and K^+ [114.1(44) + 39.1 = 5744.1(2.2)]

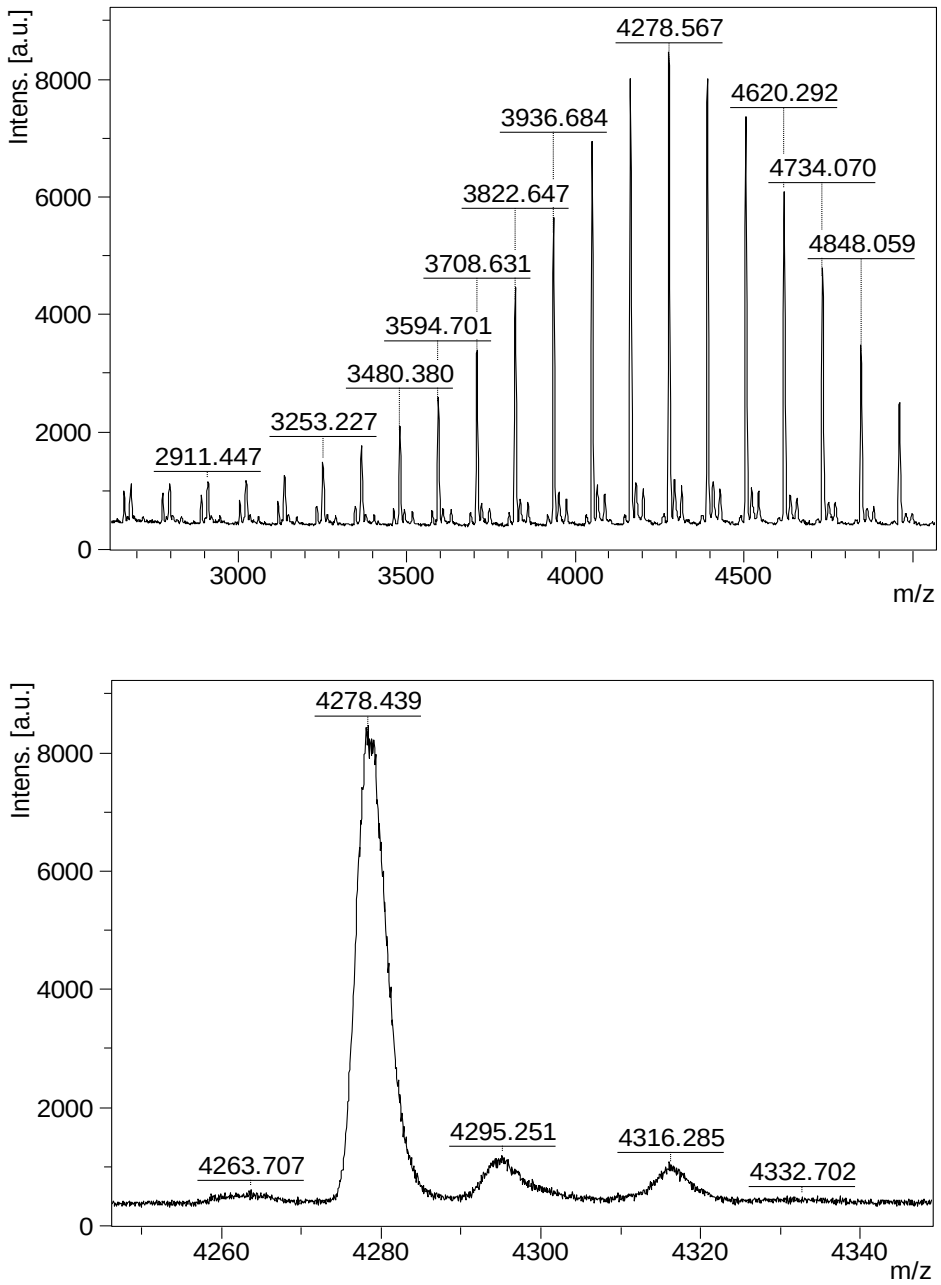


Figure A.125 MALDI-(Top) MALDI-ToF mass spectrum of ϵ-PCL synthesised using **5**. M. Conditions: [ϵ-CL]:[**5**]$_0$ = 200:1, [ϵ-CL]$_0$ = 0.5 M, 6.0 mL Toluene at 25 °C, 10% conversion. The cationisation agent was KTFA, and the matrix was DCTB. Δm/z = 114.1(4) Da between peak envelopes. Peak envelope centred at 4278.4 Da corresponds to 50 units of linear ϵ-CL (OH/H) and K^+ [114.14 + 39.1 + 18 = 4280.3 Da]. **(**Bottom**)** Expansion of between 4250–4350 *m/z*. mass fragments relating to polymer that occurring in spectrum.

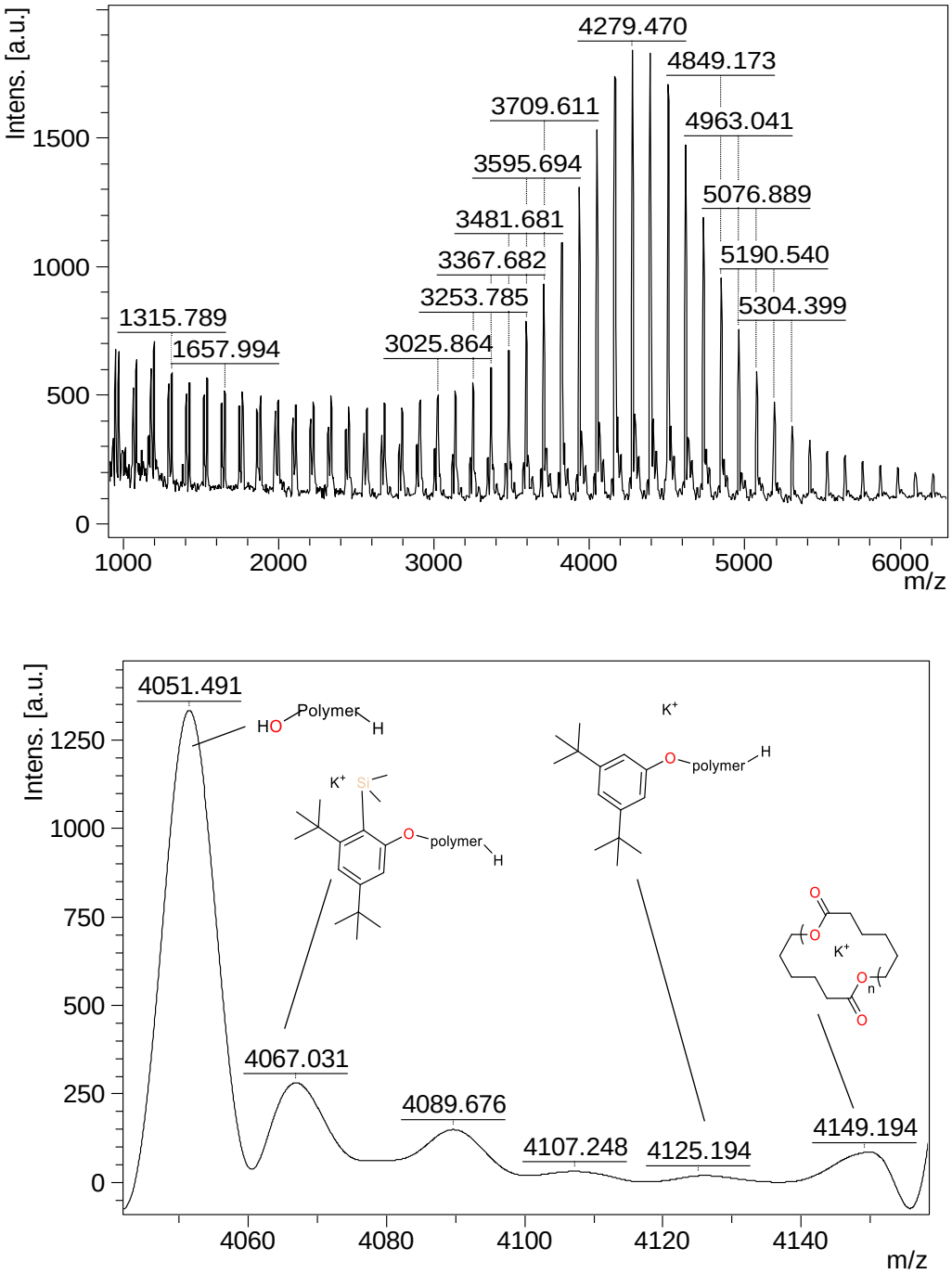


Figure A.126 (Top) MALDI-ToF mass spectrum of ϵ-PCL synthesised using **5**. M. Conditions: [ϵ-CL]:[**5**]$_0$ = 200:1, [ϵ-CL]$_0$ = 0.5 M, 6.0 mL Toluene at 25 °C, 10% conversion. The cationisation agent was KTFA, and the matrix was DCTB. Δm/z = 114.1(4) Da between peak envelopes. Peak envelope centred at 4394.71 Da corresponds to 50 units of linear ϵ-CL (OH/H) and K^+ [114.14 + 39.1 + 18 = 4394.42]. **(**Bottom**)** Expansion of between 4000–4160 *m/z*. mass fragments relating to polymer occuring in spectrum.

Table A.6 Mass fragments from MALDI-TOF spectrum in **Figure A.125**

m/z	End group (α\ω)	Calculated m/z	Chain length
4051.5	H/OH	4051.0	35
4067.0	H/$Me_2Si^{tbu2}ArO$	4068.0	33
4125.2	H/^{tbu2}OAr	4126.19	34
4149.2	Cyclic	4148.1	36

A.3.3.4. ϵ-CL using 5 and $OPPh_3$ - Variable temperature

Table A.7 ROP of ϵ-CL initiated by $OPPh_3$ complex **5** +$OPPh_3$ 200:1 [ϵ-CL]:[**Sc**].

Temp. (°C)	Time (h)	Conv.[a] (%)	k_{obs} (h^{-1})	R^2	$M_{n,SEC}$ *(kDa)*	$M_{n,\,th}$[a,c] *(kDa)*	$Đ_M$
30	11.2	65	0.115±0.05	0.999	180	15	1.45
50	2.7	62	0.442±0.009	0.998	140	14	1.62
55	1.7	67	0.716±0.010	0.996	132	15	1.61
60	1.3	63	0.917±0.006	0.998	151	14	1.62

Conditions: $[ϵ\text{-CL}]_0$:$[Sc]_0$ as stated; $[ϵ\text{-CL}]_0$ = 0.5 M in 0.6 mL Tol-d_8 at 'T' °C. [a] measured by ^{1}H NMR spectroscopic analyses. First-order rate constant (k_{obs}) and R^2 were obtained from plots of $\ln([ϵ\text{-CL}]_0/[ϵ\text{-CL}]_t)$ *vs* time. [b] [c] Calculated from monomer conversion data: $[M]_0/[Sc]_0 \times$ conv. (%) × 114.14 × 0.01 + (M_w of end groups (α+ω)).[d]

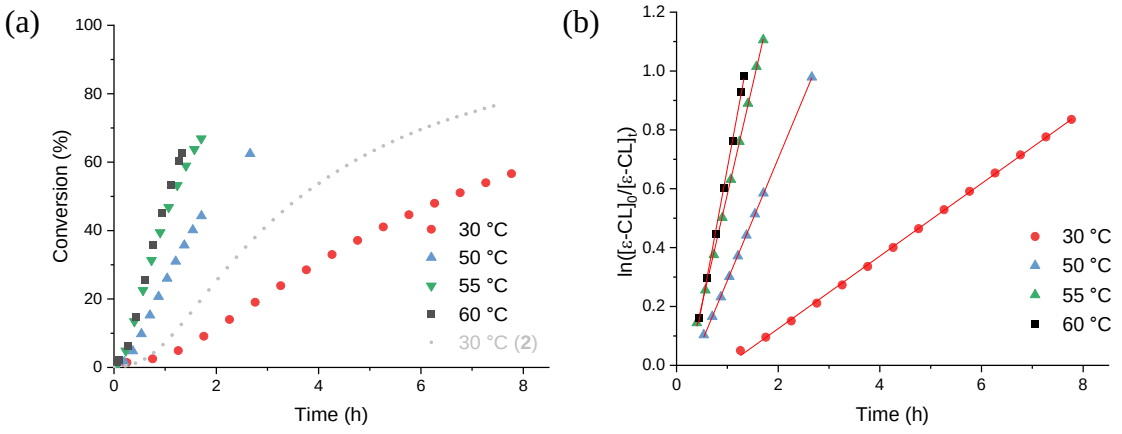


Figure A.127 a) Plots of percentage conversion *vs.* time. (b) Plots of $\ln([ϵ\text{-CL}]_0/[ϵ\text{-CL}]_t)$ *vs.* time. Red circles: 30 °C (k_{obs} = 0.115±0.005 h^{-1}. R^2 = 0.999); blue upward triangles: 50 °C (k_{obs} = 0.442±0.009 h^{-1}. R^2 = 0.998); green downward triangles: 55 °C (k_{obs} = 0.716±0.010 h^{-1}. R^2 = 0.996); black squares 60 °C (k_{obs} = 0.917±0.006 h^{-1}. R^2 = 0.998). Conditions: $[ϵ\text{-CL}]_0$:$[Sc]_0$ as 200:1, $[ϵ\text{-CL}]_0$ = 0.5 M in 0.6 mL toluene-d_8. Sc = **12** (5 + $OPPh_3$)

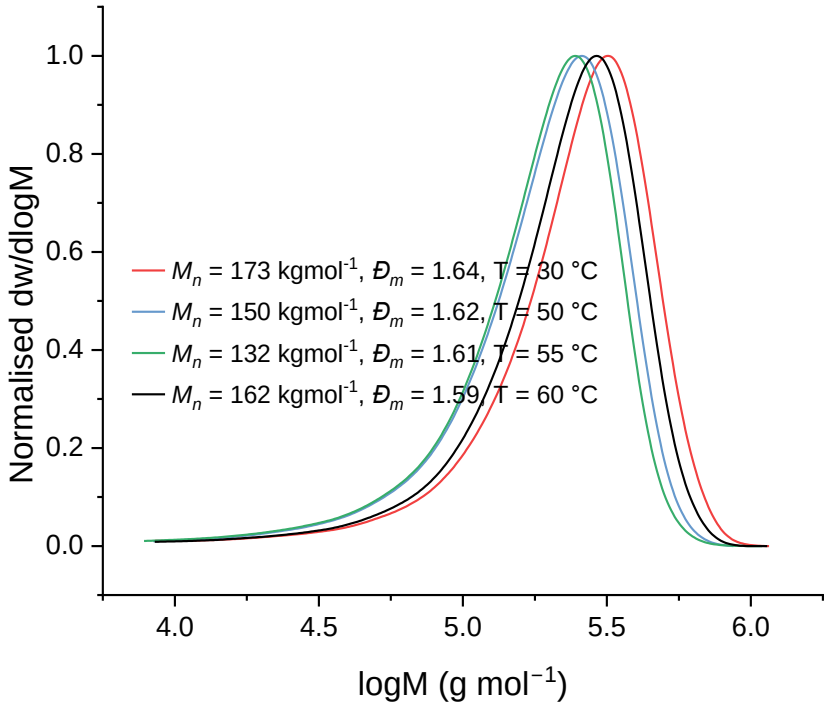


Figure A.128 Gel permeation chromatograms of ϵ-CL synthesised by **5 (5 + OPPh$_3$)** as a function of temperature**.** Conditions: [ϵ-CL]$_0$:[5]$_0$:[OPPh$_3$] = 200:1:1; [ϵ-CL]$_0$ = 0.5 M in 0.6 mL Tol-d_8 at 'T' °C.

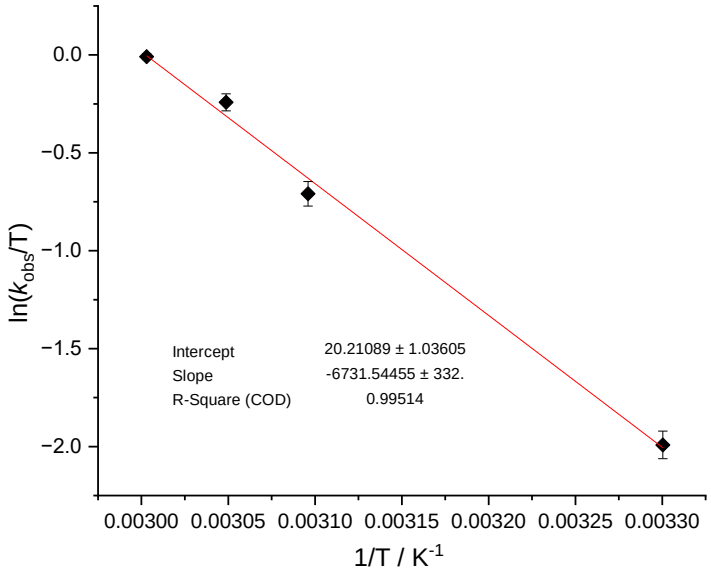


Figure A.129 Eyring plot of ln(k_{obs}/T) *vs.* 1/T. Slope = –6731.5 ± 332, intercept = 20.21 ± 1.04, R^2 = 0.9951, $\Delta H^{\ddagger}$ = 56.0 ± 2.8 kJ mol^{-1}, $\Delta S^{\ddagger}$ = –29.5 ± 8.6 J mol^{-1} K^{-1} for the ROP of *ϵ-CL* using **(5 + OPPh$_3$).**

A.3.3.5. ϵ-CL using 7 – Variable concentration and temperature

Table A.8 ROP of ϵ-CL using PHENI*-AMIDO scandium complex **7** at various stoichiometries

$[M]_0/[Sc]_0$	Temp. (°C)	Time (min)	Conv.[a]	k_{obs} (h^{-1})	R^2	$M_{n,SEC}$[b,(d)]	$M_{n,\,th}$[a,c]	$Đ_M$[b]
250	30	10	72	6.61	0.999	73	21	2.20
500	30	15	60	3.55	0.996	110	34	1.85
750	30	20	61	2.79	0.972	118	52	1.51

Conditions: $[ϵ\text{-CL}]_0:[Sc]_0$ as stated; $[ϵ\text{-CL}]_0$ = 0.5 M in 0.6 mL Tol-d_8 at 30 °C. Measured by ^{1}H NMR spectroscopic analyses. First-order rate constant (k_{obs}) and R_2 were obtained from plots of $\ln([ϵ\text{-CL}]_0/[ϵ\text{-CL}]_t)$ *vs* time. [c] Calculated from monomer conversion data: $[M]_0/[Sc]_0 \times$ conv. (%) × 114.14 × 0.01 + (M_w of end groups (α+ω)).[d]

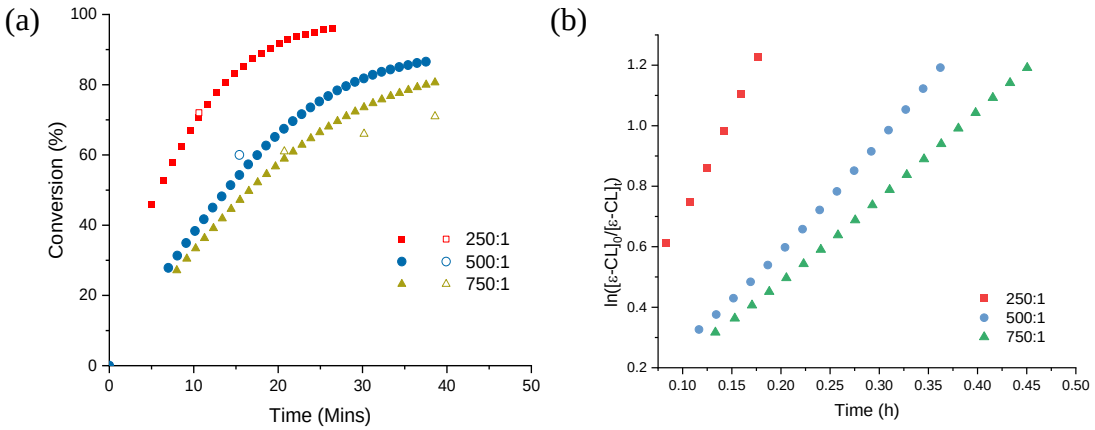


Figure A.130 (a) Plots of percentage conversion *vs.* time. (b) Plots of $\ln([ϵ\text{-CL}]_0/[ϵ\text{-CL}]_t)$ *vs.* time. Red squares: 250:1 (k_{obs} = 2.79 h^{-1}. R^2 = 0.999); blue circles: 500:1 (k_{obs} = 3.55 h^{-1}. R^2 = 0.996); green upward triangles: 750:1 (k_{obs} = 6.61 h^{-1}. R^2 = 0.972). Conditions: $[ϵ\text{-CL}]_0:[Sc]_0$ as stated, $[ϵ\text{-CL}]_0$ = 0.5 M in 0.6 mL toluene-d_8 at 30 °C.

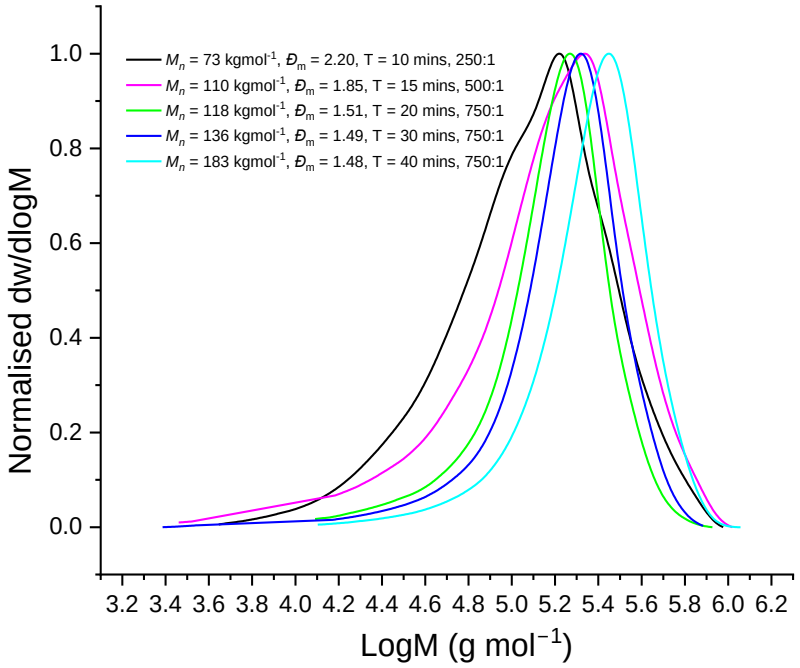


Figure A.131 Gel permeation chromatograms of ϵ-CL synthesised by **7** as a function of concentration. Conditions: $[\epsilon\text{-CL}]_0$:$[Sc]_0$ as stated; $[\epsilon\text{-CL}]_0$ = 0.5 M in 0.6 mL Tol-d_8 at 30 . ROP of ϵ-CL using PHENI*-AMIDO scandium complex **7** at various stoichiometries

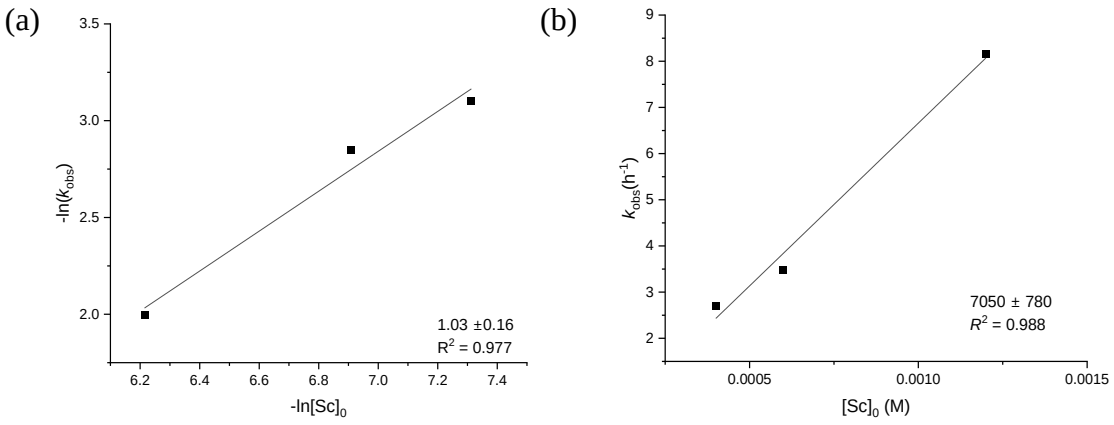


Figure A.132 (a) Plot of $-\ln(k_{obs})$ *vs.* $-\ln[Sc]_0$ for ROP of ϵ-CL at 30°C with **7**. Order of reaction with respect to $[Sc]_0$ is 1.03 ± 0.15; R^2 = 0.977. (b) Plot of k_{obs} *vs.* $[Sc]_0$ for ROP of ϵ-CL using **7** where k_p = 7050 ± 780 M^{-1} h^{-1}; R^2 = 0.988

Table A.9 ROP of ϵ-CL using PHENI*-AMIDO scandium complex **7** [ϵ-CL]:[Sc] 750:1.

Temp. (°C)	Time (h)	Conv.[a] (%)	k_{obs} (h^{-1})	R^2	$M_{n,SEC}$[b]	$M_{n,\,th}$[a,c]	$Đ_M$[b]
0	4.8	75	0.250±0.014	0.998	183(105)		1.99(2.20)
10	2.2	75	0.510±0.006	0.999	198(115)		1.79(1.94)
20	0.63	74	1.473±0.037	0.996	143(81)		1.87(2.03)
30	0.64	81	2.79±0.026	0.968	183	52	1.48
60	0.15	50	6.48±0.019	0.999	-	-	-

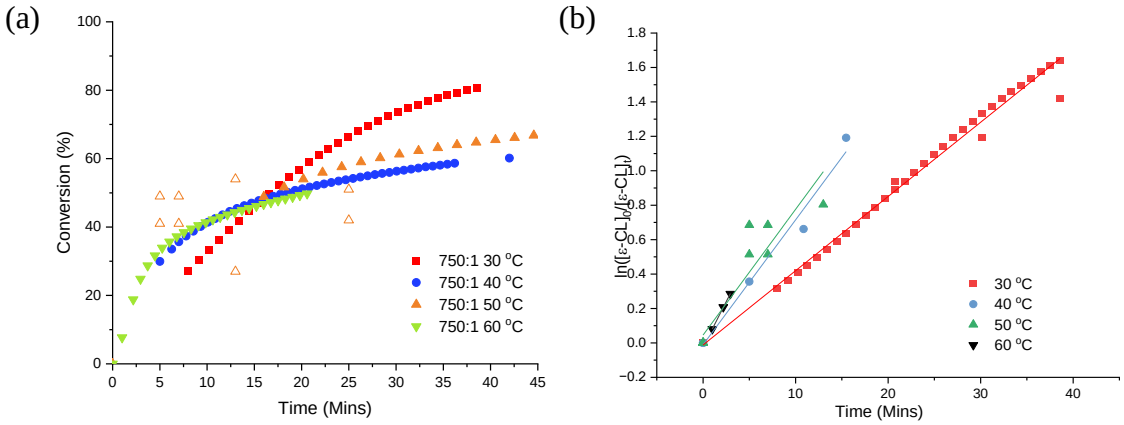


Figure A.133 (a) Plots of percentage conversion *vs.* time. (b) Plots of $\ln([\epsilon\text{-CL}]_0/[\epsilon\text{-CL}]_t)$ *vs.* time. Red squares: 30 °C; blue circles: 40 °C green upward triangles: 50 °C; black squares: 60 °C. Conditions: $[\epsilon\text{-CL}]_0$:$[Sc]_0$ as stated, $[\epsilon\text{-CL}]_0$ = 0.5 M in 0.6 mL toluene-d_8 at 750:1

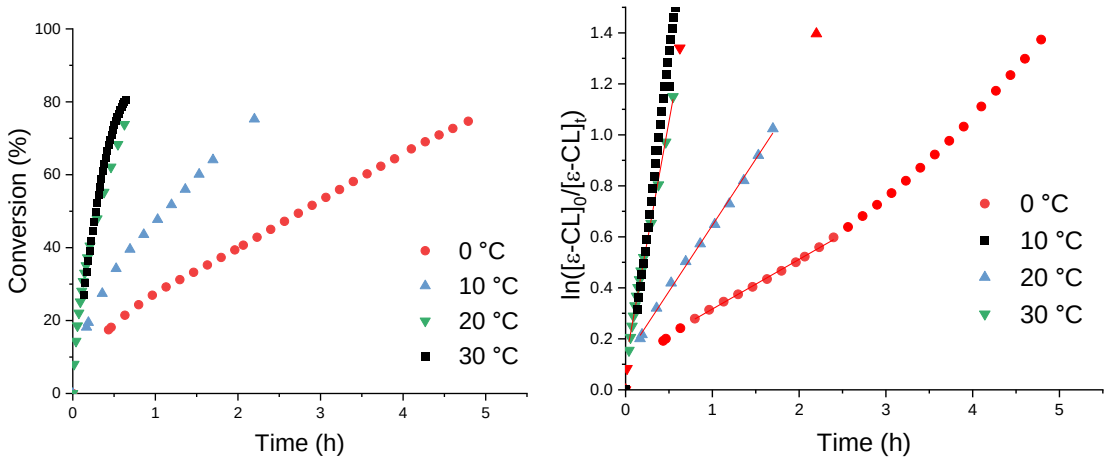


Figure A.134 (a) Plots of percentage conversion *vs.* time. (b) Plots of $\ln([\epsilon\text{-CL}]_0/[\epsilon\text{-CL}]_t)$ *vs.* time. Red squares: 0 °C; blue circles: 10 °C green upward triangles: 20 °C. Conditions: $[\epsilon\text{-CL}]_0$:$[Sc]_0$ as stated, $[\epsilon\text{-CL}]_0$ = 0.5 M in 0.6 mL toluene-d_8 at 750:1 Red circles: 0 °C (k_{obs} = 0.250±0.014 h^{-1}. R^2 = 0.999); blue upward triangles: 10 °C (k_{obs} = 0.510±0.006 h^{-1}. R^2 = 0.998); green downward triangles: 20 °C (k_{obs} = 1.473±0.037 h^{-1}. R^2 = 0.996); black squares 30 °C (k_{obs} = 0.2.58±0.054 h^{-1}. R^2 = 0.968).

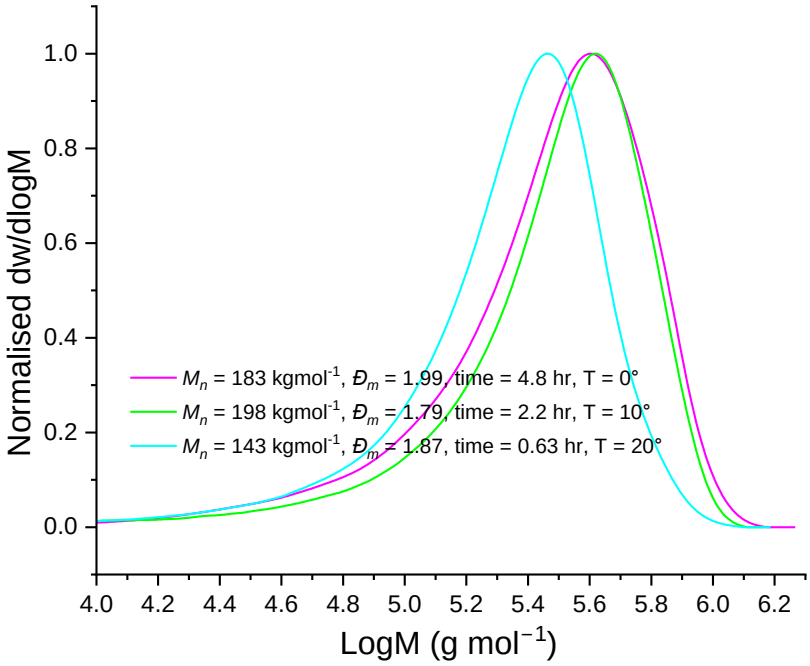


Figure A.135 Gel permeation chromatograms of ϵ-CL synthesised by **7** as a function of temperature Conditions: $[\epsilon\text{-CL}]_0$:$[Sc]_0$ [750]:[1]; $[\epsilon\text{-CL}]_0$ = 0.5 M in 0.6 mL Tol-d_8 at T stated °C. ROP of ϵ-CL using PHENI*-AMIDO scandium complex **7** at temperatures. Duplicates not shown.

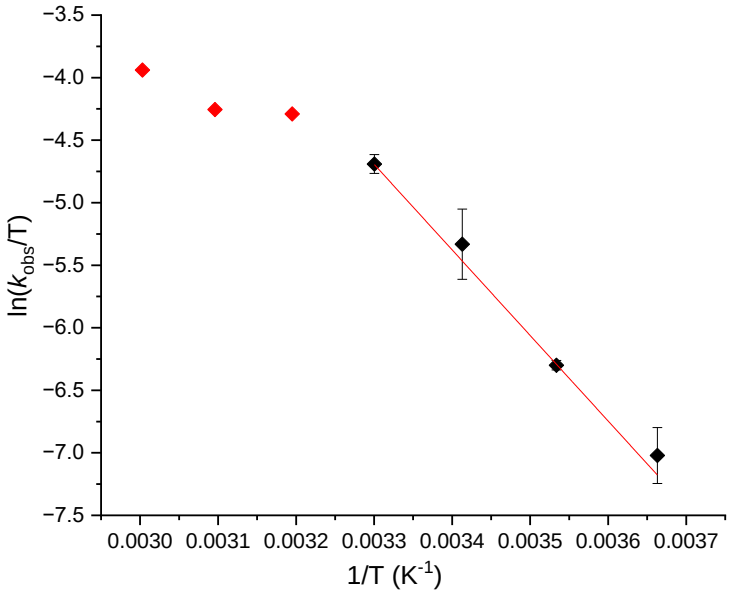


Figure A.136 Eyring plot of ln(k_{obs}/T) *vs.* 1/T. Slope = –6843.3 ± 214.6, intercept = 17.9 ± 0.7, R^2 = 0.9398, $\Delta H^{\ddagger}$ = 56.9 ± 1.8 kJ mol^{-1}, $\Delta S^{\ddagger}$ = –48.8 ±6.2 J mol^{-1} K^{-1} for the ROP of *ϵ-CL* using ^{Me_2}SB($^{t\text{Bu}}$N,I*)Sc(ODipp)THF (**7**). Deviation from linearity at higher temperatures (red diamonds) no included in calculations.

A.3.3.6. ϵ-CL using Sc(OAr)$_3$.2THF. OAr = ^{iPr2}OAr (29) and ^{tBu2}OAr (30)

Table A.10 ROP of ϵ-CL initiated by Sc complexes **29** and **30**.

Cat.	$[M]_0/[Sc]_0$	Temp. (°C)	Time (h)	Conv.[a] (%)	$M_{n,SEC}$[b] (kDa)	$M_{n,th}$[a,c] (kDa)	$Đ_M$[b]
29	50	30	83	67	98	3.8	2.17
30	50	30	30	95	32	5.4	1.59

Conditions: $[ϵ\text{-CL}]_0:[Sc]_0$ as 50:1, $[ϵ\text{-CL}]_0$ = 0.5 M in 0.6 mL benzene-d_6 at 30 °C. [a] Measured by ^{1}H NMR spectroscopic analyses. First-order rate constant (k_{obs}) and R^2 were obtained from plots of $\ln([ϵ\text{-CL}]_0/[ϵ\text{-CL}]_t)$ *vs* time. [b] [c] Calculated from monomer conversion data: $[M]_0/[Sc]_0$ × conv. (%) × 114.14 × 0.01 + (MW of end groups (α+ω)) in kDa

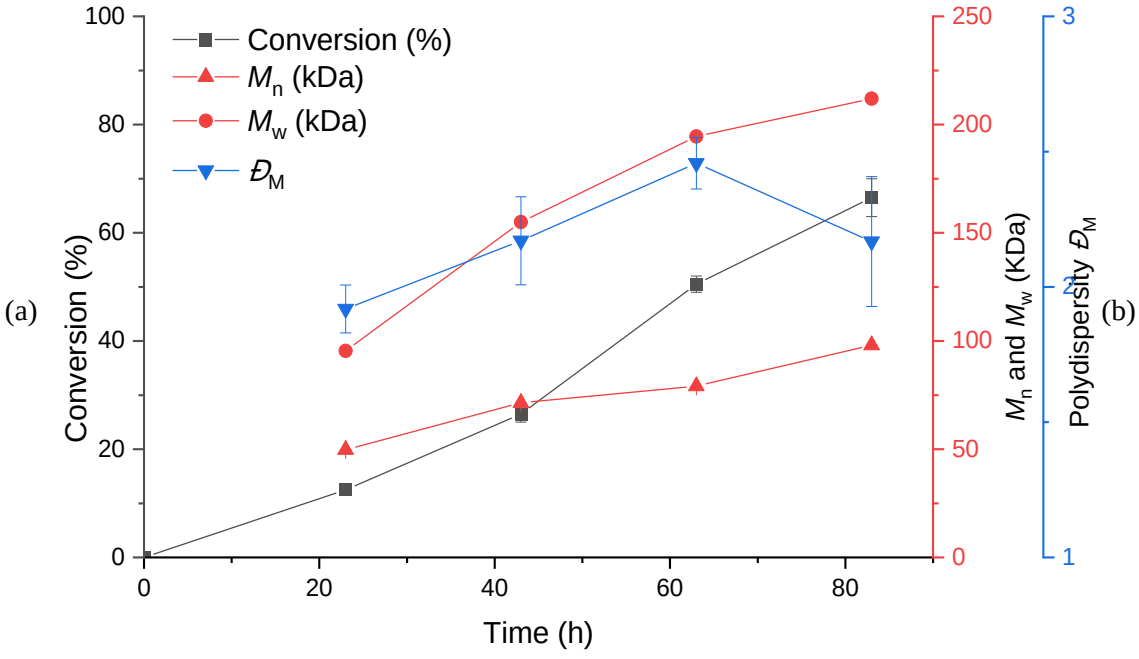


Figure A.137 (a) Conversion (%) vs Time (hr). (Right, red) M_n and M_w (kDa) vs Time (hr) and (right, blue) Polydispersity $Đ_M$ vs Time (h). Conditions: $[ϵ\text{-CL}]_0$:[**Sc**]$_0$ 50:1, $[ϵ\text{-CL}]_0$ = 0.5 M in 6 mL toluene at 25 °C. (b) GPC traces for left. ROP of ϵ-CL using Sc(ODipp)$_3$.2THF (**29**).

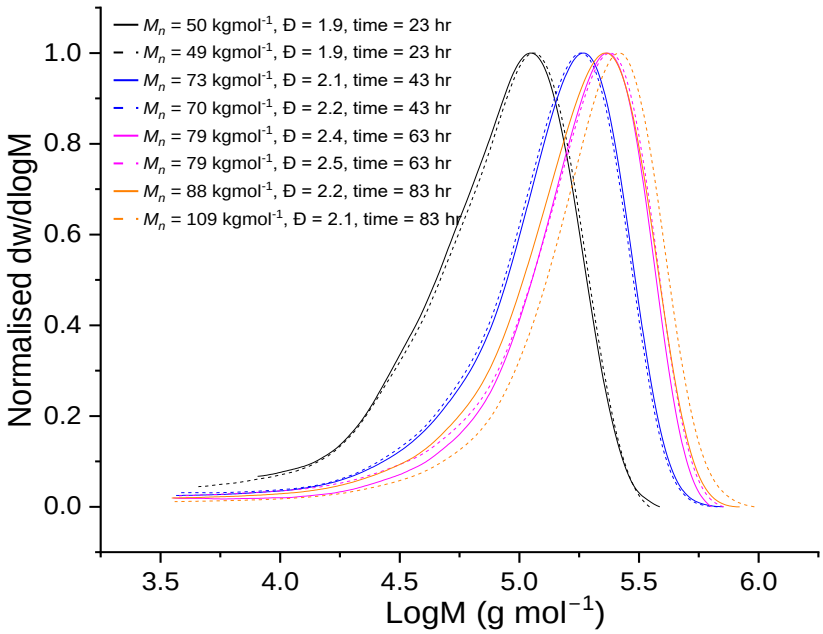


Figure A.138 Gel permeation chromatograms of ϵ-CL synthesised by **5** as a function of time. Conditions: $[\epsilon\text{-CL}]_0$:$[\mathbf{Sc}]_0$ 50:1, $[\epsilon\text{-CL}]_0$ = 0.5 M in 6 mL toluene at 25 °C.

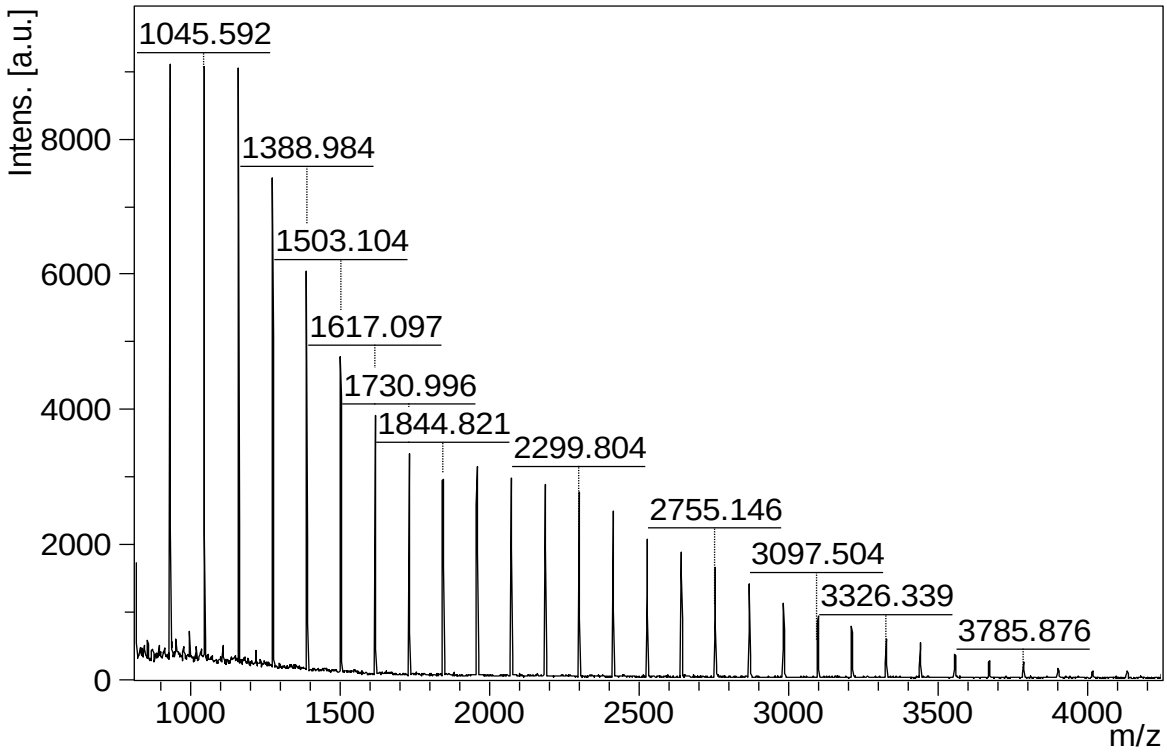


Figure A.139 MALDI-ToF mass spectra of ϵ-PCL synthesised using (**Sc(O-2,4-^{tbu2}Ar)$_3$**) **2THF**. Mn(GPC) = 3509 g mol^{-1} , M_w/M_n = 1.98. Conditions: [ϵ-CL]:$[\mathbf{sc}]_0$ = 10:1, $[\epsilon\text{-CL}]_0$ = 0.5 M, $[\mathbf{sc}]_0$ = 0.01 M, 0.6 mL Toluene-d_8 at 25 °C after 2.5 hr, 10 % conversion. The cationisation agent was KTFA, and the matrix was DCTB. Δm/z = 114.1(4)± 1 Da between peak envelopes.

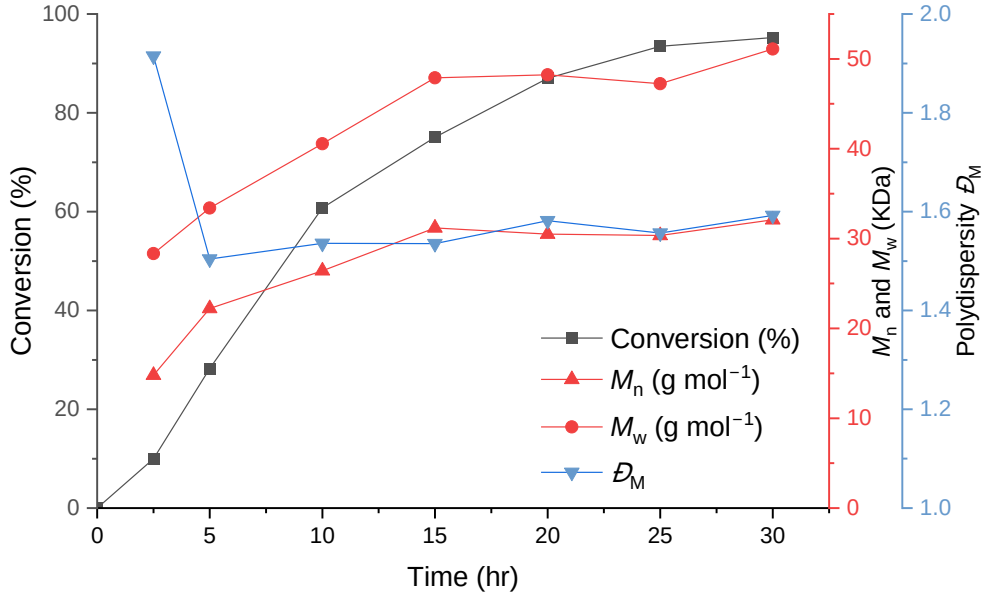


Figure A.140 Conversion (%) vs Time (hr). (Right, red) M_n and M_w (kDa) vs Time (hr) and (right, blue) Polydispersity $Đ_M$vs Time (hr). Conditions: [ϵ-CL]$_0$:[**30**]$_0$ 50:1, [ϵ-CL]$_0$ = 0.5 M in 0.6 mL toluene-d_8 at 30 °C. ROP of ϵ-CL using Sc(O-2,4-^{t}Bu-C$_6$H$_3$)$_3$.2THF **30**

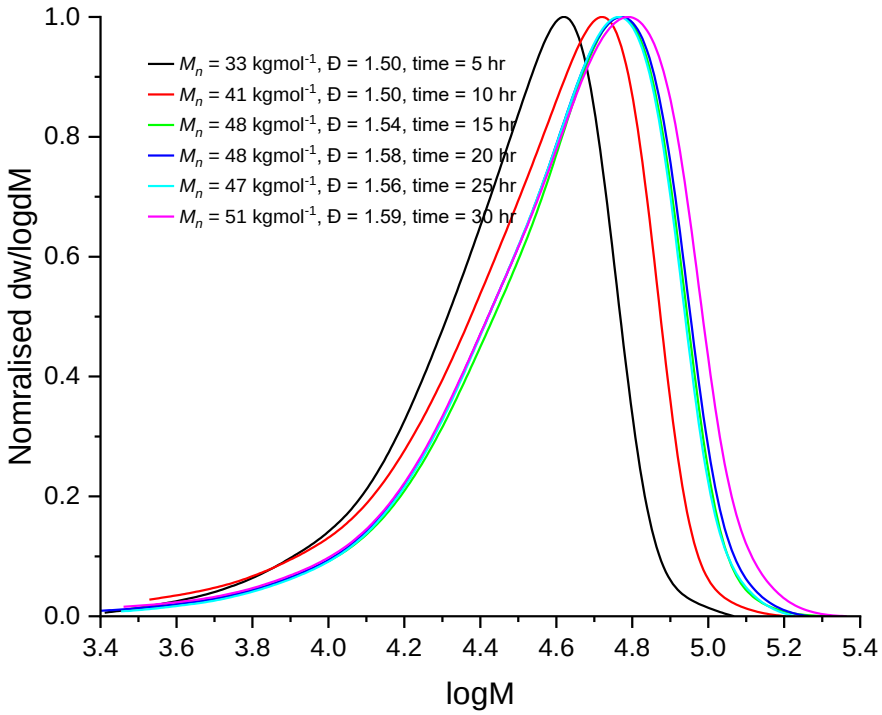


Figure A.141 Gel permeation chromatograms of ϵ-CL synthesised by **30** as a function of time. Conditions: [ϵ-CL]$_0$:[**30**]$_0$ 50:1, [ϵ-CL]$_0$ = 0.5 M in 0.6 mL toluene-d_8 at 30 °C. ROP of ϵ-CL using Sc(O-2,4-^{t}Bu-C$_6$H$_3$)$_3$.2THF **30**

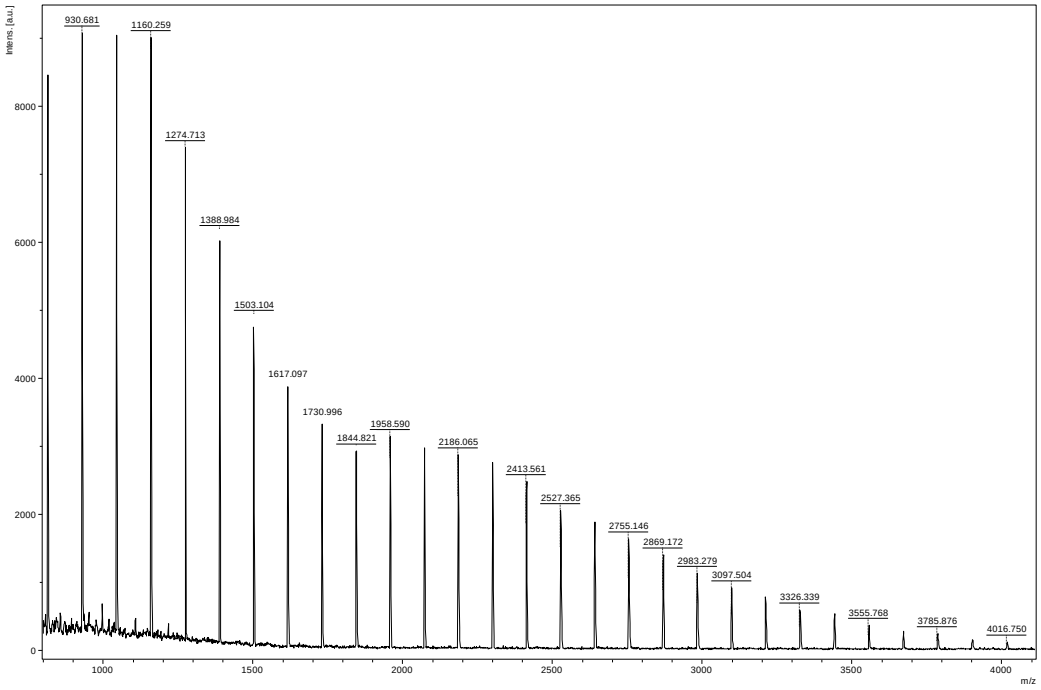


Figure A.142 MALDI-ToF mass spectra of ϵ-PCL synthesised using (**30**). Conditions: [ϵ-CL]:[**Sc**]$_0$ = 10:1, [ϵ-CL]$_0$ = 0.5 M, [**Sc**]$_0$ = 0.01 M, 0.6 mL Toluene-d_8 at 25 °C. The cationisation agent was KTFA, and the matrix was DCTB. Δm/z = 114.1(4) Da between peak envelopes. Peak envelope centred at 1844.821 Da corresponds to 14 units of ϵ-CL, -O-2,4-*tert*butyphenyl and K^+ [114.1(44) +206.33 + 39.1 = 1843.39(0.62)].

A.3.4. Copolymerisation ϵ-CL and L-La using 7 and $OPPH_3$

Table A.11 ROP of *L*-LA ϵ-CL initiated by Sc complexes **7**.

ϵ-CL	L-LA	$OPPh_3$	Temp. (°C)	Time (h)	Conv. (ϵ-CL/L-LA)[a] (%)	$M_{n,SEC}$[b] (kDa)	$Đ_M$[b]
250	250	1	60	4.23	0/87	56	1.36
25	25[d]	1	30/60	3/	60/80	5	2.15
750	0	0	60	0.15	50		
0	750	0	70	3	xx	xx	xx
0	750	1	70	1	xx	xx	xx

Conditions: [ϵ-CL]$_0$:[Sc]$_0$ as 50:1, [ϵ-CL]$_0$ = 0.5 M in 0.6 mL toluene-d_6 at stated temperature. [a] Measured by ^{1}H NMR spectroscopic analyses with ϵ-CL conversion in brackets. First-order rate constant (k_{obs}) and R^2 were obtained from plots of ln([ϵ-CL]$_0$/[ϵ-CL]$_t$) *vs* time. [b] [c] Calculated from monomer conversion data: [M]$_0$/[Sc]$_0$ × conv. (%) × 114.14 × 0.01 + (MW of end groups (α+ω)) in kDa.[d] *L*-Lactide added after 3 mins at R

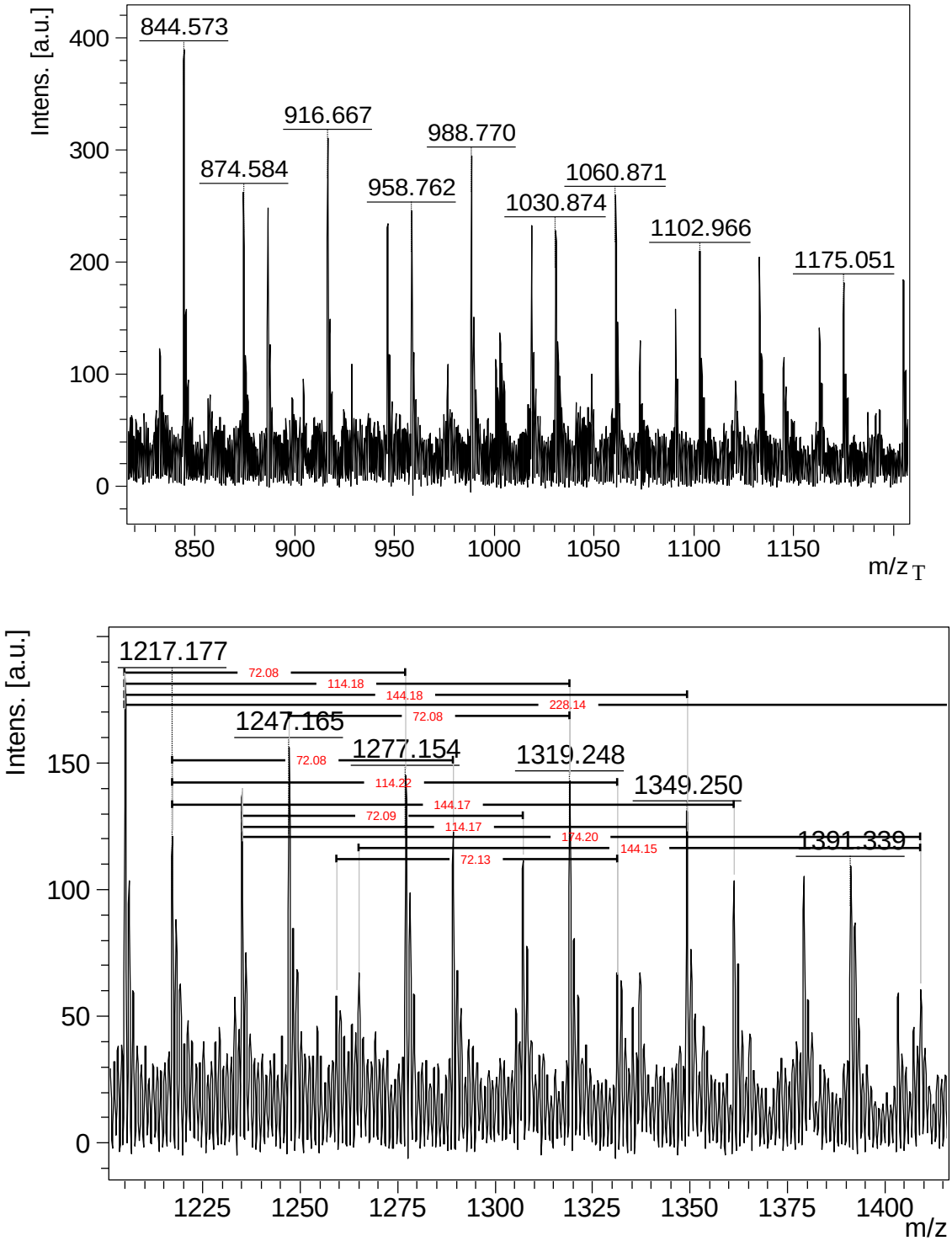


Figure A.143 MALDI-ToF mass spectra of ϵ-PCL synthesised using (**7**). Conditions: [ϵ-CL]:[L-La]:[**7**]$_0$ = 25:25:1, [ϵ-CL]$_0$ = 0.05 M, 0.6 mL Toluene-d_8 at 25 °C. The cationisation agent was KTFA, and the matrix was DCTB.

A.4. Additional files

A.4.1. Crystallographic information file

File containing inputs for DFT studies.

"Computational coordinates and final free gibbs energy.xyz"

ORCA INP

```
#geometry optimization
!RKS r2SCAN-3c RIJCOSX SlowConv TightSCF def2-SVP Normalprint Opt Freq PAL8
%basis NewGTO Sc "def2-TZVP" end
        NewGTO O "def2-TZVP" end
        NewGTO Si "def2-TZVP" end
        NewGTO N "def2-TZVP" end  /* or P*/
    End
*xyz 0 1
…
```